THE UNIVERSITY OF CHICAGO

QUANTUM MEASUREMENTS OF MICROWAVE-FREQUENCY ACOUSTIC RESONATORS WITH SUPERCONDUCTING CIRCUITS

A DISSERTATION SUBMITTED TO
THE FACULTY OF THE DIVISION OF THE PHYSICAL SCIENCES
IN CANDIDACY FOR THE DEGREE OF
DOCTOR OF PHILOSOPHY

DEPARTMENT OF PHYSICS

BY
MING-HAN CHOU

CHICAGO, ILLINOIS
MARCH 2023

CONTENTS

LIST OF FIGURES v

LIST OF TABLES vii

ACKNOWLEDGMENTS viii

ABSTRACT x

1 INTRODUCTION 1

2 THEORY 4
2.1 Superconducting circuits 4
2.1.1 LC resonator 4
2.1.2 Superconducting qubits 6
2.1.3 Qubit readout 9
2.1.4 Qubit control lines 12
2.1.5 Capacitive and inductive coupling 13
2.2 Mechanical device 15
2.2.1 Elastic waves in a solid 15
2.2.2 Piezoelectricity 17
2.2.3 Interdigital transducer 18
2.2.4 Loss mechanisms for surface acoustic wave devices 20
2.2.5 Phononic crystals 22

3 CIRCUIT DESIGN 25
3.1 Butterworth-van Dyke (BVD) circuits 26
3.2 Estimating the number of phonons in a BVD resonator 31
3.3 Qubit coupled to a mechanical resonator 33
3.4 Design of control lines 38

4 FABRICATION 44
4.1 Fabrication process for FBAR devices 44
4.1.1 Overview 44
4.1.2 Silicon-on-insulator (SOI) substrate 45
4.1.3 Alignment markers for optical lithography 45
4.1.4 Silicon oxide stop layer 48
4.1.5 Aluminum nitride deposition 48
4.1.6 Gold and chromium markers for electron beam lithography 51
4.1.7 Aluminum nitride etch 51
4.1.8 Silicon oxide protective layer 52
4.1.9 Pattern phononic crystals 53
4.1.10 Pattern interdigital transducer 54
4.1.11 Pattern releasing windows 54

4.1.12 Mechanically release devices with vapor HF . . . 55
4.2 Superconducting circuits fabrication . . . 57
4.3 Flip-chip integration . . . 61

5 CHARACTERIZATION OF THE FBAR DEVICES . . . 64
5.1 Microwave transmission measurement . . . 64
5.1.1 Room temperature measurement . . . 64
5.1.2 Cryogenic temperature measurement . . . 65
5.2 Quantum measurement with a superconducting qubit . . . 66
5.3 Hole-burning technique to enhance resonator lifetime . . . 71

6 CONCLUSION AND OUTLOOK . . . 74

A FABRICATION PROCEDURE AND RECIPES . . . 76
A.1 Silicon oxide stop layer deposition procedure . . . 76
A.2 AlN sputtering procedure . . . 77
A.3 Gold and Chromium markers deposition procedure . . . 78
A.4 AlN dry etching procedure . . . 78
A.5 Fabrication procedure for silicon devices . . . 79
A.6 Fabrication procedure for interdigital transducers . . . 80
A.7 Fabrication procedure for release windows . . . 81
A.8 Commonly used recipes . . . 82
A.8.1 Solvent clean procedure . . . 82
A.8.2 Optical lithography with positive photoresist AZ1512 . . . 82
A.8.3 Strip photoresist . . . 83
A.8.4 AlN sputter procedure and recipe . . . 83
A.8.5 NMP liftoff process . . . 84
A.8.6 H-SiQ development process . . . 85
A.8.7 PMMA bilayer process . . . 86
A.8.8 Aluminum deposition for liftoff process . . . 87
A.8.9 SU8 3005 spacer process . . . 88

B CIRCUIT TRANSFORMATION AND FORMULA . . . 90
B.1 Replace a mutual inductor with a T-circuit . . . 90
B.2 Conversion between Π-circuit and T-circuit . . . 90
B.3 A control line inductively couples to external circuits . . . 91

C EXPERIMENTAL SETUP . . . 92

D RESONATORS AND QUALITY FACTORS . . . 95

BIBLIOGRAPHY . . . 97

LIST OF FIGURES

2.1 Schematic diagrams show the LC circuits, Josephson junction and a frquency-tunable qubit. 5
2.2 Energy levels for a linear LC resonator and a qubit. 9
2.3 Readout transmission signals from a typical qubit device. 11
2.4 The microwave transmission signal of the readout line. 12
2.5 A Bloch sphere and the schematic for qubit control lines. 13
2.6 Circuit diagrams for capacitive and inductive coupling of two resonators. 14
2.7 Lamb wave in a bilayer membrane. 17
2.8 Schematic of an IDT. 19
2.9 IDT electrical responses for the different number of finger pairs. 20
2.10 Schematic slowness curve and the SAW propagation direction. 21
2.11 A phononic crystal and its band structure 23

3.1 Circuit model for a qubit integrated with a BVD resonator. 26
3.2 The circuit diagram for a BVD resonator. 26
3.3 The schematic diagram of the SAW resonator. 27
3.4 The absolute value of an impedance for a BVD circuit. 28
3.5 The microwave transmission measurement schematic diagram for a through configuration and tee configuration. 29
3.6 Microwave transmission signals with a through configuration. 30
3.7 The typical circuit diagram for measuring a BVD resonator. 31
3.8 Lossless circuit model for coupling a qubit to a BVD resonator. 35
3.9 Avoided-level crossing and coupling strength diagrams for different coupler inductances. 38
3.10 Avoided-level crossing and coupling strength diagrams for different IDT capacitances. 39
3.11 Gmon circuits with a coupler control line. 41
3.12 Gmon qubit lifetime T_q versus coupler junction phase. 42
3.13 Mechanical resonator lifetime at different coupler junction phases. 42
3.14 The admittance of the qubit-resonator device. 43

4.1 Overview of the FABR fabrication procedure. 46
4.2 SEM images of a FBAR device. 47
4.3 AlN sample rocking curve. 50
4.4 The AlN film stress tunability. 50
4.5 AlN film characterization. 51
4.6 The geometry of a ramp and notch. 52
4.7 SEM images of H-SiQ residue. 54
4.8 Contamination due to the vapor HF etching. 56
4.9 Vapor HF undercuts of the buried oxide layer of a test device. 56
4.10 Overview of a typical qubit chip. 60
4.11 Photograph of an assembled device. 62
4.12 A flip-chip integrated device. 62

4.13 CO_2 phase diagram. 63

5.1 Room temperature microwave transmission measurement for a FBAR resonator 64
5.2 Microwave transmission measurements at $T \sim 80\,\mathrm{mk}$ for a FABR resonator. . . . 65
5.3 Effective qubit frequency for different coupler inductances. 67
5.4 Qubit lifetime and coherence time. 68
5.5 Qubit spectroscopy. 69
5.6 Qubit-resonator Rabi swaps measurement. 70
5.7 Phonon lifetime measurement. 71
5.8 Resonator lifetime at different phonon levels. 72
5.9 Hole-burning experiment for enhancing resonator lifetime. 73

A.1 The angled SEM images of the silicon nanobeam and its sidewall. 80
A.2 An angled SEM image of a 6% H-SiQ e-beam resist mask. 86

B.1 T-equivalent circuit of mutually coupled inductors. 90
B.2 Π circuit to tee circuit transformation. 90
B.3 Inductively couple a control line to an external circuit. 91

C.1 The wiring diagram for microwave measurements in ADR. 92
C.2 The wiring diagram for the qubit-resonator experiment. 93
C.3 The wiring diagram for the hole-burning experiment. 94

D.1 Schematic of a series RLC resonator. 96
D.2 Transmission signals of a series RLC resonator. 96

LIST OF TABLES

3.1 Typical lumped-element circuit parameters for a qubit and a FBAR resonator. . 34

4.1 ALD SiO_x growth recipe. 53
4.2 Vapor HF etching process for one cycle. 57
4.3 Vapor HF purge process for one cycle. 57

A.1 PECVD SiO_x growth recipe. 77
A.2 AlN etching recipe. 79
A.3 Silicon etching recipe. 80

ACKNOWLEDGMENTS

It has been a long journey since I came to UChicago to pursue my degree. I am deeply grateful for the help of many people who contribute to this work. I foremost want to thank my advisor, Andrew Cleland, for his guidance and support on my project. When I joined his lab, I know very little about quantum computing, fabrication, microwave engineering, and cryogenic physics. Andrew always has the patience to teach and guide me in the right direction. Without his help and encouragement, I would not have been able to finish this work. In addition to my advisor, I also thank my thesis committee: David Schuster, Paolo Privitera, and Giulia Galli. Their suggestions and comments are always helpful and inspiring, and I thank them for making my project fruitful.

Greg Peairs and Kevin Satzinger are the Ph.D. students moving with Andrew from UCSB to UChicago, and they became our group mentors when we rebuilt our lab. My first project was working with Greg on the quantum transduction experiment, and Greg kindly taught me all the tricks of doing simulations and the knowledge of optics. Kevin spent a lot of time in the PNF cleanroom and figuring out how to operate all the instruments. I learn a lot of fabrication skills from him, and those skills later become the most valuable parts of my entire Ph.D.

Youpeng Zhong and Hung-Shen Chang are our qubit experts. Youpeng built all the electronics in our lab. Without Youpeng, our lab cannot do any qubit experiments. Hung-Shen designed and fabricated our first working qubit at UChicago, and his qubit design then became the prototype of our group. I thank them for their help on my qubit-resonator experiment.

Étienne Dumur and Audrey Bienfait joined our group as postdocs, and we had a wonderful time developing acoustic devices. Étienne helps me a lot on designing my FBAR devices, and I also appreciate his help on debugging my codes. Audrey has always been able to find the right questions, and I am always impressed by how fast she can wrap up the project. I thank them for many fruitful discussions, which inspire me significantly during my Ph.D.

Joel Grebel and Rhys Povey have been infinitely reliable in assistance of all kinds. I am so glad to see their experiments finally work, and I wish you all find amazing positions for your next journey.

More and more talented people have joined our group in the past few years. Haoxiong Yan works not only on the quantum network experiments but also helps me on scaling up our quantum acoustic systems. His knowledge of circuit designs, electronics and quantum simulations is always helpful. I wish you will have productive results in the following few years. Recently, Chris Conner and Gustav Andersson start new projects on designing the next generation of acoustic devices. Yash Joshi and Jacob Miller, on the other hand, work on the next generation of superconducting qubits and resonator devices. I have great confidence in all of you, and I wish you all the best on those ambitious projects. Hong Qiao and Xuntao Wu joined the group recently, but could get several amazing results from their projects. I already see the bright future in front of you, and hope you will all enjoy your journey.

In addition to the support from our lab, I want to thank many people at UChicago. Because I am the person spending the longest time in the cleanroom since it opened, I appreciate the help from the PNF. Peter Duda III is always ready to rescue me from troubles. I would not have been able to figure out my processes without his help. Joe Hermans and Nazar Delegan, our friends from Argonne, take care of the AlN sputtering system. This tool has several bugs and has to be treated extremely carefully. Without their help, I could not sputter AlN films for my experiments. I also want to express my appreciation for Mary Pat McCullough and Sally Wolcott from PME. They always kindly helped me (and our group) deal with all kinds of administrative business and difficulties. Without their help, our group cannot rebuild the lab quickly and smoothly.

Finally, I want to offer special thanks to my teachers, family, and friends who prepared me for this experience. Your ideas, experience and encouragement always inspire and help me to go through this long journey. I wouldn't have gone so far without your support.

ABSTRACT

Phonon modes at microwave frequencies can be cooled to their quantum ground state using conventional cryogenic refrigeration, providing a convenient way to study and manipulate quantum states at the single phonon level. Phonons are of particular interest because mechanical deformations can mediate interactions with a wide range of different quantum systems, including solid-state defects, superconducting qubits, and optical photons when using optomechanically active constructs. Phonons, thus, hold promise for quantum-focused applications as diverse as sensing, information processing, and communication. In this thesis, we describe a piezoelectric quantum bulk acoustic resonator with a 4.88 GHz resonant frequency, which, at cryogenic temperatures, displays large electromechanical coupling strength combined with a high intrinsic mechanical quality factor $Q_i \sim 4.3 \times 10^4$. Using a recently developed flip-chip technique, we couple this resonator to a superconducting qubit on a separate die and demonstrate the quantum control of the mechanics in the coupled system. The resonator lifetime at a single phonon level is measured, which yields a $Q_i \sim 5.43 \times 10^3$. This lower quality factor at a single phonon level is likely due to the two-level system (TLS) defects contamination in the device. To test whether this dissipation comes from the TLS defects, a hole-burning technique is implemented to saturate those defects. As a result, the resonator quality factor is enhanced back to $Q_i \sim 3 \times 10^4$, which demonstrates that TLS defects contribute the dissipation significantly in our device.

CHAPTER 1

INTRODUCTION

Hybrid quantum systems have attracted significant recent interest, for applications in both quantum information processing and quantum engineering and technology [1–7]. Quantum acoustics can play an essential role in hybrid quantum systems, as mechanical degrees of freedom can couple many different types of systems. For example, the research in Ref. [8] demonstrates a quantum transducer using an intermediary nanomechanical resonator that converts the electrical excitation of the superconducting quantum bit (qubit) into a single phonon with a piezoelectric interaction, and then subsequently converts that phonon to an optical photon with an optomechanical resonator. This transducer realizes a new type of hybrid quantum network, and potentially it can be used for building distributed quantum computers. In addition to interacting with optical [9–21] and microwave photons [22–30], many other experiments demonstrate that mechanical waves can be used to interact and control spin ensembles [31, 32], quantum dots [33, 34], artificial atom [35] and two-dimensional materials [36]. Those results show that the mechanical system can be an ideal candidate for developing a quantum communication platform, distributed quantum computers and quantum-limited sensors.

In the past several decades, people were able to build quantum-limited mechanical force sensors [2, 37]. Due to their operating frequency and sensitivity, people have been considering using those sensors as detectors for dark matter [38–40] or gravitational waves [41–43]. For example, many experiments have observed cosmic ray events on superconducting chips. When a cosmic ray or a high-energy particle hits the superconducting chips, it ionizes the substrate and radiates high-energy phonons. Those phonons can propagate a long distance and break the Cooper pairs into quasiparticles, and cause errors in the quantum processor [44–46]. Those errors usually are fatal for quantum computing and need to be removed or corrected if possible. However, from another perspective point of view, if those phonons can be trapped in the mechanical cavity for enough time, we may open a new

window to explore our universe by studying the properties of those captured phonons.

Furthermore, quantum computing can also benefit from mechanical systems. Several proposals have been made for protecting qubits by using a quantum harmonic resonator [47–50]. The idea is to encode qubits into a long-lifetime resonator to minimize qubit energy relaxation decay. Those proposals are demonstrated by coupling a qubit to a long lifetime electromagnetic resonator at cryogenic temperature [51–55]. However, due to the physical size of the electromagnetic resonator ($\sim 50\,\mathrm{mm}^3$), the scalability for building a quantum computer with this approach is technically challenging. The potential solution here is to replace the electromagnetic resonator with a long-lifetime mechanical resonator [56]. Because of slow speed of sound, the mechanical resonator can be made with a much smaller physical size ($\sim 0.1\,\mathrm{mm}^3$), and a compact integrated device can be made easily. Recent research demonstrates that optomechanical resonators can reach a lifetime above 1 ms at both room temperature and cryogenic temperature [57, 58]. As a result, combining quantum acoustics with superconducting circuits becomes an interesting approach to building a quantum computer.

To interact with superconducting circuits, mechanical resonators are usually fabricated on piezoelectric substrates in order to have strong electromechanical interaction. Many groups have developed different types of electromechanical devices for quantum acoustic experiments. For example, surface acoustic wave devices integrated with superconducting circuits can be used for storing and transferring quantum information [24, 26, 28, 35, 59–61]. In addition to surface acoustic wave devices, people can also couple qubit to bulk acoustic resonators, and test several quantum computational protocols with those bulk acoustic devices [22, 23, 25, 27, 30, 62, 63]. However, the long lifetime mechanical resonator is only realized in the optomechanical system and is not demonstrated in the electromechanical system yet. Those phonons of the electromechanical resonators do not approach the lifetimes of photons in electromagnetic cavities [64–66]. The mechanism of this issue is not well-understood. As a result, having a long-lifetime electromechanical resonator with a large

coupling rate is still a challenging problem. In this thesis, we will develop a new electromechanical resonator by using a different material combination. To improve its lifetime, the device is suspended and shielded by phononic crystals to avoid phonon scattering loss. The coupling strength is maintained in the MHz range by using a strong piezoelectric material with an interdigital transducer. With this new approach, we expect the lifetime of an electromechanical resonator can be improved and can still interact with the qubit strongly.

This thesis is structured as follows: In chapter 2, we introduce the theory for understanding superconducting circuits and mechanical resonators. This theory helps us to design our experiments. In chapter 3, we discuss the circuit design, including coupling the qubit to a mechanical resonator. In chapter 4, we describe the fabrication process of our devices, especially focusing on the process of making our electromechanical resonators. In chapter 5, we show the characterization of our resonators and several related experimental results. In chapter 6, we conclude the thesis with the outlook of several potential experiments that can be performed in the future.

CHAPTER 2

THEORY

For our experiment, we want to develop a long-lifetime electromechanical resonator, which can be potentially used for storing quantum information. The mechanical resonator is fabricated on the bilayer membranes, where a piezoelectric material is deposited on a thin silicon device layer. The resonator consists of an interdigital transducer (IDT) and acoustic mirrors. The IDT is used for generating mechanical waves, and the mechanical wave can be trapped by two acoustic mirrors to create a Fabry-Pérot cavity. In order to study the property of the mechanical resonator at the quantum regime, we couple the resonator to a superconducting qubit, and use the qubit to control and manipulate the phonon in the resonator.

In this chapter, we introduce the necessary theory to understand superconducting circuits and mechanical devices. Understanding this theory is very important since it can guide us in choosing materials, designing circuits and performing experiments. Several good references for superconducting circuits can be found in Ref. [67–74], and for mechanical devices can be found in Ref. [75–81].

2.1 Superconducting circuits

2.1.1 LC resonator

Before discussing qubits, we first take a look at simple harmonic oscillators. For an LC circuit shown in Fig. 2.1 (a), its Hamiltonian is given by

$$H = \frac{Q^2}{2C} + \frac{\Phi^2}{2L} \tag{2.1}$$

where Q is the charge stored in the capacitor C and Φ is the flux in the inductor L. This LC resonator can be quantized by promoting charge and flux as quantum operators obeying

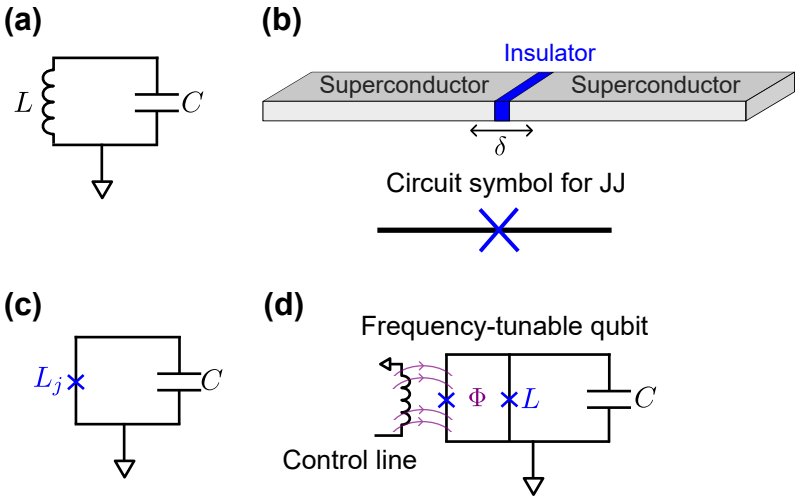

Figure 2.1: (a) Schematic of a LC resonator. (b) Top: Schematic of a Josephson junction, comprising a thin insulator barrier (blue) sandwiched by the two superconductors. The phase difference between the two superconductors is denoted by δ. Bottom: circuit symbol for a Josephson junction. (c) Schematic of a non-linear LC resonator. (d) Circuit diagram for a frequency-tunable qubit. The control line can generate the external flux (purple) into the SQUID and thus change the qubit frequency.

the canonical commutation relation

$$[\hat{\Phi}, \hat{Q}] = j\hbar. \tag{2.2}$$

where $j \equiv \sqrt{-1} = i$. With this relation, we can define the creation and annihilation operators as

$$a = \frac{j}{\sqrt{2\hbar\omega_0 L}}\hat{\Phi} + \frac{1}{\sqrt{2\hbar\omega_0 C}}\hat{Q}, \tag{2.3}$$

$$a^\dagger = \frac{-j}{\sqrt{2\hbar\omega_0 L}}\hat{\Phi} + \frac{1}{\sqrt{2\hbar\omega_0 C}}\hat{Q}, \tag{2.4}$$

where $\omega_0 = 1/\sqrt{LC}$. The Hamiltonian for a quantum harmonic oscillator can then be rewritten as

$$H = \hbar\omega_0 \left(a^\dagger a + \frac{1}{2}\right), \tag{2.5}$$

and its eigenstates satisfy

$$H|m\rangle = \hbar\omega_0 \left(m + \frac{1}{2}\right)|m\rangle = E_m|m\rangle, \tag{2.6}$$

where $|m\rangle$ is known as a Fock state and E_m is its corresponding energy. From Eq. 2.6, we know that the corresponding energy levels of a LC resonator are equally spaced by $\hbar\omega_0$. Detailed information about quantum harmonic oscillators and their properties can be found in Ref. [68, 73].

2.1.2 Superconducting qubits

An ideal qubit is a two-level system that is measured and controlled. In the typical LC circuit, all the elements are linear, and the energy levels are equally spaced. This becomes an issue since we want to focus on just a two-level system with a specific energy level splitting of $\hbar\omega_{ge}$. The solution to this problem is to introduce a nonlinear element into the circuits, so the energy levels are no longer spaced equally. This can be achieved if we have Josephson junctions (JJs), which serve as a non-linear inductor.

Josephson junctions can be made by growing a thin oxide layer between two superconductors (see Fig. 2.1). This allows the superconducting phase to be different on either side of the oxide barrier. This phase difference δ is related to the current I and the voltage V by the Josephson relations [82]:

$$I = I_c \sin(\delta) \tag{2.7}$$

$$V = \frac{\Phi_0}{2\pi}\frac{d\delta}{dt} \tag{2.8}$$

where $\Phi_0 = h/2e$ is the flux quantum and I_c is the critical current of the junction. Now we differentiate Eq. 2.7 and insert the result into Eq. 2.8. We can then define the inductance

L_j by

$$V = \frac{\Phi_0}{2\pi I_c}\frac{1}{\cos(\delta)}\frac{dI}{dt} = \frac{L_{j0}}{\cos(\delta)}\frac{dI}{dt} \equiv L_j\frac{dI}{dt} \tag{2.9}$$

where $L_{j0} = \frac{\Phi_0}{2\pi I_c}$. With this formula, we can observe that the Josephson junction is a non-linear inductor with a value depending on $\cos(\delta)$. The energy stored in the JJ can be calculated by integrating VI over time,

$$E = \int_{-\infty}^{t} VIdt' = -E_J\cos(\delta) \tag{2.10}$$

where $E_J = I_c\Phi_0/2\pi$ is called the Josephson energy. If we connect this inductor with a capacitance, we can engineer a non-linear LC resonator, as shown in Fig. 2.1 (c). The Hamiltonian of the non-linear LC resonator is given by [67]

$$H = \frac{Q^2}{2C} - E_J\cos(\delta) \tag{2.11}$$

$$= 4E_C n^2 - E_J\cos(\delta) \tag{2.12}$$

where $n = Q/2e$ is the number of Cooper pairs and $E_C = e^2/2C$ is the charge energy. Assuming δ is small, we can Taylor expand and rewrite the Hamiltonian as

$$H \approx 4E_C n^2 + E_J\frac{\delta^2}{2} - \frac{\delta^4}{24} \tag{2.13}$$

$$= \sqrt{8E_J E_C}\left(a^\dagger a + \frac{1}{2}\right) - \frac{E_C}{12}(a + a^\dagger)^4, \tag{2.14}$$

where

$$\delta = \left(\frac{2E_C}{E_J}\right)^{1/4}(a + a^\dagger), \tag{2.15}$$

$$n = -j\left(\frac{E_J}{8E_C}\right)^{1/4}(a - a^\dagger). \tag{2.16}$$

Here, the constant and higher-order terms are dropped off for brevity. The eigenenergy of this Hamiltonian is then given by [67]

$$E_m = m\sqrt{8E_J E_C} - \frac{E_C}{12}(6m^2 + 6m) \tag{2.17}$$

where m is an integer corresponding to the energy level of the nonlinear LC circuit. The last term in the Eq. 2.17 comes from the nonlinearity of the JJ, and it makes the energy levels not equally spaced. The energy levels of the non-linear LC resonator are shown in Fig. 2.2. The E_0, E_1 and E_2 correspond to the energy levels of the resonator ground state $|g\rangle$, first excited state $|e\rangle$ and second excited state $|f\rangle$, respectively. The resonator frequency ω_{ge} is then determined by

$$\omega_{ge} = \frac{E_1 - E_0}{\hbar}. \tag{2.18}$$

The typical value of ω_{ge} is designed to be about 5 GHz. The anharmonicity η of this resonator is defined by the frequency difference between $|g\rangle$-$|e\rangle$ and $|e\rangle$-$|f\rangle$ transitions,

$$\eta = \omega_{ef} - \omega_{ge}. \tag{2.19}$$

The typical value of η is about $-200\,\mathrm{MHz}$. With the anharmonicity, we can use the lowest two energy levels ($|g\rangle$ and $|e\rangle$) as the computational basis, and thus treat this nonlinear LC circuit as a qubit.

Now, if a single junction is replaced by a junction pair (so-called superconducting quantum interference device, or SQUID [83]), and the junction pair are shunted with a capacitance, we can create a frequency-tunable qubit. By using an external control line to change the flux in the junction loop, the equivalent inductance can be controlled and thus the qubit frequency can be tunable. In this thesis, the frequency-tunable qubit used in our experiments is called an Xmon [84], and its circuit geometry is shown in Fig. 2.1 (d). The typical value for the

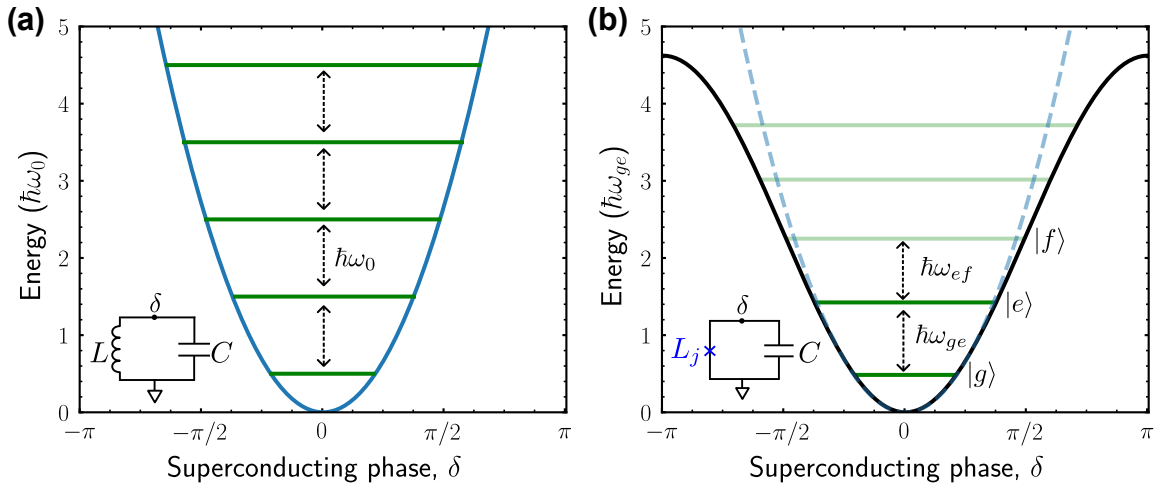

Figure 2.2: (a) Energy potential (blue) for a simple harmonic LC circuit. The energy levels (green) are equally spaced by $\hbar\omega_0$. (b) Energy potential (black) for a nonlinear LC circuit. The nonlinearity of the circuit makes the potential deviate from the potential of the linear LC circuit (blue dashed line). The energy levels are not equally spaced, and the lowest two levels ($|g\rangle$ and $|e\rangle$) are usually used as the computational basis. The insets show the corresponding circuit diagrams.

Xmon capacitance C_q is about 90 fF.

2.1.3 Qubit readout

Qubit measurement is a very challenging problem since the qubit is very fragile and sensitive to noise. We want to isolate the qubit from the environment but somehow extract the information from it. A method to resolve this difficulty involves coupling a resonator to the qubit and using the dispersive shift of the resonator to know the state of the qubit [85]. Several experiments [51, 86, 87] have demonstrated non-demolition quantum measurement by using this method.

To understand this method, we need to look at the Jaynes-Cummings model, which describes how a two-level system interacts with a harmonic oscillator [88]. The Jaynes-Cummings Hamiltonian is given by [89]

$$H_{JC} = \hbar\omega_r a^\dagger a - \frac{1}{2}\hbar\omega_q\sigma_z + \hbar g(\sigma_- + \sigma_+)(a^\dagger + a) \tag{2.20}$$

where ω_r and ω_q are the resonant frequencies of the oscillator and qubit, a and σ_- are the annihilation operators of the oscillator and qubit excitations, respectively, σ_z is the qubit Pauli operator, and g is the coupling strength. By using the rotating-wave approximation given by [68, 73, 89], we can rewrite the Jaynes-Cummings Hamiltonian as

$$H_{JC} = \hbar\omega_r a^\dagger a - \frac{1}{2}\hbar\omega_q\sigma_z + \hbar g(\sigma_- a^\dagger + \sigma_+ a) \tag{2.21}$$

The $\sigma_- a$ and $\sigma_+ a^\dagger$ terms are dropped off due to the violation of the excitation number conservation. We also define the detuning $\Delta = \omega_q - \omega_r$. If $\omega_r \gg |\Delta| \gg |g|$, we are in the so-called dispersive limit. In this regime, we can apply a unitary transformation $U = e^{\frac{g}{\Delta}(a^\dagger\sigma_- - a\sigma_+)}$ and rewrite a new Hamiltonian H'_{JC} given by [89]

$$H'_{JC} = UH_{JC}U^\dagger = \hbar\omega_r a^\dagger a - \frac{1}{2}\hbar\omega_q\sigma_z - \hbar\frac{g^2}{\Delta}\sigma_z a^\dagger a \tag{2.22}$$

$$= \hbar(\omega_r + \chi\sigma_z)a^\dagger a - \frac{1}{2}\hbar\omega_q\sigma_z \tag{2.23}$$

$$= \hbar\omega_r a^\dagger a - \frac{1}{2}\hbar(\omega_q - 2\chi a^\dagger a)\sigma_z \tag{2.24}$$

where the dispersive shift $\chi \equiv -\frac{g^2}{\Delta}$. If we consider the second excitation ($|f\rangle$ state) of the qubit, the dispersive shift is modified by a factor [67] related to the anharmonicity η

$$\chi = \frac{-g^2}{\Delta}\frac{1}{1+\Delta/\eta}. \tag{2.25}$$

In Eq. 2.23, we can see that the oscillator frequency is shifted by the $\pm\chi$ based on the state of the qubit. As a result, by measuring the readout resonator and monitoring its frequency, we can know the state of the qubit. Furthermore, the qubit frequency can also be shifted based on the number of excitations in the oscillator ($\omega'_q = \omega_q - 2\chi a^\dagger a$), as shown in Eq. 2.24. This useful formula provides us with a method to measure the population of the oscillator.

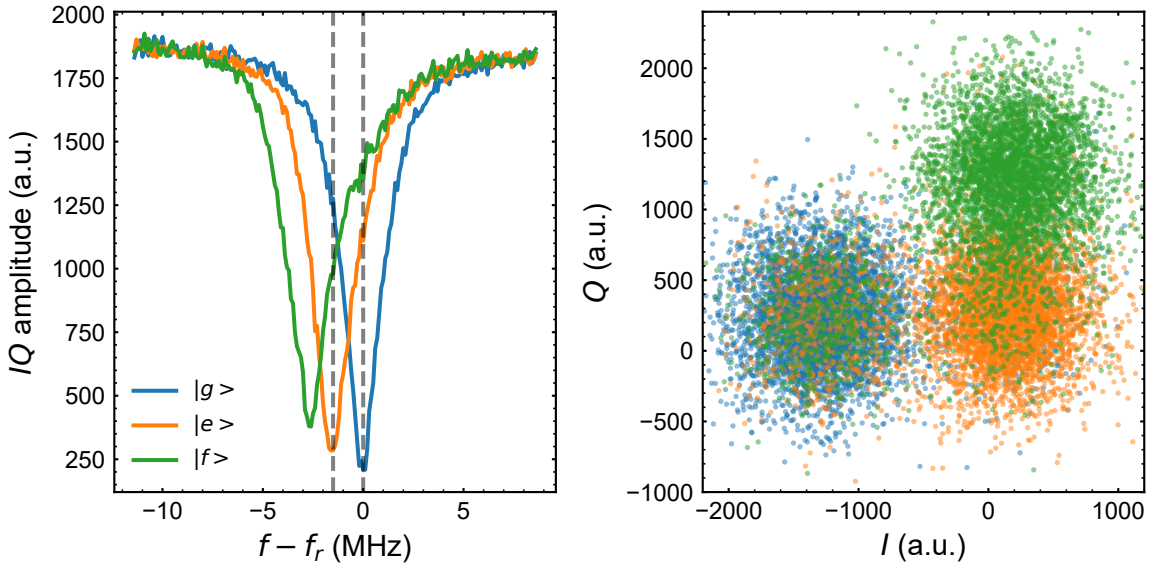

Figure 2.3: Left: readout transmission signal from our typical qubit device. The transmission signal is represented by a complex number $I + jQ$. The resonant frequency f_r is shifted due to different qubit states. The difference between two dashed lines indicates $2\chi \sim 1.5\,\mathrm{MHz}$. Right: Prepared qubit states are plotted in the complex I-Q plane. The qubit ground state ($|g\rangle$), first ($|e\rangle$) and second ($|f\rangle$) excited states correspond to different regions in the I-Q plane.

In Fig. 2.3, we show the dispersive shift of a readout resonator[1]. Although here we use the readout resonator as an example, the Jaynes-Cummings model is valid for coupling qubit to any type of harmonic oscillator [27, 28, 85], including the mechanical resonator we will discuss in this thesis.

In the typical design, the readout resonator is a quarter-wave coplanar waveguide (CPW) resonator, with one end capacitively coupled to the qubit and the other end inductively coupled to a transmission line. The energy decay rate κ_r of the readout resonator to the transmission line usually is designed to be a few MHz. This κ_r also needs to match 2χ to have optimal visibility [69]. Due to this energy decay rate, the qubit can still lose its energy through the transmission line, and thus the κ_r cannot be too large[2]. This limits how fast we can read out the qubit state. To avoid this limitation, one of the solutions is to use a

1. The measured signal has amplitude and phase information, which is a complex number that can be mapped into quadratures I and Q components [69].

2. This energy decay rate γ is given by [90], and can be approximated as $\gamma = \frac{g^2\kappa_r}{\Delta^2}$.

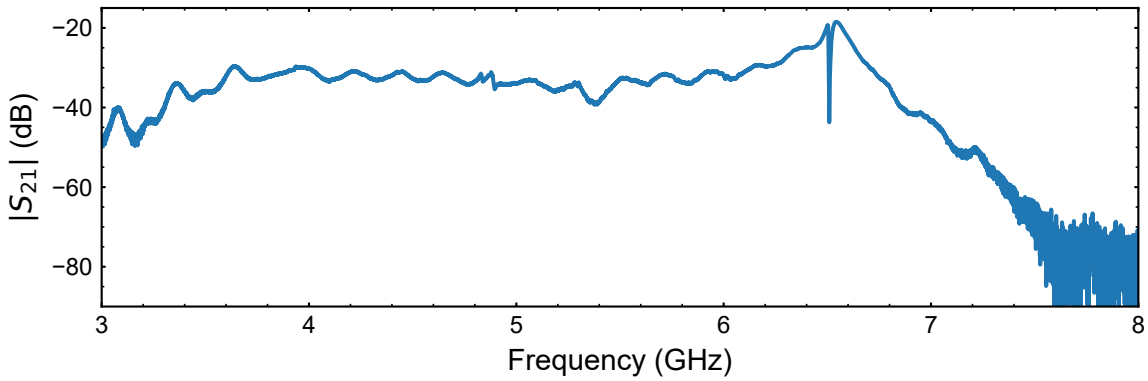

Figure 2.4: The microwave transmission signal of the readout line, measured by a vector network analyzer (VNA). The Purcell filter feature (broad peak near 6.5 GHz) aligns with the readout resonator frequency with a narrow dip at about 6.5 GHz.

Purcell filter to protect a qubit [69, 91–93], so its energy doesn't decay too quickly even with a larger κ_r. The Purcell filter is a bandpass filter, which allows the energy to be transferred only near the readout frequency but suppresses it elsewhere. In this thesis, the Purcell filter is designed to be a half-wave CPW resonator weakly coupled ($Q_{c,\text{in}} \sim 2000$) to the input line while strongly coupled ($Q_{c,\text{out}} \sim 20$) to the output line[3]. This filter allows us to enhance κ_r by a factor of $Q_{c,\text{out}}$ while keeping the qubit lifetime unchanged. The typical microwave transmission signal of a Purcell filter with a readout resonator is shown in Fig. 2.4. Detailed information about designing Purcell filter can be found in Ref. [69].

2.1.4 Qubit control lines

With a proper design of the qubit anharmonicity, we can always address the lowest two energy levels as the computational basis. As a result, we ignore the $|f\rangle$ state, and the quantum state of a qubit can be expressed as

$$\psi = \cos(\theta/2)|g\rangle + \sin(\theta/2)e^{j\phi}|e\rangle. \tag{2.26}$$

3. Detailed discussion about quality factors can be found in the Appendix. D.

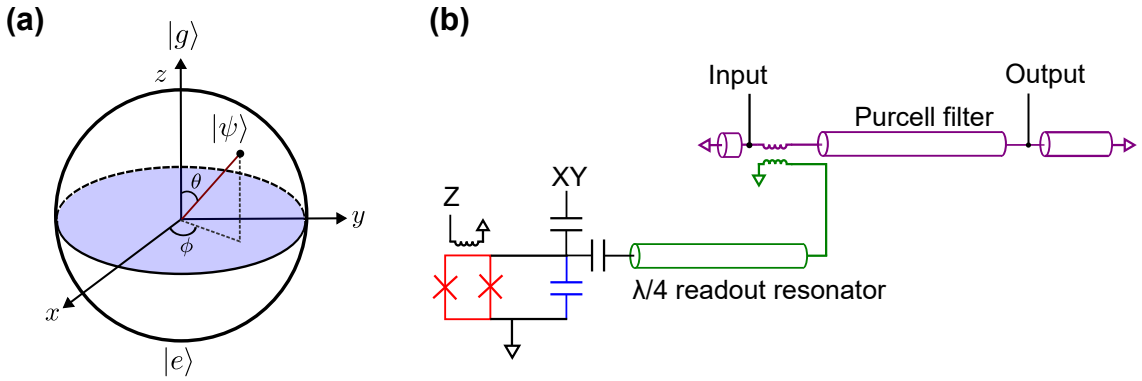

Figure 2.5: (a) Qubit state represented on a Bloch sphere. (b) Qubit control lines (black) and readout schematic. The positions of the input and output line on the Purcell filter (purple) determine Q_{out} and Q_{in}. The Xmon qubit consists of a SQUID (red) in parallel with a capacitance (blue). The readout resonator (green) is a quarter-wave resonator.

To have better intuition, we can plot a qubit pure state on the surface of a unit sphere, which is called the Bloch sphere, as shown in Fig. 2.5. In this presentation, the θ and ϕ correspond to the polar and azimuthal angle of the unit vector on the Bloch sphere. Frequency-tunable qubits are usually controlled by an XY control line and a Z control line. The XY-line is capacitively coupled to the qubit, and the on-resonant microwave pulse is sent via the XY-line to drive the qubit. This is equivalent to rotating the qubit state along any axis on the equator of the Bloch sphere. The Z-line is inductively coupled to the SQUID loop of a qubit. The fast DC pulse is sent via a Z-line to the SQUID to change the qubit frequency. This is equivalent to rotating a qubit along the z-axis of the Bloch sphere. The circuit of the Xmon qubit, control and readout lines are shown in Fig. 2.5. Detailed information about designing the control lines can be found in Ref. [69, 73]

2.1.5 Capacitive and inductive coupling

When we couple two microwave electromagnetic resonators, the natural ways are using either capacitive or inductive coupling. The corresponding circuit diagrams are shown in Fig. 2.6. Capacitive coupling requires one element to drive a voltage across other elements, while inductive coupling requires one element to drive a current through other elements. The

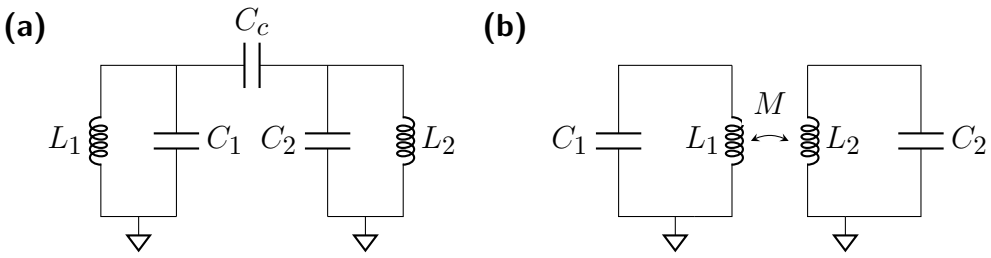

Figure 2.6: The circuit diagrams for (a) capacitive and (b) inductive coupling of two resonators.

coupling strength g_c for capacitive coupling and g_l for inductive coupling are given by [74]

$$g_c = \frac{1}{2}\frac{C_c}{\sqrt{(C_1 + C_c)(C_2 + C_c)}}\sqrt{\omega_1\omega_2} \tag{2.27}$$

and

$$g_l = \frac{1}{2}\frac{M}{\sqrt{L_1 L_2}}\sqrt{\omega_1\omega_2} \tag{2.28}$$

respectively. Here, ω_1 and ω_2 are the resonant frequencies of the two resonators. Both formulas can be applied to a nonlinear resonator or a qubit, if we replace the linear inductor with a nonlinear element such as a Josephson junction.

The discussion above refers to fixed coupling. Because of frequency crowding, this kind of coupling becomes harder to implement when the quantum processor becomes more complex. To avoid this issue, different kinds of tunable couplers have been created and implemented in quantum processors [94–100]. With those couplers, the interactions between two resonators can be turned off even if they are tuned at the same frequency. However, the tradeoff here is that we need more control lines to individually control the coupler, which is also a challenging problem for scaling up the quantum processor. The tunable coupler we use in this thesis was first demonstrated in Ref. [97], where two qubits were inductively coupled. This combination of an Xmon qubit and a tunable coupler is referred to as a Gmon qubit. Our group then adopted this technique and coupled the Gmon qubit to a surface acoustic

wave (SAW) resonator [24]. Here, we will follow the same strategy and couple the Gmon qubit to a thin-film bulk acoustic resonator (FBAR). The detailed circuit design is discussed in chapter 3.

2.2 Mechanical device

In this section, we sketch a discussion from several references [75–78, 80, 81], and use the theory of solid mechanics to understand mechanical waves and piezoelectric response. Several critical elements introduced here will be used later for building our mechanical device.

2.2.1 Elastic waves in a solid

Wave propagation in a solid can be determined by the wave equation subject to the boundary condition representing the device geometry. In solid mechanics, the wave equation for a solid is given by the Newtonian equations

$$\nabla \cdot \mathbf{T}(\mathbf{r}) = -\rho\omega^2 \mathbf{u}(\mathbf{r}, t), \tag{2.29}$$

$$T_{ij} = c_{ijkl} S_{kl} \tag{2.30}$$

$$S_{kl} = \frac{1}{2}\left(\frac{\partial u_k}{\partial x_l} + \frac{\partial u_l}{\partial x_k}\right) \tag{2.31}$$

where $\mathbf{u}(\mathbf{r}, t)$ is the relative displacement for a cube at a given time t, and the cube oscillates at the frequency ω. The $\mathbf{T}(\mathbf{r})$ is the stress tensor and can be connected to the strain tensor $\mathbf{S}$ by the stiffness matrix $\mathbf{c}$. The indices i, j, k, l are in the range from 1 to 3, indicating three different spatial directions $\hat{x}, \hat{y}$ and $\hat{z}$.

For a plane wave propagating in an infinite isotropic elastic medium, the displacement $\mathbf{u}(\mathbf{r}, t)$ of the wave takes the form

$$\mathbf{u}(\mathbf{r}, t) = \mathbf{u_0} e^{-j(\mathbf{k}\cdot\mathbf{r} - \omega t)} \tag{2.32}$$

where ω is the angular frequency and $\mathbf{k}$ is the wavevector. The direction of $\mathbf{u_0}$ and $\mathbf{k}$ determines the polarization of the wave.

Many quantum acoustic experiments are using surface acoustic waves [24, 26, 28, 35, 60], which is a unique wave propagating only at the surface of the solid. We can derive its profile by using the wave equation with boundary conditions. We consider a surface acoustic Rayleigh wave propagating on the surface of a semi-infinite isotropic solid. The surface ($z = 0$) of that solid has a stress-free boundary condition. Since the wave is confined on the surface of a solid, we expect its wave amplitude decays exponentially into the solid. The characteristic decay length is approximately equal to its wavelength. Putting all the requirements together, the Rayleigh surface acoustic wave takes a form given by [76]

$$\mathbf{u}(\mathbf{r}, t) = A(u_x\hat{x} + u_y\hat{y} + u_z\hat{z})e^{-j(k_R x - \omega t)} \tag{2.33}$$

$$u_x = \gamma e^{ak_R z} - e^{bk_R z} \tag{2.34}$$

$$u_y = 0 \tag{2.35}$$

$$u_z = j\left(\gamma a e^{ak_R z} - \frac{1}{b}e^{bk_R z}\right) \tag{2.36}$$

where a, b and γ are positive and real numbers, A is the displacement amplitude and k_R is the wavevector of the Rayleigh surface acoustic wave. Detailed information about the Rayleigh surface acoustic wave can be found in Ref. [75, 76].

In this thesis, however, we focus on the other type of wave: the Lamb wave. Here, we consider a plane wave propagating in the x-direction in a thin isotropic semi-infinite plate. The thickness $2h$ of the plate is less than or equal to the wavelength, and the normal vector of the plate is pointed into the z-direction. The wave properties can be obtained by using a similar approach [101]. In this case, the top and the bottom surfaces are stress-free, and we have

$$T_{zz}(z = \pm h) = T_{xz}(z = \pm h) = 0 \tag{2.37}$$

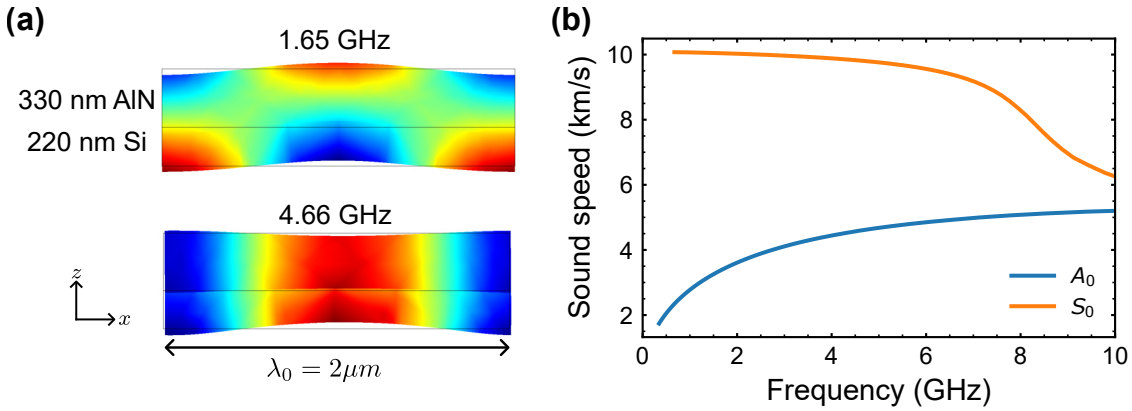

Figure 2.7: Lamb wave in a bilayer membrane (330 nm AlN on 220 nm Si). (a) Volumetric strain profile of A_0 (top) and S_0 (bottom) modes obtained from finite element simulations, with exaggerated deformation. (b) The sound speed for the A_0 and S_0 modes.

With those constraints, the Lamb wave is divided into two categories: symmetric wave (S_n) and anti-symmetric wave (A_n), where n is the mode index and is integer-valued. Their speeds and displacement profiles are quite different, and their properties depend strongly on the ratio of film thickness to wavelength. In Fig. 2.7, we show the profile of the fundamental A_0 and S_0 modes when the wavelength $\lambda_0 = 2\,\mu$m and the thickness $h = 550$ nm in aluminum nitride (AlN) on silicon (Si). In the experiment we will discuss later, we focus on the S_0 mode since its frequency is about 5 GHz and is easier to couple to a qubit.

2.2.2 Piezoelectricity

Certain materials exhibit a unique property, piezoelectricity, where their crystals can deform strongly when an electric field is applied. Furthermore, when their crystals are stretched, special charge distribution can be generated. In other word, for piezoelectric substrates, the strain $\mathbf{S}$, stress $\mathbf{T}$ and electric field $\mathbf{E}$ are coupled together, and their relations are given by

$$\mathbf{D} = \boldsymbol{\epsilon} \cdot \mathbf{E} + \mathbf{e} \cdot \mathbf{S} \tag{2.38}$$

$$\mathbf{T} = -\mathbf{e}^{\mathbf{t}} \cdot \mathbf{E} + \mathbf{c} \cdot \mathbf{S} \tag{2.39}$$

where $\mathbf{D}$ is the electric displacement, $\boldsymbol{\epsilon}$ is the dielectric tensor, $\mathbf{e}$ is the piezoelectric tensor and $\mathbf{e^t}$ denotes the transpose of $\mathbf{e}$. Piezoelectricity provides us with a unique way to detect mechanical vibrations with electrodes. Furthermore, we can generate mechanical vibrations by applying a voltage to a transducer, which will be discussed in the next section.

So far, we have discussed the wave propagating in an isotropic material. For piezoelectric substrates, a similar wave can exist. In this case, we need to consider the electrical boundary condition on the surface and the anisotropy of the piezoelectric substrate. The wave velocities for a free surface (v_f) and a metalized surface (v_m) on the piezoelectric substrate are different. For a metalized surface, the electrical field is shorted at the surface, and this would slow down the velocity v_m. The difference between the velocities is related to the piezoelectric coupling strength of the material. The electromechanical coupling coefficient K^2 is defined by

$$K^2/2 \equiv (v_f - v_m)/v_m \tag{2.40}$$

For most piezoelectric materials, K^2 is less than one percent [76, 78]. In our experiment, we choose aluminum nitride (AlN) since it is a relatively strong piezoelectric material ($K^2 \sim 0.01$), and we can control its properties by using a commercial sputter tool. Besides, by combining AlN with thin silicon films, this material combination also opens the possibilities for optical experiments and building hybrid quantum systems [8, 17].

2.2.3 Interdigital transducer

A Lamb wave or a SAW in a piezoelectric substrate can be detected and launched by electrodes. An interdigital transducer is an array of signal and ground electrodes that match the mechanical wave profile. The wavelength λ_0 of the mechanical wave is determined by the pitch (p) of the electrodes. When voltage is applied to the electrodes, an electrical field is generated between the transducer signal and ground electrodes. As we have discussed

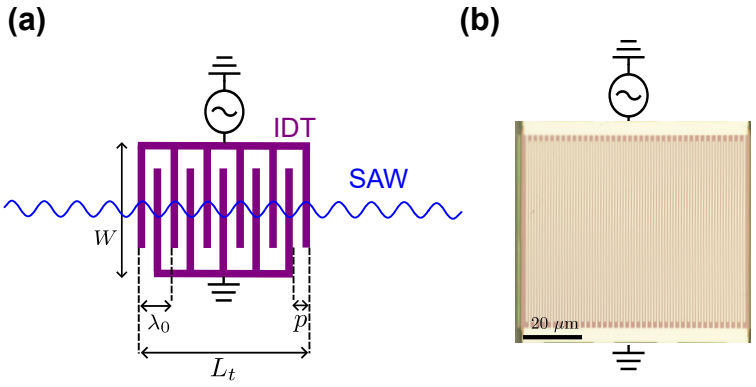

Figure 2.8: (a) Schematic of the single-electrode transducer connected to an external source. (b) An optical image of an IDT.

above, this electric field can introduce stress to the piezoelectric substrate, and thus the mechanical wave can be launched if the frequency of the electric field matches that of the mechanical wave. Furthermore, when the piezoelectric substrate is deformed by mechanical waves, IDT can detect deformations due to the induced voltages, and thus captures the mechanical waves. For the Lamb wave, both symmetric and anti-symmetric waves can be generated by the IDT. We design our device such that the S_0 mode is at about 5 GHz, while the A_0 mode is at about 2 GHz. When driving IDT at the S_0 mode frequency, any energy in the A_0 mode is expected to be a loss since the A_0 mode is not phase-matched to the IDT.

The single-electrode transducer has an electrode pitch equal to half of the wavelength ($p = \lambda_0/2$), as shown in Fig. 2.8. The IDT aperture is labeled by W and its width L_t is determined by the product of the electrode finger pairs N_p and the wavelength ($L_t = N_p\lambda_0$). To better understand the IDT, we can look at its electrical admittance

$$Y_t = G_a(\omega) + jB_a(\omega) + j\omega C_t \tag{2.41}$$

where $G_a(\omega)$ and $B_a(\omega)$ are the acoustic conductance and susceptance respectively, and C_t is the IDT geometric capacitance [76]. The conductance G_a and B_a are related to the acoustic response, where electrical energy is converted into mechanical vibrations. We consider the simplest case where the IDT is an array of lossless and non-reflective single-finger electrodes,

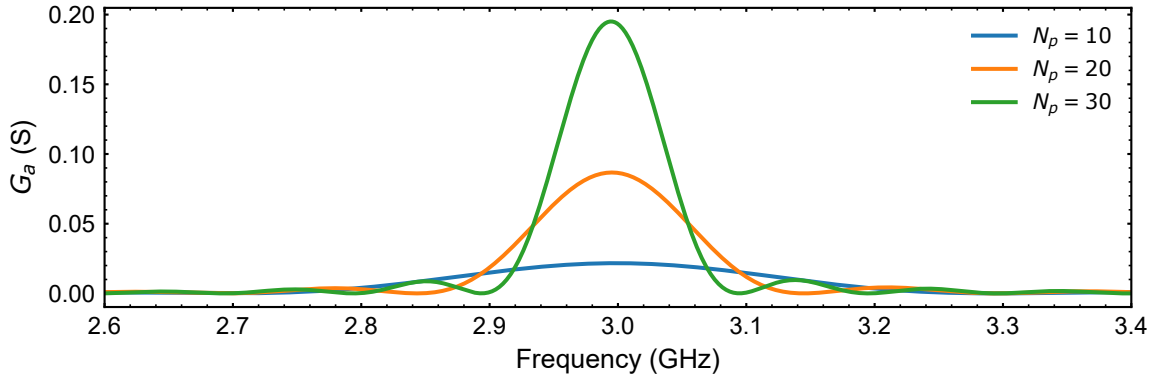

Figure 2.9: The IDT electrical response for the different number of finger pairs.

and it has angular frequency ω_t, aperture W and electrode finger pairs N_p. The G_a is then given by [76]

$$G_a(\omega) = G_0 \left[\frac{\sin(X)}{X}\right]^2 \approx K^2 N_p^2 \omega_t W \epsilon_\infty \left[\frac{\sin(X)}{X}\right]^2 \tag{2.42}$$

where ϵ_∞ is the effective dielectric constant of the substrate and $X = N_p \pi \frac{\omega - \omega_t}{\omega_t}$. The bandwidth of the IDT is approximately equal to $\omega_t/(2\pi N_p)$. Based on this formula, having more IDT finger pairs enhances the IDT response, at the price of narrowing its bandwidth (see Fig. 2.9). For AlN, the product of $K^2\epsilon_\infty$ is about 20 times larger than for quartz or gallium arsenide. As a result, the AlN transducer can have a broadband acoustic response with only a few finger pairs.

2.2.4 Loss mechanisms for surface acoustic wave devices

For conventional SAW devices, there are four common loss mechanisms [76]. The first one is beam steering, which is related to the crystalline orientation of the substrate. Anisotropic materials can exhibit beam steering, which causes misalignments between the direction of the SAW and its wavevector $\mathbf{k}$. For the SAW transducer, the $\mathbf{k}$ is determined by the transducer geometry, and its direction usually is designed to be perpendicular to the IDT fingers. When driving the IDT, a specific frequency is selected and its wavevector $\mathbf{k}$ is determined by the

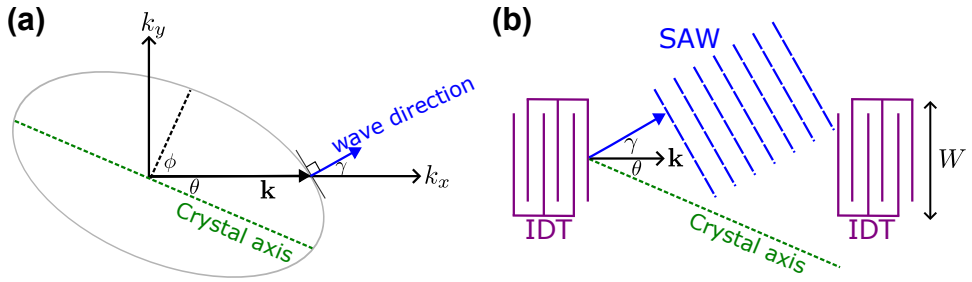

Figure 2.10: (a) Schematic slowness curve (gray), showing the k as a function of ϕ. The angle θ indicates the misalignment of the crystal axis (green) with the device. The angle γ is the beam steering angle. (b) Schematic diagram shows the SAW propagation direction (blue) if beam steering is included.

dispersion relation $\omega(\mathbf{k})$. However, the magnitude $|\mathbf{k}|$ depends on the properties of the substrate, and the wavevector is not always aligned with the propagating direction. This idea can be explained by looking at the slowness curve, which is a polar plot of the inverse speed $(1/v)$ versus angle ϕ in the $\mathbf{k}$-space (see Fig. 2.10). By using the parabolic approximation [76], we have

$$k_x = k(\phi = 0) - ak_y - \frac{1}{2}bk_y^2 \tag{2.43}$$

$$a = \tan(\gamma) \tag{2.44}$$

$$b = \left(1 + \frac{d\gamma}{d\theta}\right)\sec^2\gamma \tag{2.45}$$

For a given crystal orientation and propagation direction, a, b and $k(\phi = 0)$ are constants. The second term on the right-hand side of Eq. 2.43 causes the beam steering, and this effect can be minimized if the crystal axis is aligned to the SAW propagation direction (normal to the IDT finger orientation). The third term on the right-hand side of Eq. 2.43 causes diffraction, and this is the second loss mechanism for SAW devices. The diffraction happens even if the crystal axis is aligned with the wavefront ($a = 0$ and $b = 1$). For the SAW resonator device, by making the IDT aperture W longer, the diffraction loss can be suppressed [78]. For sputtered AlN films, the AlN grains are randomly distributed in-plane orientation and thus should have a very small beam steering effect. For our typical device,

we design the device such that the IDT aperture is long enough to alleviate the diffraction loss.

The third loss mechanism for SAW devices is the two-level system (TLS) defects in the materials. Those defects create loss channels. For example, if we make a SAW resonator, the energy stored in the resonator can leak out to the TLS defects and thus the quality factor of the resonator is decreased. The origin of the TLS defects is not well understood, but the defects are found to be related to the damage of the surface during the fabrication or material growth. If the participation of the surface is decreased or eliminated, the lifetime of the resonator can be enhanced. This idea has been demonstrated in a wafer-scale bulk acoustic resonator [23, 25], where the standing wave is created between the top and bottom surfaces of a wafer. Instead of confining the mechanical wave on the surface of a substrate, the wave in this type of resonator is confined in the bulk volume, and thus it is less sensitive to the loss at the surface and interfaces.

The final loss mechanism for SAW devices is phonon scattering. The phonon scattering comes from the surface asperities, such as dust, contamination, crystal defects and metal features of IDT and acoustic mirrors. For many materials, the dominant asperities are the metal features of IDT and mirrors [80]. This loss mechanism can be minimized if we can make a freely-suspended device. Besides, to avoid the loss from the metal features of acoustic mirrors, we can replace the metal mirror structures with phononic crystals (PCs), as PC is demonstrated to be a low-loss acoustic element optomechanical resonators [58]. These two potential solutions lead to our new device design and will be discussed in the thesis.

2.2.5 Phononic crystals

Waves in periodic structures can be understood by Bloch's theorem, which states that waves can be described as a product of a plane wave and a function with a periodicity of the structure. In other words, the relative displacement $\mathbf{u}(\mathbf{r})$ has translation symmetry and is

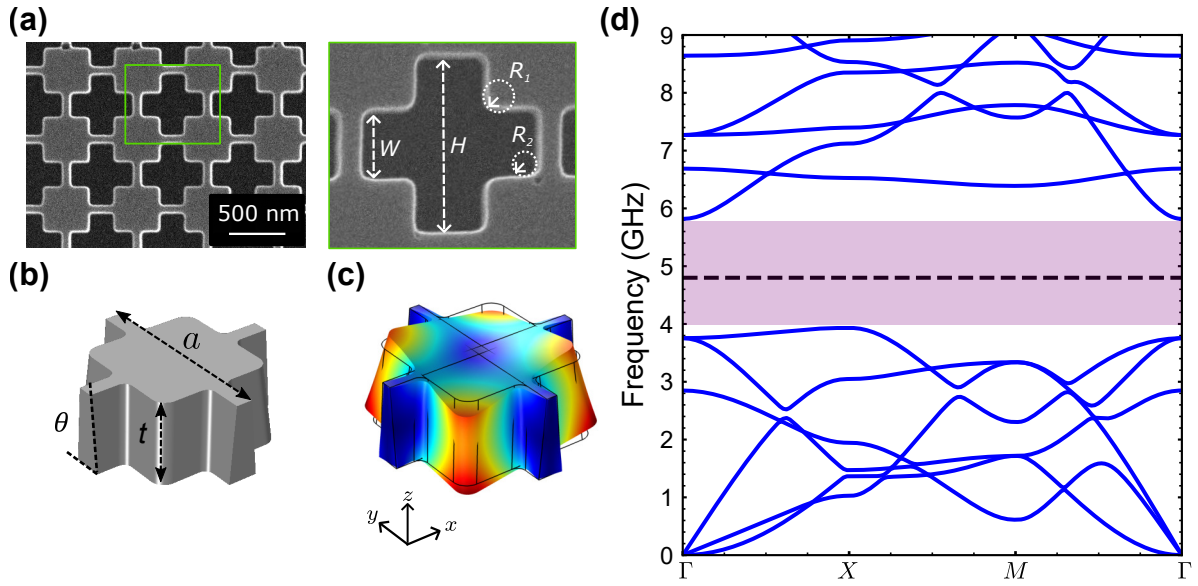

Figure 2.11: (a) The electron scanning microscope (SEM) images of a phononic crystal. Left: the phononic crystal array. Right: A closer look at the cross shape. (b) Schematic of the PC structure. The crystal geometric parameters include $W = 183\,\text{nm}$, $H = 486\,\text{nm}$, $R_1 = 36\,\text{nm}$, $R_2 = 26\,\text{nm}$, $a = 550\,\text{nm}$, $t = 220\,\text{nm}$ and $\theta = 85°$. (c) Volumetric strain profile (with exaggerated deformation) of the $\Gamma = 0$ mode at about 5.7 GHz. (d) The band structure of a unit cell, plotted along $\Gamma \to X \to M \to \Gamma$ in reciprocal space. The bandgap is located between 4 to 6 GHz (shaded purple region). The solid blue lines show the different mechanical modes of the crystal. The dashed line indicates the resonant mode confined in the phononic crystals.

given by

$$\mathbf{u}(\mathbf{r}) = \mathbf{u}_\mathbf{k}(\mathbf{r})e^{j\mathbf{k}\cdot\mathbf{r}} \tag{2.46}$$

$$\mathbf{u}_\mathbf{k}(\mathbf{r}+\mathbf{a}) = \mathbf{u}_\mathbf{k}(\mathbf{r}) \tag{2.47}$$

where $\mathbf{k}$ is the wavevector, $\mathbf{a}$ is the lattice vector and the time-dependent terms in the equations are dropped for brevity. The function $\mathbf{u}_\mathbf{k}(\mathbf{r})$ is called the Bloch function, and it has the periodicity of the crystal lattice. The eigenfrequencies and eigenvectors of the structure can be calculated by inserting Eq. 2.46 into Eq. 2.29. By applying translation symmetry and solving for a large set of $\mathbf{k}$ values, the band structure with k_i values in the interval $[-\frac{\pi}{a}, \frac{\pi}{a}]$ are obtained. This region is called the first Brillouin zone (FBZ). Detailed information about designing PCs can be found in Ref. [77].

In finite element simulations (COMSOL[4]), by applying periodic boundary conditions and solving Eq. 2.29, we can design a quasi-2D phononic crystal with sufficiently large bandgap, as shown in Fig. 2.11. The crystal we fabricate has a bandgap located between 4 and 6 GHz. If the designed mechanical mode is surrounded by such phononic crystals and its frequency lies within the bandgap, the displacement profile of that mode decays exponentially into the crystals, and thus the phononic crystals serve as acoustic shields.

4. https://www.comsol.com/

CHAPTER 3

CIRCUIT DESIGN

Circuit design plays an important role in a successful experiment. In this chapter, the circuit design for superconducting circuits and mechanical systems is discussed. The qubit used in our experiment is a Gmon qubit, which is a combination of an Xmon qubit with a tunable coupler [97]. A circuit model for the experiment is shown in Fig. 3.1. The C_q, L_q and R_q represent qubit capacitance, qubit SQUID inductors and qubit resistance respectively. The coupler consists of several inductors, including L_g, L_w and L_c. The L_c here is a Josephson junction and its phase ϕ can be controlled by an external drive line (G-line). The maximum coupling strength between a qubit and mechanical resonator is achieved when the coupler junction phase is equal to π, while minimum coupling strength happens when the phase is $\frac{\pi}{2}$ or $\frac{3\pi}{2}$ [97, 102]. The mechanical resonator can be described by the Butterworth-van Dyke model (BVD) model [76, 103]. The R_m, C_m, and L_m represent the lumped-circuit elements for the mechanical resonator. The C_0 and R_e represent the geometric capacitance and the loss of an interdigital transducer. The two L_{fc} and L'_{fc} represent flip-chip inductors, one is on the qubit chip (L_{fc}) and the other is on the mechanical resonator chip (L'_{fc}). Two chips are coupled to each other by L_{fc} and L'_{fc}, with a mutual inductance M. The R'_{fc} represents loss from the flip-chip inductor on the piezoelectric substrate. Due to the piezoelectricity, inductors on the piezo substrates have much larger phonon emissions, and in general, have much higher dissipation than on sapphire or silicon. The typical loss tangent[1] for a piezoelectric substrate is between 100×10^{-6} and 2000×10^{-6}, which is at least two orders of magnitude larger than a sapphire or silicon substrate [104–108]. In our model, the loss of the inductors on the sapphire chip is ignored. In the following sections, we discuss the circuit components step by step and will build the full circuit model (see Fig. 3.1) with control lines at the end of the chapter.

1. The dominant loss of the piezoelectric substrates mostly comes from the acoustic emission, not from the dielectric loss. The use of loss tangent terminology is not well defined for the piezoelectric substrates.

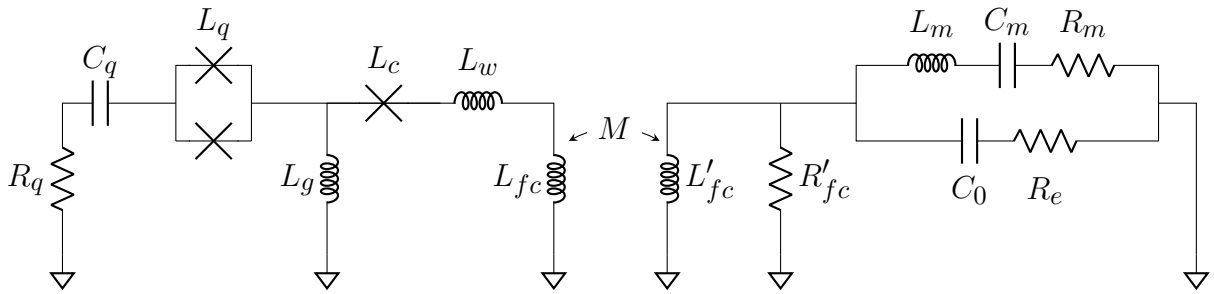

Figure 3.1: Circuit model for a qubit integrated with a BVD resonator. The control lines are dropped for brevity.

3.1 Butterworth-van Dyke (BVD) circuits

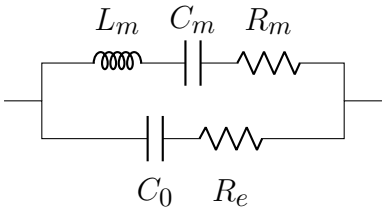

Figure 3.2: The circuit diagram for a BVD resonator.

The Butterworth-van Dyke model is a common lumped element circuit model to describe the electrical response of a piezoelectrical mechanical resonator. This model includes a geometric capacitance C_0 with an electrical loss element R_e, in parallel with a RLC circuit that is for modeling a mechanical system, which consists of a mechanical inductance L_m, a mechanical capacitance C_m and a mechanical loss R_m (see Fig. 3.2). Those lumped elements can be determined by the material properties and the device geometry. In general, the material properties can be obtained from the supplier or COMSOL simulation. If not, more dedicated experiments need to be designed to study the material properties. For the SAW resonator shown in Fig. 3.3, the C_0 is given by the IDT geometric capacitance,

$$C_0 \sim C_t = N_p W \epsilon_\infty \tag{3.1}$$

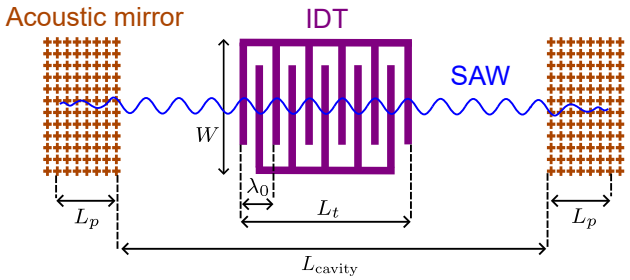

Figure 3.3: The schematic diagram of the SAW resonator. The IDT with finger pairs $N_p = 5$ is shown in this diagram.

The mechanical capacitance C_m is given by [76]

$$\frac{C_m}{C_0} \sim \frac{L_t}{L_{\text{cavity}} + 2L_p} K^2. \tag{3.2}$$

where $L_t = N_p\lambda_0$ is the IDT width and λ_0 is the wavelength of the SAW, L_p is the penetration depth that the SAW can go into the acoustic mirrors, and L_{cavity} is the distance between two acoustic mirrors. If the acoustic mirror is made by PCs, L_p is about a few μm. The mechanical resonant frequency ω_s is related to the SAW speed v, and we assume it is matched with the IDT resonant frequency ω_t. The L_m is then given by

$$\omega_s \sim \omega_t = \frac{2\pi v}{\lambda_0} = \frac{1}{\sqrt{L_m C_m}}. \tag{3.3}$$

For a Lamb wave of S_0 mode on the AlN/Si membranes, v is about 10 km/s. With the equations above, we can know the BVD lumped circuit parameters based on the device dimension and material properties. The resistances R_m and R_e are more related to the defects from fabrication and material growth, and it is hard to distinguish one from the other. The dissipation in the resonator can be extracted by measuring the quality factor of the resonator, as we will discuss below.

Now, we can write down the impedance of the BVD circuit,

$$Z_{BVD} = \left[\frac{1}{1/(j\omega C_0) + R_e} + \frac{1}{1/(j\omega C_m) + j\omega L_m + R_m}\right]^{-1}. \tag{3.4}$$

This circuit has two resonances. One resonance ω_p involves C_0 and the mechanical inductance L_m, which is called the electromechanical resonance (or parallel mode). The other resonance ω_s involves the mechanical elements C_m and L_m, and it is called the mechanical resonance (or series mode). The ω_p and ω_s are given by

$$\omega_s = 2\pi f_s = \sqrt{\frac{1}{L_m C_m}} \tag{3.5}$$

$$\omega_p = 2\pi f_p = \frac{1}{\sqrt{L_m C_m}} \sqrt{1 + \frac{C_m}{C_0}} = \omega_s \sqrt{1 + \frac{C_m}{C_0}} \tag{3.6}$$

The mechanical resonance ω_s is defined when the BVD impedance is zero, while the electromechanical resonance ω_p is defined when the impedance is infinite, as shown in Fig. 3.4. Both resonances can be characterized by two-port transmission measurements. In Fig. 3.5(a),

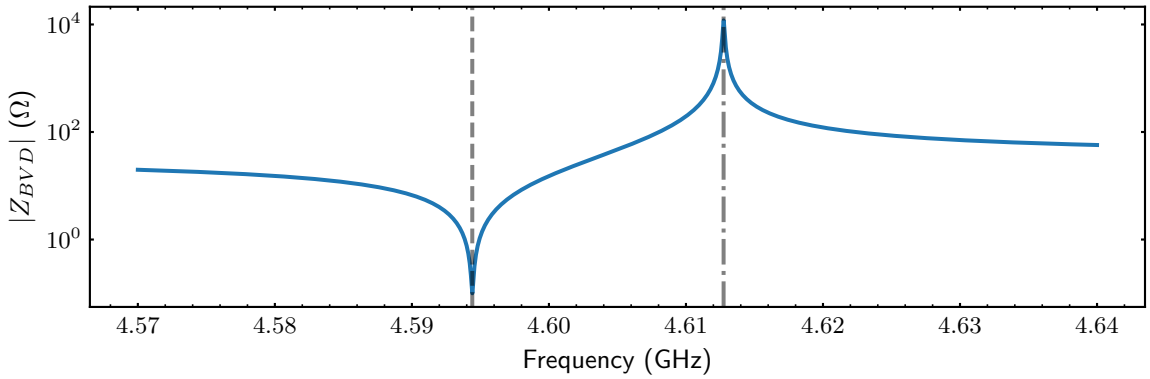

Figure 3.4: The absolute value of an impedance for a BVD circuit. The circuit parameters include $L_m = 0.15\,\mu\text{H}$, $C_m = 8\,\text{fF}$, $C_0 = 1\,\text{pF}$, $R_e = 0\,\Omega$ and $R_m = 0.1\,\Omega$. The dashed and dash-dot lines indicate f_s and f_p respectively.

a "through" configuration is shown and we probe the electromechanical resonance since the transmission dip shows up when the impedance is infinite. In Fig. 3.5(b), on the other hand, the "tee" configuration is displayed and the transmission dip shows up when the impedance is zero, which corresponds to the mechanical mode. As we will show later, the Gmon qubit is coupled to the mechanical mode, which is emphasized in the "tee" configuration.

With the BVD resonator parameters, we can calculate the $1/S_{21}$ and extract the resonator

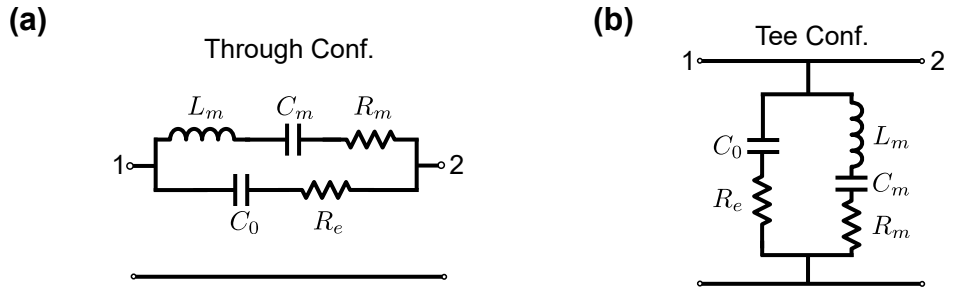

Figure 3.5: The microwave transmission measurement schematic diagram for (a) through configuration and (b) tee configuration. The two ports are labeled by 1 and 2 respectively.

quality factor from a transmission measurement [109]. If R_e is ignored, Z_{BVD} is given by

$$Z_{BVD} = \frac{1 + j\omega R_m C_m - L_m C_m \omega^2}{-R_m C_m C_0 \omega^2 + j(\omega C_m - \omega^3 L_m C_m C_0 + \omega C_0)} \tag{3.7}$$

$$= \frac{1 + j\omega R_m C_m - L_m C_m \omega^2}{\omega(C_0 + C_m)\left[(-R_m \frac{C_0 C_m}{C_0 + C_m}\omega) + j - \frac{L_m C_0 C_m}{C_0 + C_m}\omega^2\right]} \tag{3.8}$$

$$= \frac{1 + j\omega R_m C_m - L_m C_m \omega^2}{j\omega(C_0 + C_m)(1 + j\omega R_m \tilde{C} - L_m \tilde{C}\omega^2)} \tag{3.9}$$

where $\tilde{C} = \frac{C_m C_0}{C_m + C_0}$. For the "through" configuration, we can define

$$\omega = \omega_p(1 + \delta) \tag{3.10}$$

$$Q_i^p = \frac{1}{R_m \tilde{C} \omega_p}. \tag{3.11}$$

If we Taylor expand around the resonance ω_p, and then Z_{BVD} can be approximated as follows

$$Z_{BVD}(\omega \sim \omega_p) \sim \frac{1 + j\omega_p(1+\delta) R_m C_m - L_m C_m \omega_p^2 (1+\delta)^2}{j\omega_p(1+\delta)(C_0 + C_m)\left[1 + j\omega_p(1+\delta) R_m \tilde{C} - L_m \tilde{C}\omega_p^2(1+\delta)^2\right]} \tag{3.12}$$

$$\sim \frac{1 + j\omega_p R_m C_m - L_m C_m \omega_p^2}{j\omega_p(C_0 + C_m)\left[1 + \frac{j(1+\delta)}{Q_i^p} - (1 + 2\delta)\right]} \tag{3.13}$$

$$= -\frac{Q_i^p(1 + j\omega_p R_m C_m - L_m C_m \omega_p^2)}{\omega_p(C_0 + C_m)(1 + j2\delta Q_i^p)}. \tag{3.14}$$

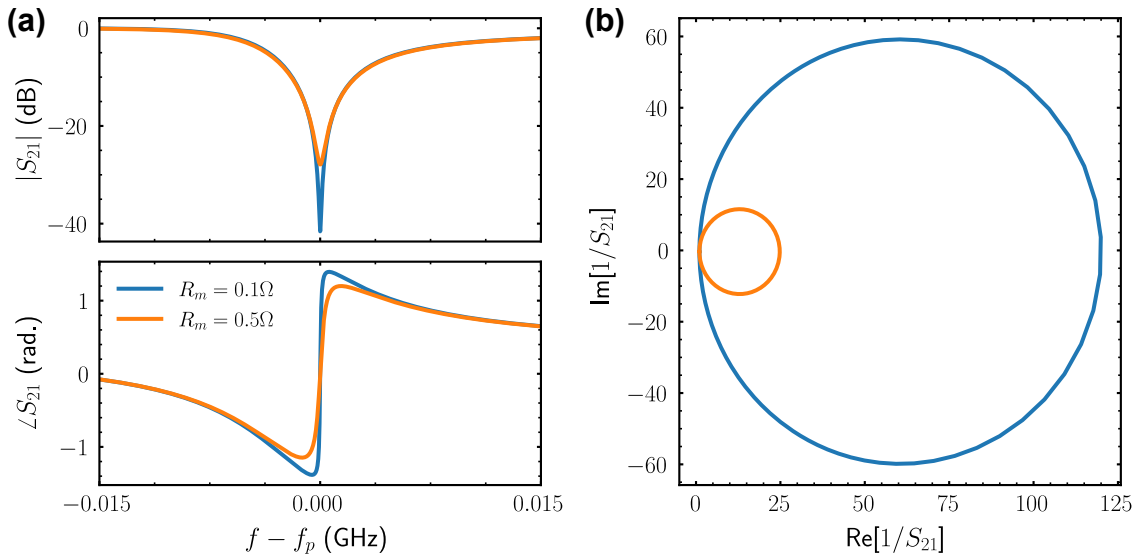

Figure 3.6: Microwave transmission signal with a through configuration. (a) The amplitude (top) and phase (bottom) of the transmission signal. Combining the amplitude and phase information, $1/S_{21}$ is plotted at (b). The diameter of the circle indicates the ratio of Q_i^p/Q_c^p. If the Q_c^p is the same, a larger circle implies that the resonator has a higher internal quality factor.

We can define $Z_l^p = -\frac{1+j\omega_p R_m C_m - L_m C_m \omega_p^2}{\omega_p(C_0+C_m)}$, and the inverse S_{21} is given by

$$Z_{BVD}(\omega \sim \omega_p) = \frac{Q_i^p |Z_l^p| e^{j\varphi}}{1 + 2j\delta Q_i^p} \tag{3.15}$$

$$S_{21}^{-1}(\omega \sim \omega_p) = 1 + \frac{Z_{BVD}(\omega \sim \omega_p)}{2Z_0} = 1 + \frac{Q_i^p e^{j\varphi}}{Q_c^p(1 + 2j\delta Q_i^p)} \tag{3.16}$$

where φ is an arbitrary phase and the Q_c^p is defined as $\frac{2Z_0}{|Z_l^p|}$. The S_{21}^{-1} of a "through" configuration is shown in Fig. 3.6. Similar approaches can be applied to the "tee" configuration, and the results are listed below

$$Z_{BVD}(\omega \sim \omega_s) = \frac{1 + 2j\delta Q_i^s}{Q_i^s \omega_s (C_0 + C_m)(1 + j\omega_s R_m \tilde{C} - L_m \tilde{C} \omega_s^2)} \tag{3.17}$$

$$= \frac{|Z_l^s| e^{j\varphi}(1 + 2j\delta Q_i^s)}{Q_i^s} \tag{3.18}$$

$$S_{21}^{-1}(\omega \sim \omega_s) = 1 + \frac{Z_0}{2Z_{BVD}(\omega \sim \omega_s)} = 1 + \frac{Q_i^s e^{-j\varphi}}{Q_c^s(1 + 2j\delta Q_i^s)} \tag{3.19}$$

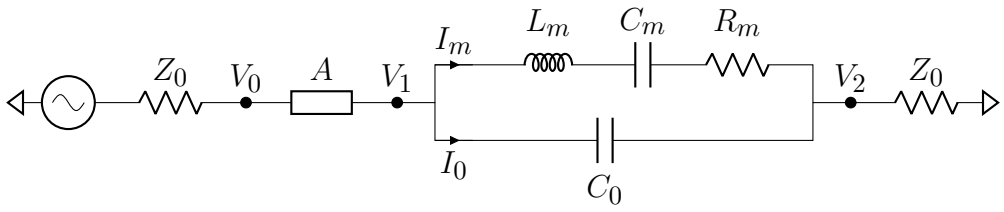

Figure 3.7: The typical circuit diagram for measuring a BVD resonator. The generator usually is a vector network analyzer (VNA). The attenuation comes from the attenuators in the setup and the loss from the microwave cables.

where $Z_l^s = \frac{1}{\omega_s(C_0+C_m)(1+j\omega_s R_m\tilde{C}-L_m\tilde{C}\omega_s^2)}$, $Q_c^s = \frac{2|Z_l^s|}{Z_0}$ and $Q_i^s = \frac{1}{R_m C_m \omega_s}$.

3.2 Estimating the number of phonons in a BVD resonator

A typical setup for probing a BVD resonator is shown in Fig. 3.7. The generator has an impedance $Z_0 = 50\,\Omega$ and an output power of P_0. P_0 is reduced by an attenuator[2] A and is connected to a BVD resonator. In the following, we use the "through" configuration as an example, and show how to estimate the energy stored in the resonator. This estimation could provide useful information to understand the two-level system (TLS) defects in our device.

We first look at the circuit when it resonates at ω_s. The $Z_{BVD}(\omega_s)$ is given by

$$Z_{BVD}(\omega_s) = \left(j\omega_s C_0 + \frac{1}{R_m}\right)^{-1} \tag{3.20}$$

The currents that go through the mechanical elements and geometric capacitance are given

$$I_0 = j\omega_s C_0(V_1 - V_2) \tag{3.21}$$

$$I_m = \frac{V_1 - V_2}{R_m} \tag{3.22}$$

2. The attenuator is expressed in the decibel unit.

The voltage V_2 can be obtained by the voltage divider formula

$$V_2 = \frac{V_1}{1 + Z_{BVD}(\omega_s)/Z_0} \tag{3.23}$$

By inserting V_2 back to Eq. 3.22, we can get

$$I_m = \frac{V_1}{R_m[1 + Z_0/Z_{BVD}(\omega_s)]} \tag{3.24}$$

The voltage V_1 is the sum of the incident ($V_1^+ = \frac{V_0^+}{\sqrt{A}}$) and reflected ($V_1^- = V_0^- \times \sqrt{A}$) voltages. The V_1^- can be expressed as

$$V_1^- = S_{11}V_1^+ = \frac{Z_{BVD}(\omega_s)}{Z_{BVD}(\omega_s) + 2Z_0}V_1^+ \tag{3.25}$$

where S_{11} is the element from scattering parameters [110]. The V_1 is then given by

$$V_1 = V_1^+ + V_1^- \tag{3.26}$$

$$= \frac{2Z_{BVD}(\omega_s) + 2Z_0}{Z_{BVD}(\omega_s) + 2Z_0}\frac{V_0^+}{\sqrt{A}}. \tag{3.27}$$

The total energy E_m^s stored in the mechanical elements can be calculated as follows

$$E_m^s = \frac{L_m|I_m|^2}{2} \tag{3.28}$$

$$= \frac{L_m}{2}\left(\frac{V_1}{R_m}\right)^2 \frac{1}{\left|1 + \frac{Z_0}{Z_{BVD}(\omega_s)}\right|^2} \tag{3.29}$$

$$= 4\frac{L_m}{2}\left(\frac{1}{R_m}\right)^2 \frac{1}{\left|1 + \frac{Z_0}{Z_{BVD}(\omega_s)}\right|^2} \frac{\left|1 + \frac{Z_{BVD}(\omega_s)}{Z_0}\right|^2}{\left|2 + \frac{Z_{BVD}(\omega_s)}{Z_0}\right|^2} \frac{|V_0^+|^2}{A} \tag{3.30}$$

$$= 4\frac{L_m P_0}{R_m^2 Z_0 A}\frac{\left|Z_{BVD}(\omega_s)\right|^2}{\left|2+\frac{Z_{BVD}(\omega_s)}{Z_0}\right|^2} \tag{3.31}$$

where $P_0 = \frac{|V_0^+|^2}{2Z_0}$ is the input power from the generator. The phonon numbers $\langle n_s \rangle$ can be estimated by

$$E_m^s \sim \langle n_s \rangle \hbar\omega_s \tag{3.32}$$

If the resonance is at ω_p, we can use similar approaches to estimate the phonon number. In this case, $V_1 - V_2$ and current I'_m for the electromechanical mode are given by

$$V_1 - V_2 = \frac{V_1}{1 + Z_0/Z_{BVD}(\omega_p)} \tag{3.33}$$

$$I'_m = \frac{V_1 - V_2}{Z_{BVD}(\omega_p)} \tag{3.34}$$

Thus, total energy E_m^p stored in the mechanical elements and its corresponding phonon number is

$$E_m^p = \frac{1}{2}L_m|I'_m|^2 \tag{3.35}$$

$$= \frac{1}{2}L_m\left|\frac{V_1}{Z_{BVD}(\omega_p)+Z_0}\right|^2 \approx \left\langle n_p \right\rangle \hbar\omega_p \tag{3.36}$$

where $\left\langle n_p \right\rangle$ is the phonon numbers when the resonator is at resonance ω_p.

3.3 Qubit coupled to a mechanical resonator

In this section, we will evaluate the interaction between a qubit and a BVD resonator. For simplicity, we ignore all the dissipative elements in both mechanical systems and superconducting circuits, as shown in Fig. 3.8(a). Some typical lumped-element circuit parameters

are listed in Table 3.1[3].

C_q	88.0 fF
L_q	8.0 nH
L_g	0.3 nH
L_c	1.0 nH
L_w	0.25 nH
L_{fc}	0.25 nH
L'_{fc}	0.25 nH
M	225.0 pH
C_0	1.0 pF
C_m	8.0 fF
L_m	0.15 μH

Table 3.1: Typical lumped-element circuit parameters for a qubit and a FBAR resonator.

The circuits can be simplified with the following transformation. First, we replace the mutual inductor with a T-circuit of inductors, and then we combine all the inductive elements in the coupler, using the formulas in Appendix B.1 and B.2. The simplified circuits are shown in Fig. 3.8(b) and (c). Finally, we can define L_1, L_2 and L_3 as:

$$L_1 \equiv \frac{(L_c + L_w + L_{fc} - M)L_g}{L_c + L_w + L_{fc} + L_g} \tag{3.37}$$

$$L_2 \equiv \frac{L_g M}{L_c + L_w + L_{fc} + L_g} \tag{3.38}$$

$$L_3 \equiv \frac{(L_c + L_w + L_{fc} - M)M}{L_c + L_w + L_{fc} + L_g} + L'_{fc} - M \tag{3.39}$$

3. We ignore the loss terms R_q, R_e and R_m for brevity.

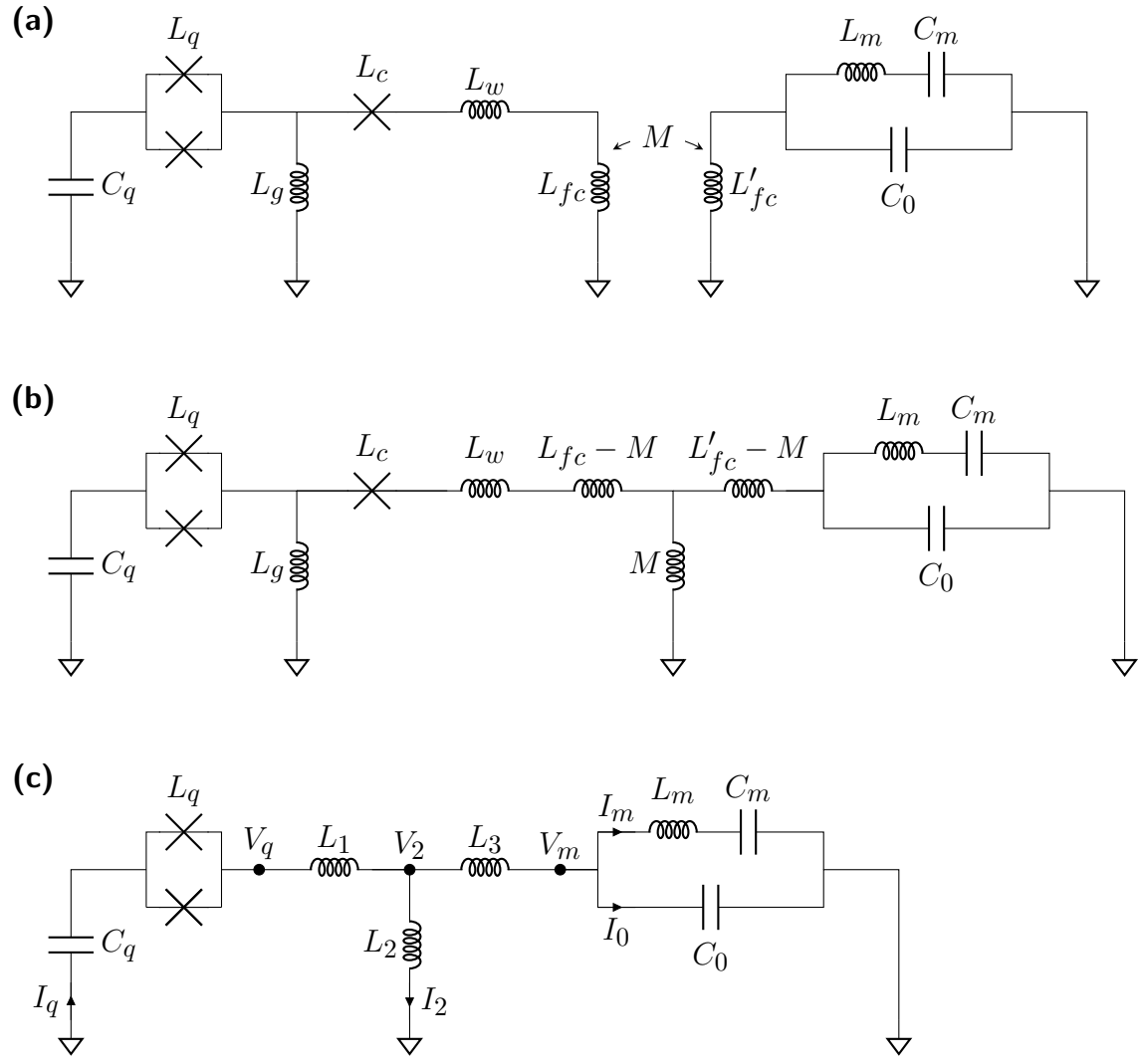

Figure 3.8: Circuit model without dissipative elements. (b) The mutual inductor in (a) is replaced by a T-circuit. (c) The inductors are re-combined by using the circuit transformation in Appendix B.

In Fig. 3.8(c), the voltage V_2 can be derived in three different ways. First, V_2 can be obtained by the following equation:

$$V_2 = j\omega L_2 I_2 = j\omega L_2 (I_q - I_m - I_0) \tag{3.40}$$

$$= j\omega L_2 [I_q - (1 + j\omega C_0 Z_m) I_m] \tag{3.41}$$

where $I_0 = \frac{V_m}{1/(j\omega C_0)} = j\omega C_0 Z_m I_m$ and $Z_m = \frac{1}{j\omega C_m} + j\omega L_m$. Second, the voltage V_2 can be calculated by:

$$V_2 = V_m + j\omega L_3 (I_m + I_0) \tag{3.42}$$

$$= V_m + j\omega L_3 I_m (1 + j\omega C_0 Z_m) \tag{3.43}$$

$$= I_m [Z_m + j\omega L_3 (1 + j\omega C_0 Z_m)] \tag{3.44}$$

Lastly, V_2 can be calculated from the current coming from the qubit

$$V_2 = V_q - j\omega L_1 I_q \tag{3.45}$$

$$= -Z_q I_q - j\omega L_1 I_q \tag{3.46}$$

where $Z_q = \frac{1}{j\omega C_q} + j\omega L_q$. Since Eq. 3.41=Eq. 3.44=Eq. 3.46, two relations are given by

$$[Z_q + j\omega (L_1 + L_2)] I_q - j\omega L_2 (1 + j\omega C_0 Z_m) I_m = 0 \tag{3.47}$$

$$j\omega L_2 I_q - [j\omega (1 + j\omega C_0 Z_m)(L_2 + L_3) + Z_m] I_m = 0 \tag{3.48}$$

Eq. 3.47 and Eq. 3.48 can be combined into eigenvalue equation

$$\begin{pmatrix} Z_q + j\omega (L_1 + L_2) & -j\omega L_2 (1 + j\omega C_0 Z_m) \\ j\omega L_2 & -j\omega (1 + j\omega C_0 Z_m)(L_2 + L_3) - Z_m \end{pmatrix} \begin{pmatrix} I_q \\ I_m \end{pmatrix} = \begin{pmatrix} 0 \\ 0 \end{pmatrix} \tag{3.49}$$

If L_c is tuned to infinite (coupler is "off"), we find $L_2 = 0$, $L_1 \sim L_g$ and $L_3 \sim L'_{fc}$. The off-diagonal terms in Eq. 3.49 become zero and the two systems are decoupled. The qubit then has an eigenfrequency w_q satisfying

$$\frac{1}{j\omega_q C_q} + j\omega_q L_q + j\omega_q L_g = 0 \tag{3.50}$$

and we can solve the equation to get

$$\omega_q = \sqrt{\frac{1}{C_q(L_q + L_g)}} \tag{3.51}$$

The resonator has an eigenfrequency w_r given by

$$j\omega_r(1 + j\omega_r C_0 Z_m)L'_{fc} + Z_m = 0 \tag{3.52}$$

and we replace Z_m with C_m and L_m

$$\omega_r^4 L'_{fc} C_0 L_m C_m - \omega_r^2[L_m C_m + L'_{fc}(C_0 + C_m)] + 1 = 0 \tag{3.53}$$

Eq. 3.53 is exactly the same equation if the BVD circuit is in series with an inductor and we solve for the zeros of that circuit impedance. One of the roots of Eq. 3.53 is close to $\omega_r = \sqrt{\frac{1}{C_m(L_m + L'_{fc})}}$, while the other root is at a much higher frequency. This high-frequency root must be at least a few gigahertz above the qubit frequency to avoid unwanted interaction.

If we look at the coupled system, which means the off-diagonal terms in Eq. 3.49 are not zeros, we can solve Eq. 3.49 numerically. The splitting of two eigenfrequencies can be observed when qubit frequency is tuned across the resonator frequency. The coupling strength $g/2\pi$ is half of the minimum splitting value. As the coupler inductor $|L_c|$ is reduced or the IDT capacitance C_0 is increased, the splitting is enhanced and the coupling strength becomes larger. In Fig. 3.9 and Fig. 3.10, we show the coupling strength $g/2\pi$ for different

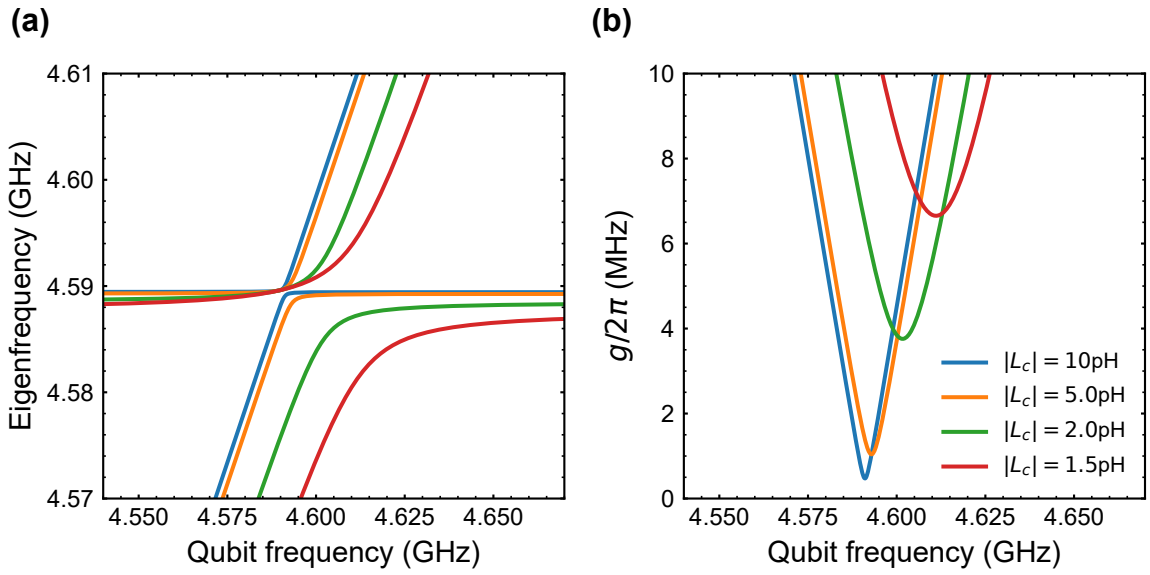

Figure 3.9: Avoided-level crossing and coupling strength for coupling a qubit to a BVD resonator. (a) The splitting for different $|L_c|$ and their corresponding (b) coupling strength.

$|L_c|$ values and different C_0 values, respectively.

3.4 Design of control lines

To fully control our systems, we need several control lines for both the qubit and mechanical resonator. Those control lines must provide reasonable tunability while introducing minimum dissipation to the qubit and the mechanical resonator. In this section, we will use the coupler control line (G-line) as an example, and show how this control line affects the qubit and resonator lifetime. A similar analysis can be applied to other qubit control lines (Z-line and XY-line) and the resonator displacement line (D-line). However, we find that the G-line has more impact on the qubit, especially when a qubit is coupled to a BVD resonator. Both the qubit and resonator are not sensitive to the other control lines.

The G-line is a CPW transmission line with one end shorted to ground and the other end is wire-bonded to a printed circuit board (PCB) trace with $Z_0 = 50\,\Omega$. The G-line is inductively coupled to the tunable coupler junction with a mutual inductance of $M_g \sim 1.5$ pH [73]. In Fig. 3.11(a), we show the circuit of a Gmon qubit and a G-line. By using

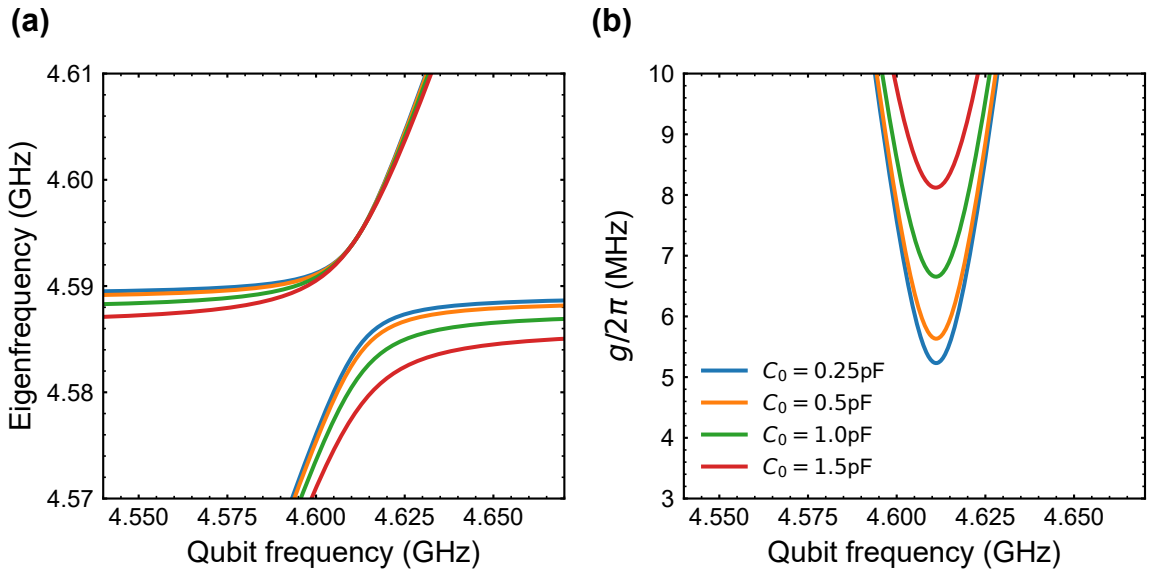

Figure 3.10: Avoided-level crossing and coupling strength for coupling a qubit to a BVD resonator. In this plot, the $|L_c| = 1.5\,\text{nH}$ is used for calculation. (a) The splitting for different C_0 and their corresponding (b) coupling strength.

the formula shown in Appendix B.3, the G-line circuit can be approximated as a series impedance equal to $Z_g = \frac{w_q^2 M_g^2}{Z_0}$, and this term can be absorbed into the rest of the circuit, as shown in Fig. 3.11(b). In this configuration, we only have one dissipative element, which is a $Z_0 = 50\,\Omega$ in the G-line. The circuit can be organized in a way such that the qubit is in series with Z_{eq}, and the qubit lifetime T_q can be estimated by

$$\frac{1}{Z_{eq}} = \frac{1}{j\omega_q(L_c + L_w + L_{fc}) + Z_g} + \frac{1}{j\omega_q L_g} \tag{3.54}$$

$$T_q = \frac{L_q}{Re[Z_{eq}]} = \frac{Q}{\omega_q} \tag{3.55}$$

where Q is the qubit "overall" quality factor. With Eq. 3.55 and the parameters listed in the Table. 3.1, we can numerically calculate T_q. This T_q is limited by the Purcell effect from the G-line (see Fig. 3.12, dashed line). When the coupler is on ($\phi = \pi$), T_q becomes shorter due to the damping from the G-line. However, when a Gmon qubit couples to a BVD resonator[1],

1. The BVD resonator changes the entire circuit, but the impedance of the new circuit and qubit lifetime can be calculated by similar approaches.

as shown in Fig. 3.11 (c), T_q is even shorter when we turn on the coupler. In fact, if C_0 is too large, T_q can be damped to $\sim 10\,\text{ns}$ (see Fig. 3.12). This undesired dissipation can be alleviated if we add a capacitance C_g in parallel with Z_0 in the G-line, as shown in Fig. 3.11 (d). This capacitance serves as a low-pass filter, and can be fabricated together with the SiO_2 crossover (see chapter 4). With a $C_g \sim 10\,\text{pF}$ integrated into the G-line, as shown in Fig. 3.12(b), T_q can eventually be enhanced to $\sim 100\,\mu\text{s}$.

Next, we want to understand whether the G-line has any impact on the mechanical resonator. By using the same strategies, we can rewrite the circuits in Fig. 3.11(c) in a different way, where a BVD resonator is in series with an equivalent impedance Z_{eq}^m. We absorb L_g with Z_q, re-organize most of the inductors, and define Z_1 and Z_2 as

$$\frac{1}{Z_1} = \frac{1}{Z_q} + \frac{1}{j\omega L_g} \tag{3.56}$$

$$Z_2 = Z_1 + j\omega(L_c + L_w + L_{fc} - M) + Z_g \tag{3.57}$$

The Z_{eq}^m then can be expressed as:

$$Z_{eq}^m = \frac{j\omega M Z_2}{j\omega M + Z_2} + j\omega(L'_{fc} - M) \tag{3.58}$$

The mechanical resonator lifetime $T_{1,r}$ can be estimated using the following equation:

$$T_{1,r} = \frac{l_m}{Re[Z_{eq}^m]} \tag{3.59}$$

In Fig. 3.13, we can see that the $T_{1,r}$ is not affected by the G-line, even if C_0 is large or without C_g in the G-line.

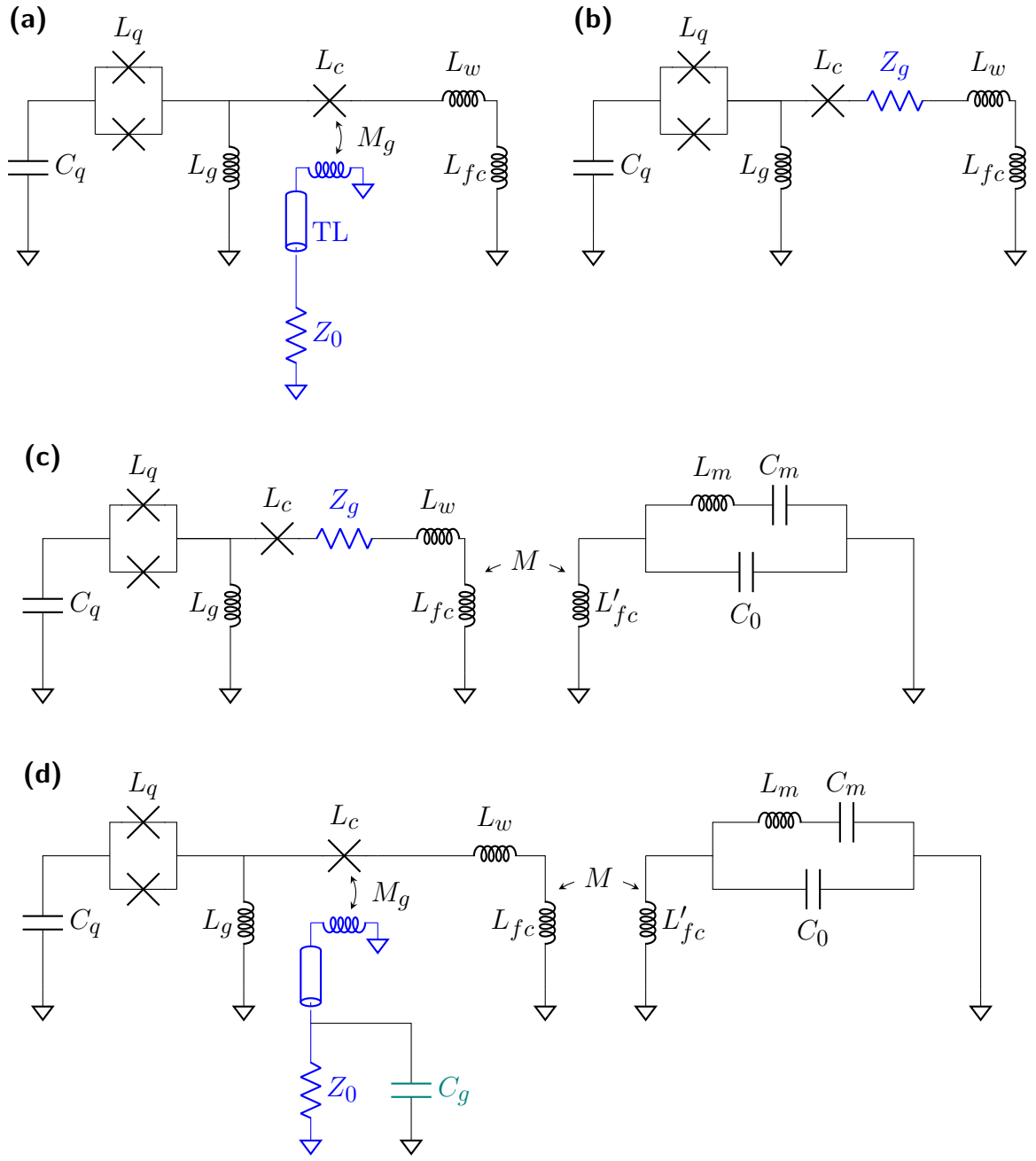

Figure 3.11: (a) The Gmon circuit and the coupler control line (G-line, blue). The G-line consists of a 1 mm lossless CPW transmission line (TL), a $Z_0 = 50\,\Omega$, and a short inductor at one end. (b) Equivalent circuits of (a) can be achieved by using the formula in Appendix. B.3. The G-line circuit is expressed as Z_g (blue). (c) A Gmon qubit with G-line couples to a BVD resonator. The only dissipative element comes from the Z_g. (d) New G-line design, where a capacitance (green) C_g is in parallel with Z_0.

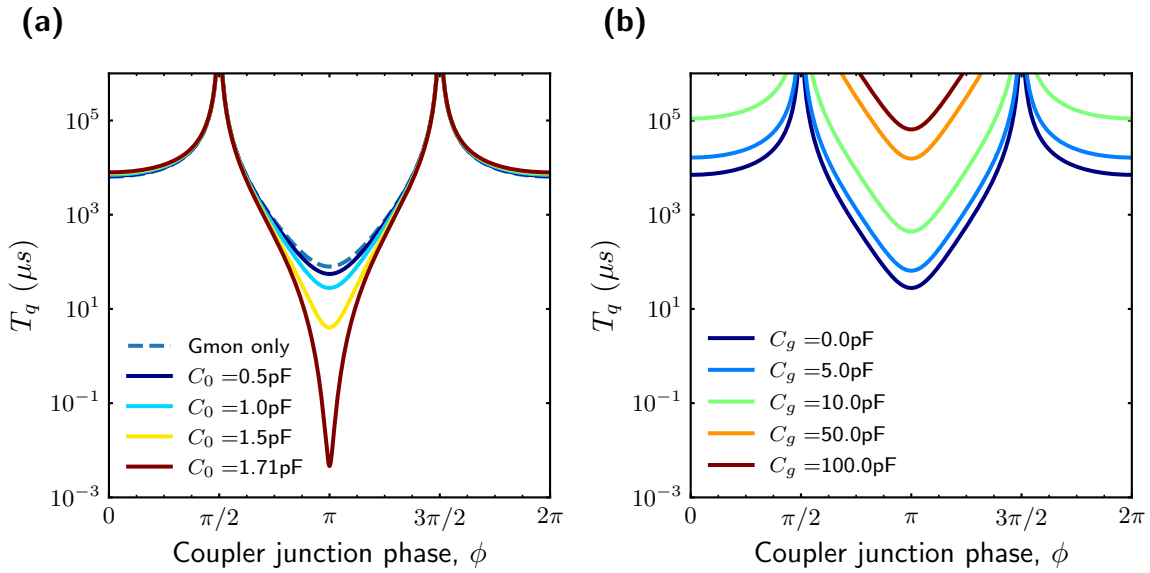

Figure 3.12: The Gmon qubit lifetime T_q versus coupler junction phase. (a) Without a BVD resonator, T_q at different phases is plotted in a dashed line. Solid lines indicate the Gmon circuit coupled to different BVD resonators. (b) By protecting the qubit with the additional capacitor, C_g, T_q is enhanced. In (b), $C_0 = 1\,\mathrm{pF}$ is used for the calculation.

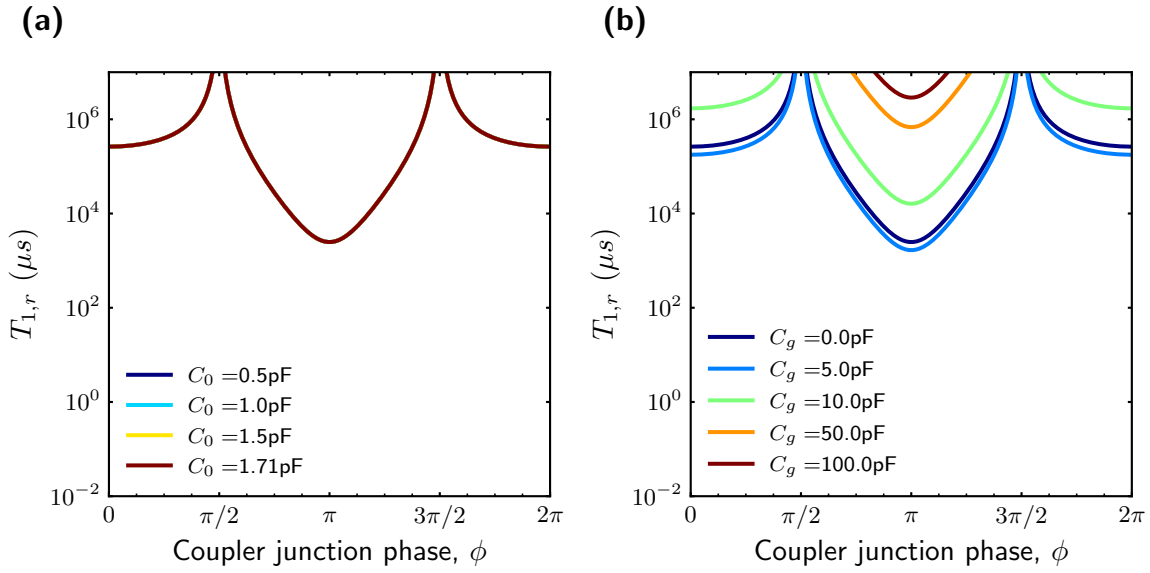

Figure 3.13: Mechanical resonator lifetime at different coupler junction phases. The resonator lifetime $T_{1,r}$ vs (a) C_0 and (b) C_g, respectively.

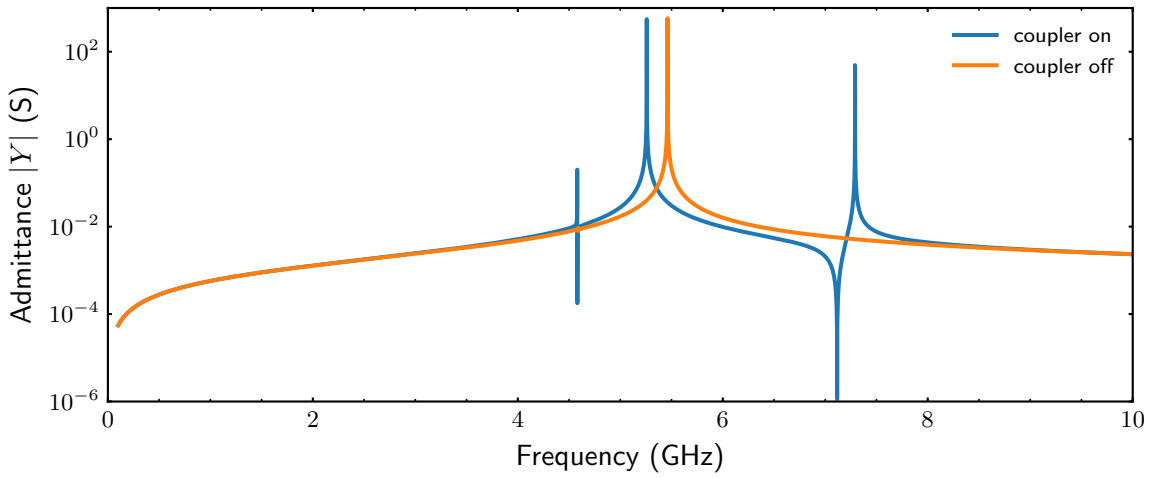

Figure 3.14: The admittance of the entire circuit. Qubit frequency is at $\sim 5.4\,\mathrm{GHz}$ and mechanical resonator frequency is at $\sim 4.6\,\mathrm{GHz}$. The high-frequency resonance can be observed at $\sim 7.2\,\mathrm{GHz}$ when the coupler is on. There are no additional modes that are observed by adding $C_g = 10\,\mathrm{pF}$ in the G-line.

The design rule here is that all the undesired resonances should be a few gigahertz above or below the qubit and mechanical resonance to avoid any unexpected impact on the experiment. In Fig. 3.14, the absolute value of circuit admittance $|Y|$ is plotted. When the coupler is on, the qubit frequency is shifted and we can observe a high-frequency mode. This high-frequency mode is what we expect (see Section 3.1), and we don't find any unexpected resonances even if C_g is introduced. The other constraint here is that all of the control lines should not limit the qubit and mechanical resonator lifetime. There may exist a tradeoff for the circuit design. For example, $g/2\pi$ could be limited due to the IDT capacitance, since the C_0 value would affect how the qubit is damped from the G-line and therefore C_0 cannot be too large. We find that 1 pF is a good value if the qubit is operated at about 4 to 5 GHz. For the other control lines (XY and Z lines), a similar approach can be applied and we find those lines don't limit the qubit and resonator performance.

CHAPTER 4

FABRICATION

In this chapter, we discuss the fabrication process of making superconducting and mechanical devices. Device performance is significantly affected by fabrication, and thus having stable and reliable recipes is very important. All the fabrication in this thesis was performed in the Pritzker Nanofabrication Facility (PNF) at the University of Chicago, except for the aluminum nitride sputter procedure. The AlN film was deposited at the Argonne National Laboratory, using the OEM Group (now acquired by Plasma-Therm, LLC) sputtering system.

4.1 Fabrication process for FBAR devices

4.1.1 Overview

One issue that arises in SAW resonators is that their lifetime is relatively short. For SAW resonators fabricated on lithium niobate ($LiNbO_3$), the main loss channel comes from the phonon scattering from the metal features of IDT and mirrors [80]. One possible solution is to create a suspended structure to avoid bulk scattering. Furthermore, since phononic crystals have been demonstrated to be a low-loss element in the optomechanical resonator [58], we can also integrate this component into our suspended devices, and use PCs as acoustic mirrors. However, PCs are usually made of thin film silicon, and the sacrificial layer below the silicon layer must be removed. These constraints imply that we need a new device design with a new material combination.

For our new design, the device is fabricated on bilayer membranes (AlN on a thin silicon device layer). The acoustic mirrors (PCs) only use the silicon layer, while the IDT is patterned on the bilayer membranes. To avoid mode conversion, we make a roughly $1\,\mu$m long ramp on the AlN layer to smoothly transfer the Lamb wave from the bilayer to the silicon layer. This requires etching the AlN, which introduces the issue of damaging the silicon

layer. To solve this issue, we selectively protect the PC's region by putting a SiO_x stop layer between the AlN and the silicon device layer. The stop layer can be removed by buffer HF (BHF) and thus we can create the ramp on AlN without damaging the PCs. However, due to the limitation of alignment precision, a notch will be created at the bottom of the ramp. The notch causes extra internal reflection and mode conversion, and it should be eliminated if possible. A detailed discussion about the ramp and the notch can be found in Ref. [81]. In the end, the entire device is mechanically released with vapor HF (VHF), so we can have a freely suspended FBAR device. Several important steps of fabricating FBAR devices are shown in Fig. 4.1. The FBAR device and its components are shown in Fig. 4.2. The procedure we describe in this thesis can also be applied to making a quantum transducer [17].

4.1.2 Silicon-on-insulator (SOI) substrate

The wafer we used for the experiment is a commercial silicon-on-insulator (SOI) wafer from Soitec, with a 220 nm device layer ($10\,\Omega/\mathrm{cm}^2$) at (100) crystal orientation, a 2 µm buried oxide layer and a 725 µm thick handle wafer ($1\,\mathrm{k}\Omega/\mathrm{cm}^2$). Silicon-on-insulator wafers are a natural choice for our experiment since we can easily fabricate nano-scale suspended structures by undercutting the buried oxide layer. Because the fabrication process for SOI wafers is mature in both industry and academic research groups, we can easily adapt their approaches to making our own devices. The SOI wafer we bought from Soitec is an 8-inch wafer, and we dice it into several 1.6"×1.6" chips to fit the AlN sputtered tool adaptor.

4.1.3 Alignment markers for optical lithography

For aligning each pattern under the different lithography steps, alignment markers are necessary. The markers we make in this step are used as the coordinate reference for all the optical lithography procedures. We pattern the markers on the diced SOI chip from the

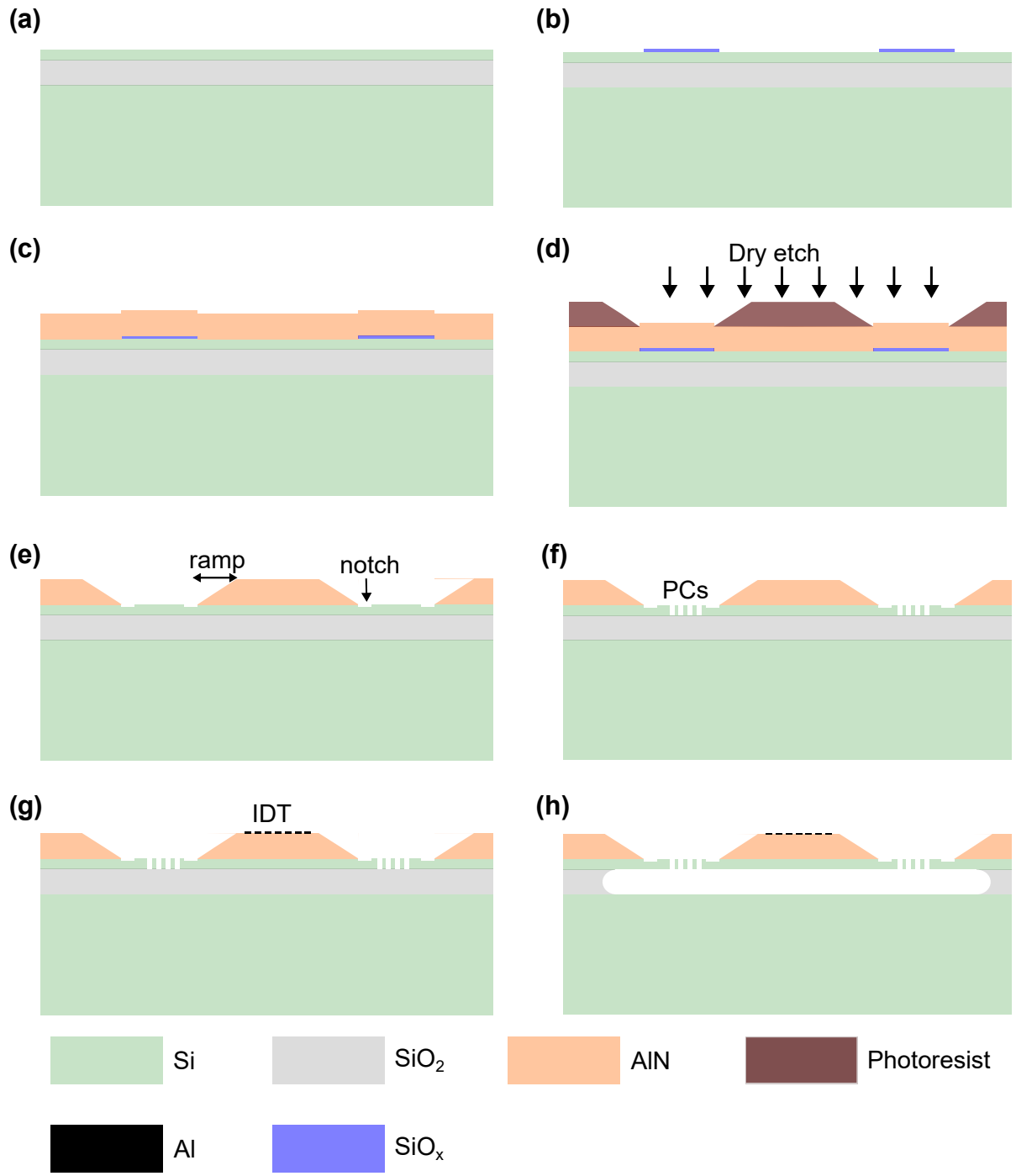

Figure 4.1: Overview of the FABR fabrication procedure. All the diagrams (false scale) display the side view of the FBAR device. (a) The process starts with the SOI wafer. (b) Pattern 70 nm silicon oxide (SiO_x) stop layer. (c) Sputter 330 nm AlN on the wafer. (d) Make the etch mask with reflowed photoresist. (e) Etch AlN and remove the stop layer. The ramp and notch are created in this step. (f) Pattern phononic crystals with electron beam lithography. (g) Pattern 30 nm aluminum interdigital transducer with liftoff process. (h) Mechanically release the device with vapor HF.

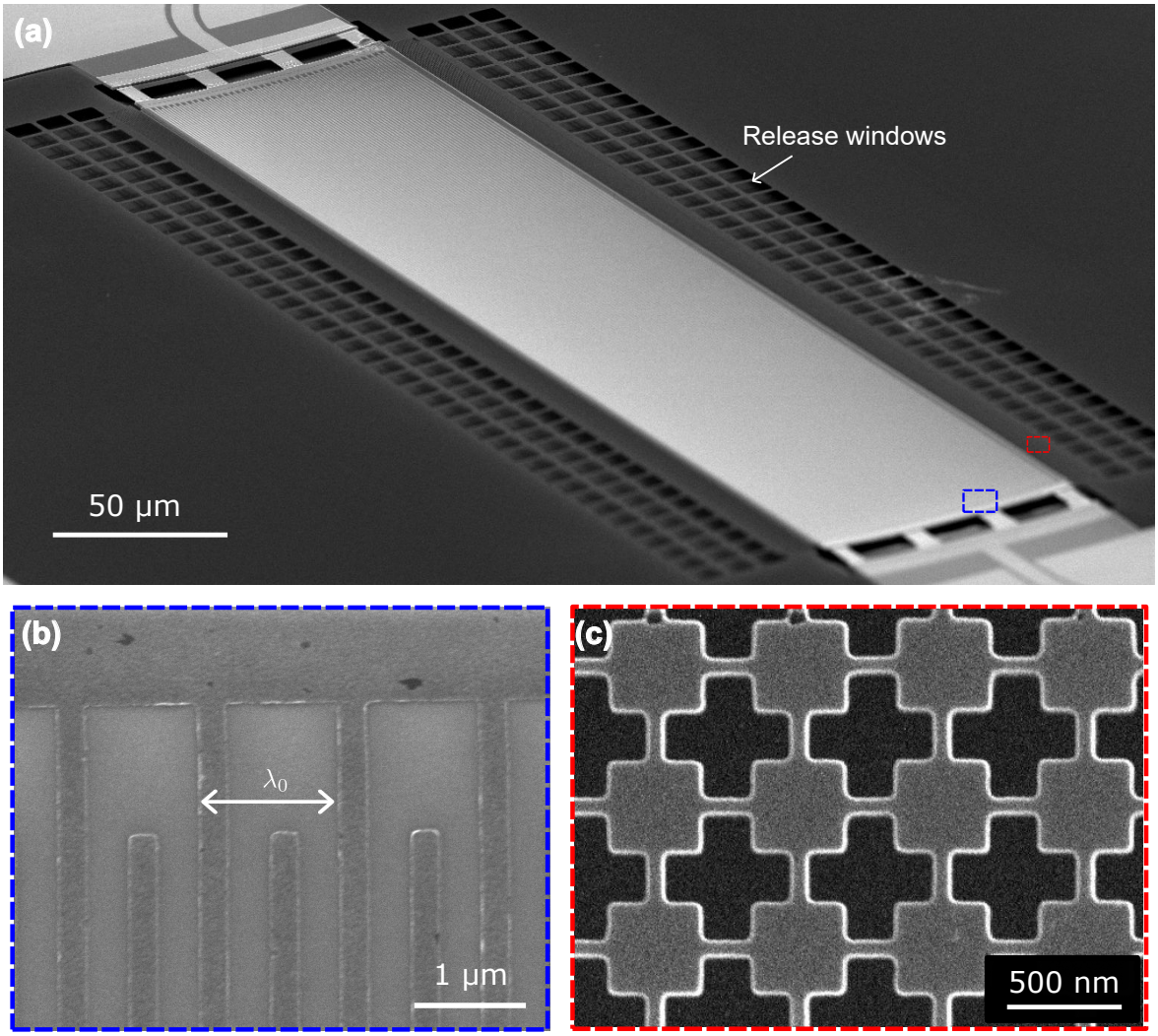

Figure 4.2: The FBAR device consists of a transducer on a piezoelectric bilayer membrane and acoustic Bragg mirrors made of phononic crystals. (a) An angled SEM image of a FBAR device. The transducer (blue) is shown in (b), and the phononic crystals (red) are shown in (c). The wavelength λ_0 of a SAW is defined by the electrode spacing.

previous step with optical lithography, then dry etch it and transfer the marker pattern[1] into the silicon device layer. After fabricating the markers, the chip is cleaned by Nanostip[2] and buffer HF (BHF) before further processing.

4.1.4 Silicon oxide stop layer

To make a high-quality mechanical resonator, keeping the surface of the active device area smooth is crucial. To protect the device layer from subsequent etching steps, we first deposit a 70 nm thick SiO_x stop layer on SOI by using the plasma-enhanced chemical vapor deposit (PECVD) tool in the PNF. The typical SiO_x layer has compressive stress below 100 MPa. The low-stress film is essential to avoid adhesion problems when sputtering AlN on top of it. We then pattern the SiO_x with optical lithography, wet etch the SiO_x by BHF and strip the photoresist by N-methyl-2-pyrrolidone (NMP). After pattering the stop layer, we clean the chip with Nanostrip before AlN deposition. The details of process flow and recipes can be found in Appendix A.1.

4.1.5 Aluminum nitride deposition

After completing the stop layer, the piezoelectric layer of aluminum nitride is sputtered on the entire SOI wafer. Considerations for this process involve film stress, surface roughness, uniformity, and crystal orientation. First, since we are making the suspended device, the AlN film stress must be slightly tensile to avoid collapse or bulking. The ideal value of film stress is about 50 to 250 MPa, and the film thickness is ~ 330 nm. Second, to have a strong piezoelectric response, AlN crystal orientation must be aligned properly. Characterizing the sputtered AlN crystal orientation is performed by X-ray diffraction, and measuring the rocking curve, with a goal of full width at half maximum (FWHM) less than 3°. Finally, the AlN surface should be as smooth as possible, to minimize the bulk scattering and propagation

1. The marker is a cross with a length 200 μm and width 4 μm.

2. Nanostip is a mixture of sulfuric acid with hydrogen peroxide compounds.

loss. The typical root-mean-square (RMS) roughness of sputtered films is less than 3 nm, and the variation of film thickness across the entire wafer should be less than 15 nm. All of the requirements can be realized by OEM Group Endeavor sputtering system installed at the Argonne National Laboratory. In this thesis, all of the AlN films are sputtered by that tool.

The OEM sputtering system consists of two circular aluminum cathodes, and a mixture of the argon and nitrogen gas is flowed into the chamber and can react with aluminum targets, thus forming aluminum nitride on the wafer [111]. The AlN grains are aligned with wurtzite crystal c-axis oriented out of the plane, while the grains have a random in-plane orientation. The controlled parameters of this tool include cathode power, Ar/N_2 flow, substrate heat (via external heater), and an adjustment resistor box (known as a film stress adjustable unit, SAU). There is a complicated tradeoff between parameters and the desired film properties can be achieved by choosing the parameters wisely. AlN film properties can be characterized by several measurements. For example, the AlN crystalline orientation (see Fig. 4.3) can be measured at the Center for Nanoscale Materials (CNM) at Argonne National Laboratory, using the Brucker D8 X-ray diffraction tool. The film stress can be extracted by comparing the wafer curvature before and after AlN deposition, using a profilometer (see Fig. 4.4). The AlN film roughness is measured by atomic force microscopy (AFM) and the uniformity of 500 nm AlN on a silicon substrate is measured by an ellipsometer (shown in Fig. 4.5). The standard AlN deposition procedure can be found in Appendix A.2.

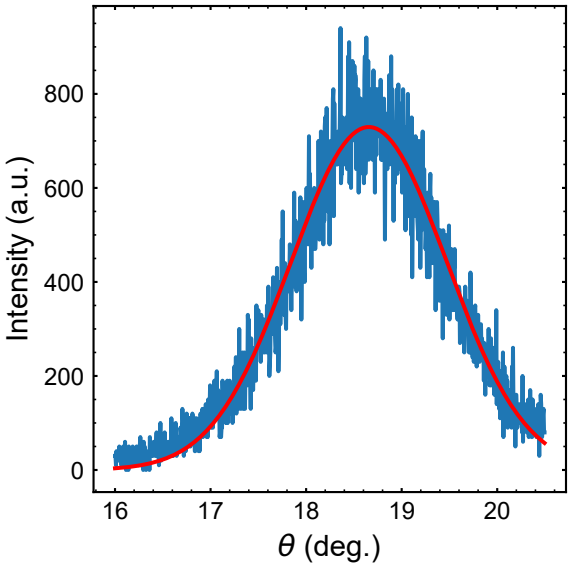

Figure 4.3: AlN sample [002] rocking curve. The blue dots are experimental data and the red line is the fit of a Gaussian curve. The FWHM of the fit curve is $\approx 1.92^{\circ}$

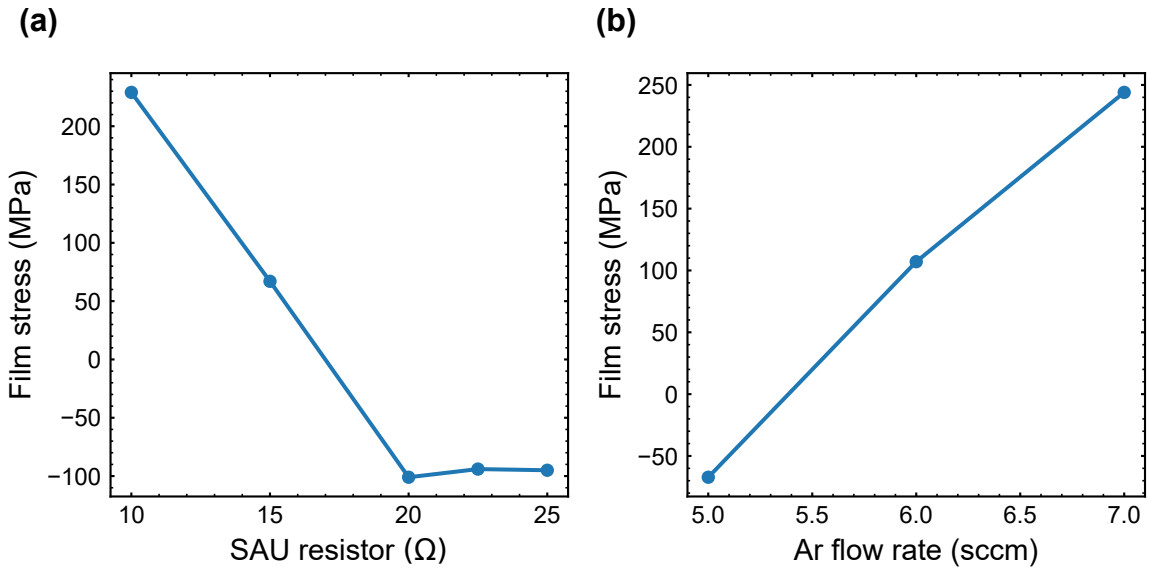

Figure 4.4: The AlN film stress tunability. A positive value of film stress represents a tensile membrane while a negative value represents a compressive membrane. AlN film stress can be controlled either by (a) the SAU resistor, or by (b) the Ar flow rate. However, the film uniformity decreases if the Ar flow rate is enhanced. In (b), the N_2 flow rate is kept at 17 sccm.

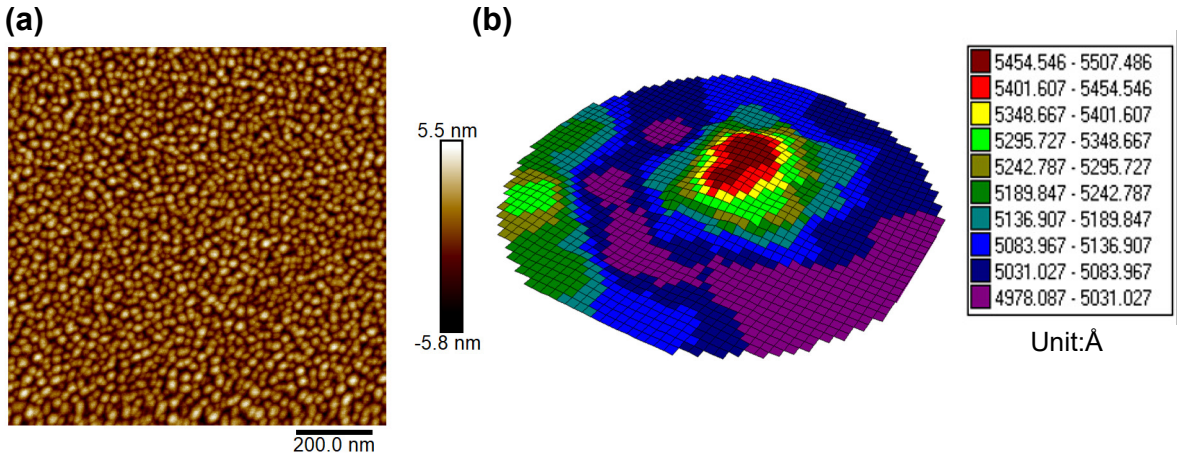

Figure 4.5: AlN film characterization. (a) AFM image of AlN grain. The RMS roughness R_q ≈1.7 nm. (b) The reconstructed profile of the AlN layer by using an ellipsometer. The measurement data is uniformly taken across a 4-inch wafer.

4.1.6 Gold and chromium markers for electron beam lithography

We use 50 nm gold on top of a 10 nm chromium (Cr) adhesion layer as our markers for electron-beam lithography. The markers are made by a liftoff process at 80°C in NMP. Detailed information on this step can be found in Appendix A.3.

4.1.7 Aluminum nitride etch

Next, we need to remove AlN and clear an area for patterning silicon phononic crystals. The AlN film is reactive-ion etched (RIE) using a reflowed photoresist mask. The reflowed mask is made by heating the AZ1512 photoresist layer after optical lithography and development. The following etching process creates a ramp with length $l_{\text{ramp}} \approx 600$ nm on the AlN layer, which helps the surface acoustic wave propagate smoothly from the bilayer (AlN/Si) membrane to the device layer (Si). Since there is a limitation of alignment precision, a notch (depth $t_{\text{notch}} \approx 60$ nm, length $l_{\text{notch}} \approx 200$ nm) is also created during this step [81] (see Fig. 4.6). After etching the AlN, the photoresist is stripped by NMP, and the SiO_x stop layer is cleaned by BHF dip. Further details of this process flow and recipes are listed in Appendix A.4.

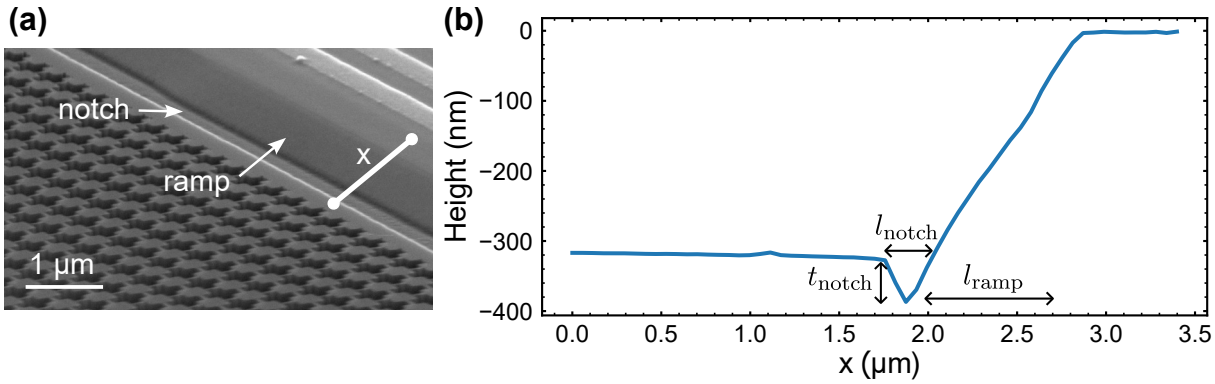

Figure 4.6: (a) An angled SEM image of a ramp and notch. (b) One dimension profile scan along x in (a) by an AFM.

4.1.8 Silicon oxide protective layer

To avoid damage to the AlN from 25% Tetramethylammonium hydroxide (TMAH) electron beam (e-beam) resist developer used in the following process, we deposit a $\sim 5\,\text{nm}$ SiO_x protective layer using atomic layer deposition (ALD). The ALD system can alternately expose samples to tris(dimethylamino)silane (TDMAS) vapor and oxygen plasma. Each cycle deposits approximately $\sim 0.1\,\text{nm}$ SiO_x on sample surfaces. This SiO_x also serves as an adhesion layer for hydrogen silsesquioxane (H-SiQ) electron-beam resist, which is used as an etching mask for making phononic crystals [79]. The important parameters for growing SiO_x using ALD can be found in Table 4.1. In addition to the ALD system, an alternate choice for growing SiO_x is the PECVD tool used in Appendix A.1, however, we find the that ALD tool is more reliable for growing ultra-thin films.

Plasma power	300 W
Precursors	TDMAS
O_2 flow	50 sccm (5 seconds, in one cycle)
Ar flow	100 sccm (5 seconds, in one cycle)
Temperature	250 °C
Number of cycles	45
Turbo	off

Table 4.1: ALD SiO_x growth recipe.

4.1.9 Pattern phononic crystals

Phononic crystals are patterned with e-beam lithography. We first spin coat negative e-beam resist 6% H-SiQ to 110 nm, then bake the sample on 90 °C for 4 minutes and immediately align and mount the sample in the Raith direct-write electron-beam lithography system. After exposure, the H-SiQ is developed by 25% TMAH. To solidify H-SiQ, we post-bake H-SiQ at 300 °C for 15 minutes. This hard bake is an important step to avoid H-SiQ disintegration in the subsequent etching process. After the e-beam lithography, a photoresist layer is patterned to cover most of the sample, except for the area of phononic crystals. The H-SiQ patterns then are transferred into the silicon device layer by using a Cl_2/O_2 inductively coupled plasma (ICP) RIE etch. After etching, the photoresist is stripped by NMP, and the ALD SiO_x and H-SiQ are removed by BHF dip. This BHF clean is critical for removing the H-SiQ as the vapor HF process used during release is insufficient and leaves residues as shown in Fig. 4.7. Detailed information about phononic crystals fabrication can be found in Appendix A.5.

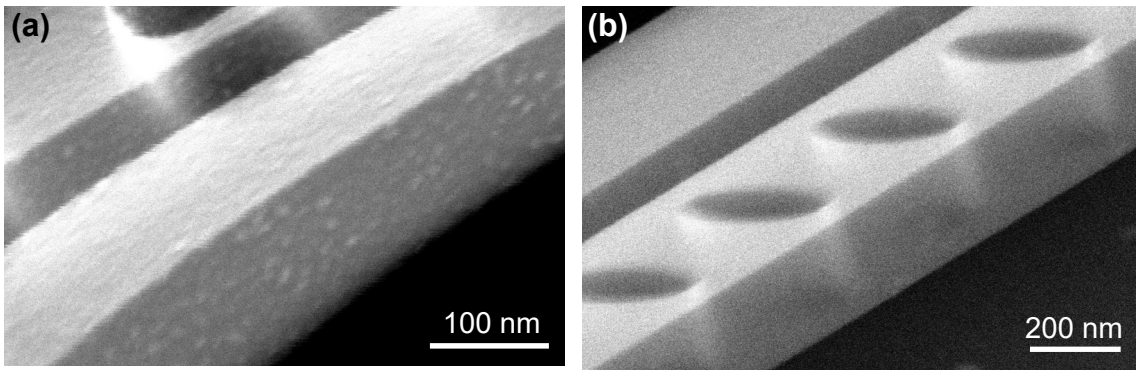

Figure 4.7: (a) An SEM image of H-SiQ residue on the surface of the device when the BHF cleaning dip is not performed. (b) The H-SiQ residue can be removed if BHF cleaning dip is involved.

4.1.10 Pattern interdigital transducer

The IDT is fabricated by using e-beam lithography with a liftoff process. The sample is spin-coated with a Poly(methyl methacrylate) (PMMA) bilayer. To avoid accumulating charges during the e-beam lithography, we deposit a 10 nm thermal gold conduction layer on the top of the PMMA bilayer (see Appendix A.8.7). The sample is then written with an electron beam and developed by methyl isobutyl ketone (MIBK) and isopropanol (IPA) mixture. After exposure, this bilayer profile consists of a thin layer on top of a thick undercut layer, providing a good structure for the liftoff process. Next, 30 nm of aluminum is deposited by using an e-beam evaporator, and then the sample is suspended face-down in acetone for 12 hours. We use very gentle sonication after liftoff if there is any obvious metal stuck on the sample surface. Finally, downstream oxygen cleaning is applied to remove PMMA residue. Further details of this process flow and recipes are listed in Appendix A.6.

4.1.11 Pattern releasing windows

To release our device, we need to drill several open windows through the Si device layer so vapor HF can go below the silicon device layer and etch the buried SiO_2. We use optical lithography to define these windows, and a Cl_2/O_2 dry etch is used for transferring the pat-

terns. The photoresist is stripped by NMP and the sample is cleaned by gentle downstream oxygen to remove any photoresist residue. The multi-device fabrication chip is then diced into smaller chips before going to the mechanical releasing process. Further details of this process flow are listed in Appendix A.7.

4.1.12 Mechanically release devices with vapor HF

Hydrogen fluoride reacts with silicon dioxide according to

$$SiO_2 + 4HF \rightarrow SiF_4 + 2H_2O \tag{4.1}$$

and thus it can be used to undercut the buried oxide layer in the SOI wafer. Since the vapor HF doesn't etch aluminum or AlN, this process is an ideal choice for us to undercut the buried oxide for the FBAR device. However, several things need to be considered when using the vapor HF tool. First, if the H-SiQ is not removed by the BHF cleaning dip completely[3], it can contaminate the device and lower the device quality. This is extremely bad for the optomechanical device since the light will be scattered due to the rough surface and thus lower the quality factor of the optical mode [112]. However, it is not clear whether the H-SiQ residue affects phononic devices in the same way. Second, any liquids present during or once release will cause collapse due to surface tension as it evaporates, so the HF vapor and water vapor ratio must be controlled properly to avoid condensation. In general, increasing the water vapor flow rate or chamber pressure enhances the etching rate, but the device would be more likely to collapse. The recipe is carefully tuned up by increasing the water vapor ratio until the mixture starts to damage devices. Lastly, vapor HF can diffuse through AlN grain boundaries or AlN/Si interface, and create released pockets underneath [79]. An example of this effect is shown in Fig. 4.8. The mechanism behind this phenomenon is not

3. Photoresist residue can also cause contamination in the chamber. It is very important to clean the photoresist on both sides of the chip.

well-understood, but this issue can be prevented by operating the etcher in pulse mode[4], where etching happens for about 5 minutes (see Table 4.2) and then the mixture is purged by N_2 (see Table 4.3). Each cycle creates a tiny undercut, and a targeted undercut can be reached by adding enough cycles (see Fig. 4.9). The typical process time for releasing the FBAR device is about 21 hours (210 cycles). The recipes for performing the etch in pulse mode are provided below.

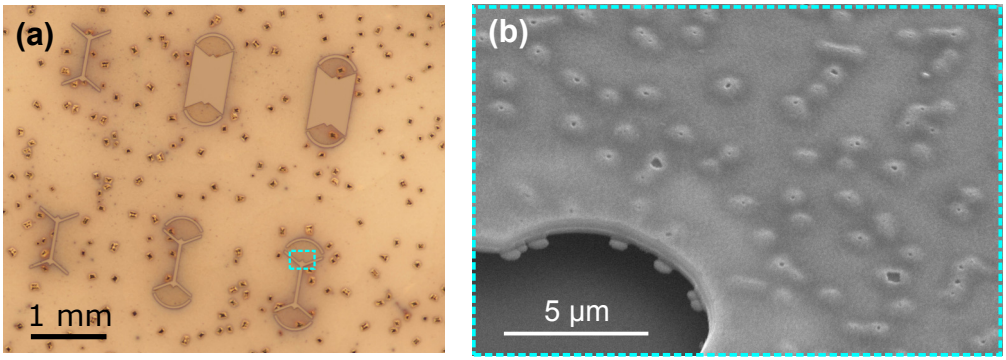

Figure 4.8: Pockmarks in the bilayer membrane due to HF vapor diffusion during mechanical release. (a) Optical microscope image showing pockmarks and (b) SEM image of the cyan marked region

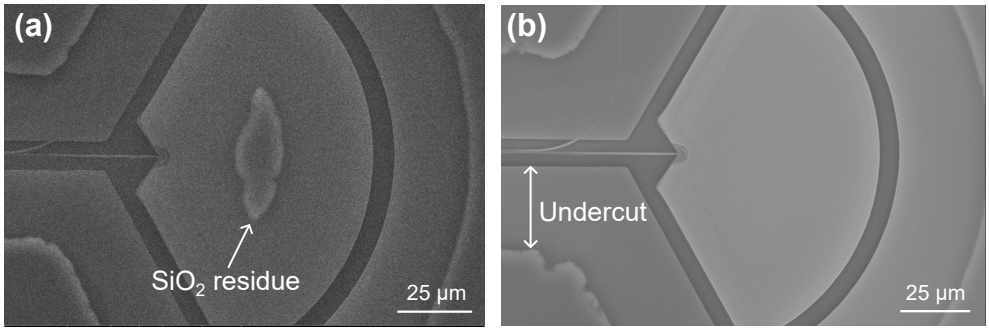

Figure 4.9: Vapor HF undercuts of the buried oxide layer of a test device. Due to the charge accumulation on the buried oxide layer, an SEM can be used to inspect the device suspension. (a) A partially suspended device with the SiO_2 residue at its center. (b) A fully released device with a $\sim 50\,\mu$m undercut.

4. When vapor HF etches the oxide layer, it can generate high temperatures in the sample due to uninterrupted etching, and the heat may damage the sample and create the pockets. When the tool is operated in pulse mode, this issue can be avoided. However, if the AlN is damaged by the previous steps, or is sputtered improperly and forms a porous film, this technique cannot solve the diffusion problem.

Process pressure	21 Torr
H_2O flow rate	5 mg/min
HF flow rate	40 sccm
N_2 flow rate	20 sccm
Etching time	5 minutes

Table 4.2: Vapor HF etching process for one cycle.

Process pressure	21 Torr
H_2O flow rate	0 mg/min
HF flow rate	0 sccm
N_2 flow rate	20 sccm
Purge time	1 minute

Table 4.3: Vapor HF purge process for one cycle.

4.2 Superconducting circuits fabrication

In this section, the fabrication process for superconducting circuits will be described. We will particularly focus on fabricating a Gmon qubit [97]. The recipes and the details of the qubit development procedure are taken from Ref. [73, 74, 80, 113]. A typical qubit chip and its critical components are shown in Fig. 4.10

The fabrication starts from depositing a 100 nm aluminum base layer on a bare sapphire wafer (double-side polished). The base layer is patterned by using a maskless aligner MLA150 from Heidelberg instruments with an optical lithography process. The base layer is etched by $Cl_2/BCl_3/Ar$, and the photoresist is stripped by NMP. Next, we pattern and develop SiO_2 crossover by an optical lithography and liftoff process. Crossovers on the ground plane minimize slot modes on the chips. The thickness of this SiO_2 crossover is about 200 nm. The top aluminum layer of the crossover will be deposited together with the bandage

aluminum layer, which involves an Ar ion mill to remove native oxide on the base layer. Before fabricating Josephson junctions, we need alignment markers for e-beam lithography so the junctions can be aligned properly with the base layer. Here, Ti/Au markers are patterned by optical lithography and deposited by using an e-beam evaporator. The junctions are fabricated with the Dolan bridge technique [114], where the angle depositions are performed in a Plassys e-beam evaporator. Our qubit is a Gmon qubit [97], and the size of the SQUID junction is about 200×200 nm^2. Our coupler junction is larger than the SQUID junction, and its size is about 400×2000 nm^2. After angle deposition, junctions are developed by a liftoff process. To create galvanic contact between the junction layer and the base layer electrodes, we use the bandaging process. This process is designed to avoid damage to the aluminum base layer and substrate below the junction layer, which is a source of qubit decoherence [115]. The last step is making the spacer for flip-chip integration [116]. Our spacer is made by SU8 photoresist (SU8 3005) and its thickness is approximately 5 µm. The spacer cannot be patterned on the FBAR chip since the vapor HF procedure is involved, and any photoresist is not compatible with the vapor HF tool. Besides, SU8 residue is very hard to be removed, and the residue can increase the surface roughness and thus create a loss channel for mechanical devices. As a result, we put the SU8 spacer on the qubit chip instead. To avoid the adhesion issue of SU8 on the aluminum layer, a longer soft-bake and post-bake are necessary (95 °C for 4 minutes). The details of the SU8 development recipe can be found in Section A.8.9. The summary of the qubit fabrication procedure is listed below.

1. Solvent clean sapphire wafer following Section A.8.1, and then deposit 100 nm Al base layer on sapphire using an e-beam evaporator.

2. Pattern SiO_2 crossover by optical lithography and liftoff process.

3. Deposit gold makers by optical lithography and liftoff process.

4. Dice the 4-inch wafer into quarter wafers.

5. Fabricate junctions by using the Dolan bridge technique. The junctions are deposited in a Plassys e-beam evaporator with two different shooting angles.

6. Fabricate the bandage layer with an optical lithography and liftoff process. The Ar ion-milling and top aluminum layer deposition can be realized by using a Plassys e-beam evaporator.

7. Pattern the SU8 spacer following Section A.8.9.

8. Measure the resistance of test junctions.

9. Dice the quarter wafer and pick up the qubit chip with desired parameters for the experiment.

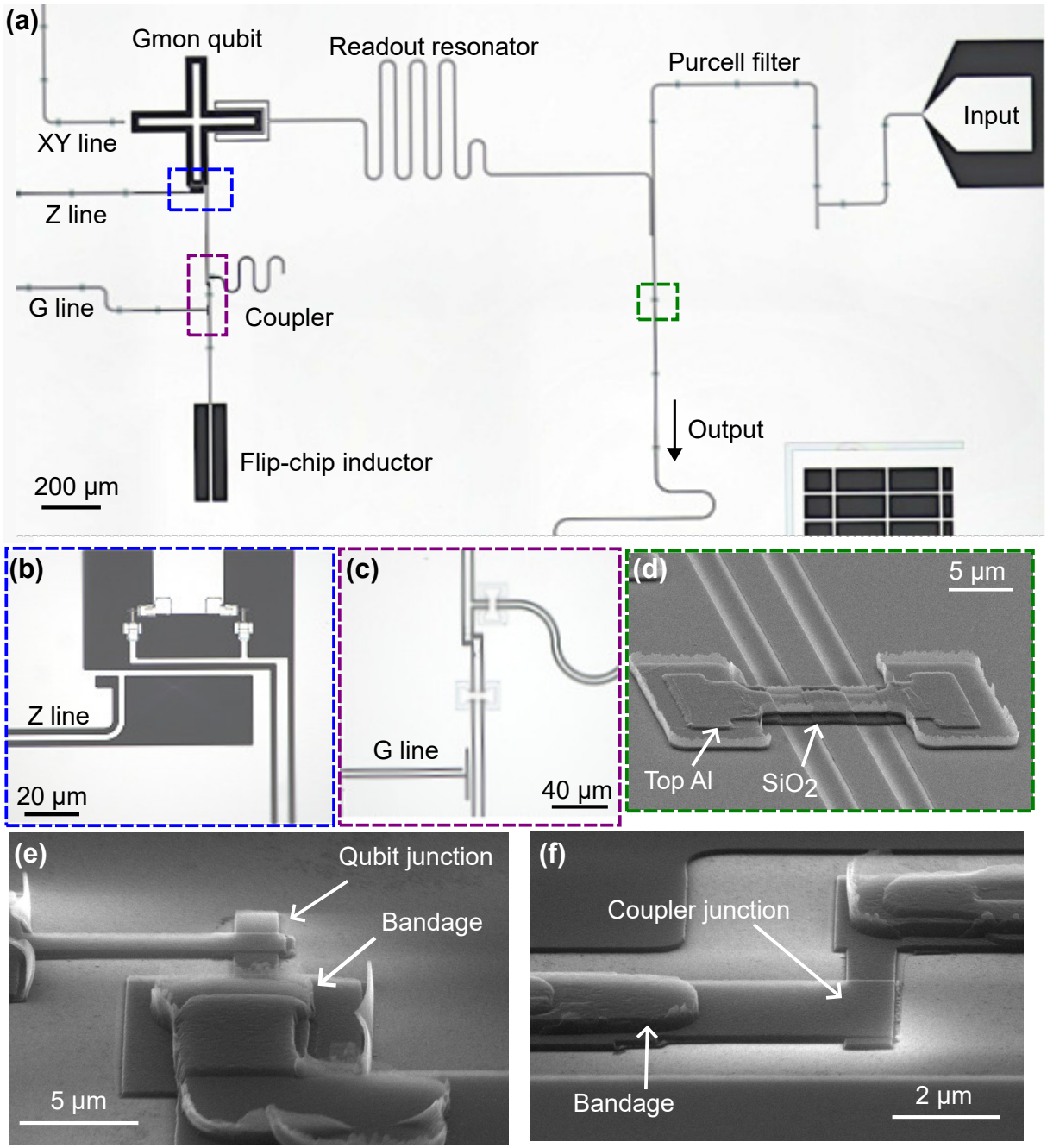

Figure 4.10: Overview of a typical qubit chip. (a) Optical microscopy image of a Gmon qubit, control lines, readout resonator, Purcell filter, and flip-chip inductor. The close view of qubit SQUID (blue), coupler (purple) and SiO_2 crossover (green) are shown in (b), (c), (d) respectively. Angled SEM images of the (e) qubit junction, and (f) the coupler junction with its bandage layer.

4.3 Flip-chip integration

The flip-chip technique is used to integrate different incompatible substrates. The traditional method is using indium bonds [117] to create galvanic contact between two substrates, however, this process is complicated and the integrated chips cannot be reused once they are assembled. Here, following Ref. [116], we integrate two different substrates by aligning the two chips under a mask aligner and then using glue (nLof photoresist) to bond the two chips. The assembled device is shown in Fig. 4.11. Typical misalignment (shown in Fig. 4.12) in the lateral direction is about 3 µm, and the rotation misalignment is less than 1 mrad. This process is relatively simple, and more importantly, the two chips can be recycled since we can use acetone to dissolve the glue and separate the chips. However, when disassembling the integrated device, the FBAR chip must be transferred to IPA and then use a critical point dryer (CPD) to remove the liquid. Critical point drying avoids surface tension forces during evaporation by going from liquid to gas around the critical point, avoiding phase transitions. In the critical point dryer, IPA is first replaced by liquid CO_2 ($\sim 6\,^{\circ}$C, 850 PSI). The chamber is then heated under pressure until CO_2 passes the critical point ($\sim 31\,^{\circ}$C, 1100 PSI). Then, the high-pressure chamber is vented slowly and the FBAR device can be dried without suffering from surface tension. The phase diagram of the CO_2 [118] is shown in Fig. 4.13.

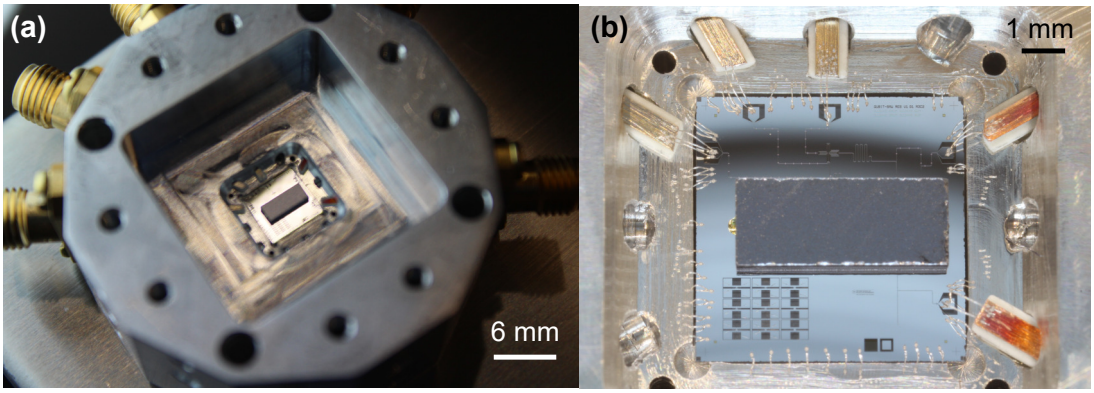

Figure 4.11: Photograph of an assembled device. (a) The assembled chips sit in an aluminum qubit box. (b) A closer look at integrated chips. The top chip is a 4×2 mm^2 FBAR chip and the bottom chip is a 6×6 mm^2 qubit chip.

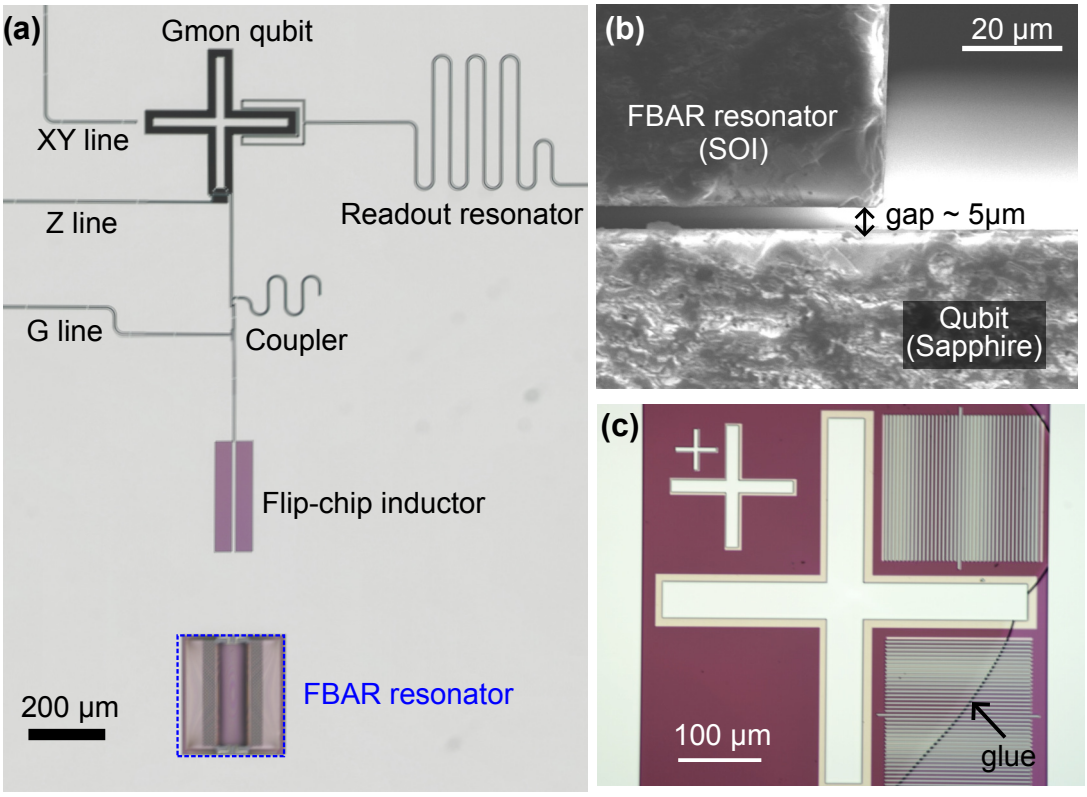

Figure 4.12: A flip-chip integrated device. (a) A FBAR device (blue) is inductively coupled to a Gmon qubit. (b) A cross-section-angled SEM image of the assembled chips. The gap is defined by the thickness of the spacers. (c) The microscopy image of two alignment markers from the aligned chips. Due to the transparency of the sapphire substrate, two alignment markers can be seen and aligned with a microscope.

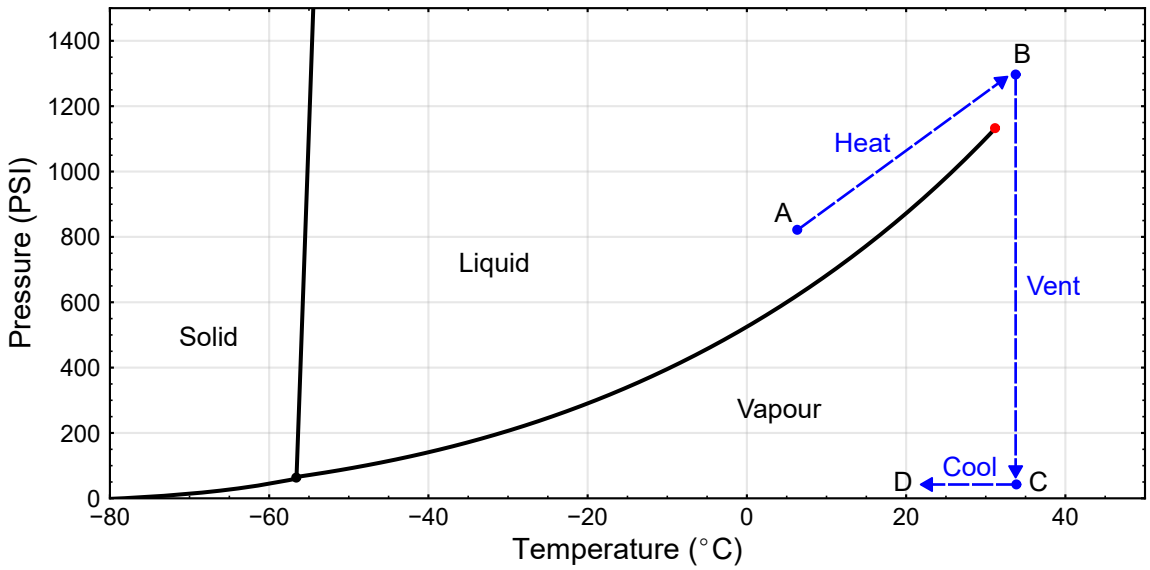

Figure 4.13: CO_2 phase diagram. The black lines show the phase boundaries of solid, liquid and vapour. The intersection of the black lines is known as a triple point (black dot), where the three different phases can coexist. The blue arrows show the trajectory of the CO_2 phase when we operate a CPD. A device is first soaked in liquid CO_2 (A). Then, the chamber is heated up (B) until CO_2 passes the critical point (red dot). Finally, the chamber is vented slowly (C) and cooled down (D).

CHAPTER 5

CHARACTERIZATION OF THE FBAR DEVICES

This chapter is an adaptation from the publication "Measurements of a quantum bulk acoustic resonator using a superconducting qubit" [30][1].

5.1 Microwave transmission measurement

5.1.1 Room temperature measurement

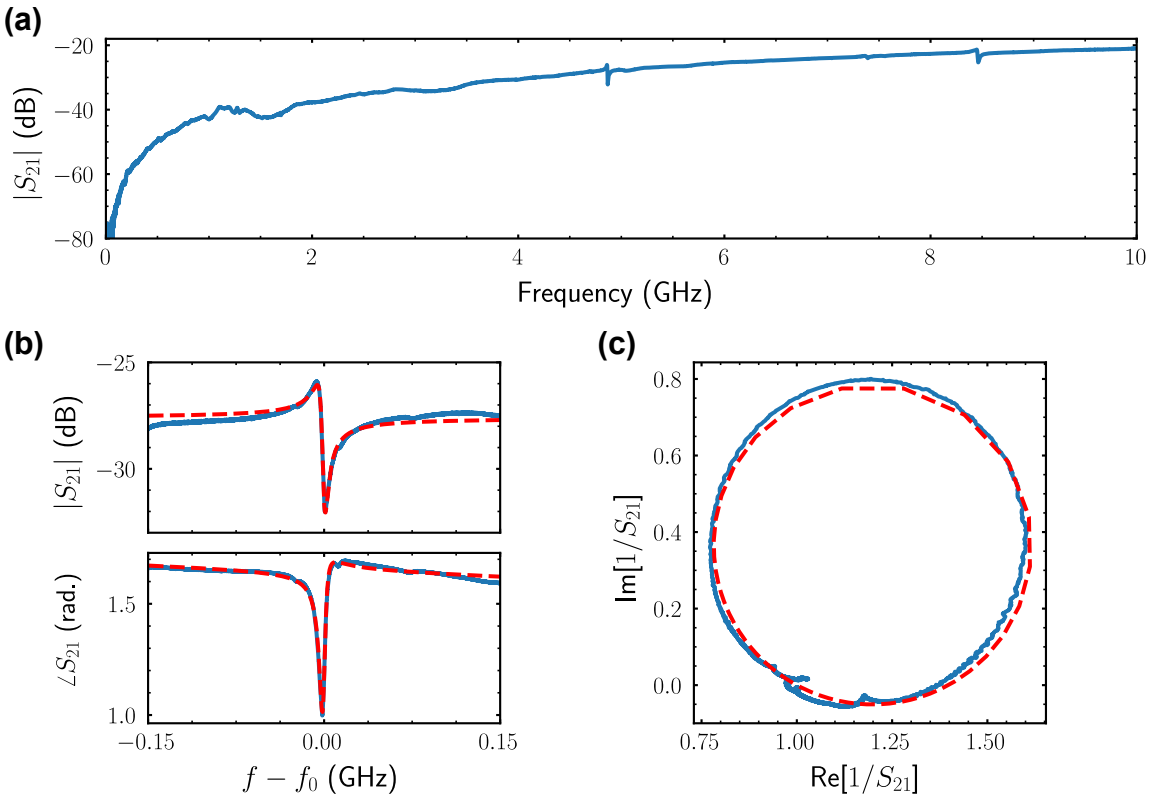

Figure 5.1: Room temperature microwave transmission measurement. (a) The transmission signal magnitude $|S_{21}|$ measured by a vector network analyzer. (b) Magnitude (top) $|S_{21}|$ and phase (bottom) $\angle S_{21}$ near the electromechanical resonance at $f_0 = 4.88\,\text{GHz}$. (c) Inverse S_{21}^{-1} in the complex plane (horizontal axis: real part; vertical axis: imaginary part). The blue lines are experimental data, and the red dash lines are the fits to Eq. 3.16.

1. Originally published in *Applied Physics Letters*. The American Institute of Physics (AIP) reprinting guidelines permit inclusion in this thesis.

The FBAR device is first characterized at room temperature. We probe the electromechanical resonance with the through configuration by using a vector network analyzer. The microwave transmission signal S_{21} is shown in Fig. 5.1 and resonance at about 4.88 GHz is observed as we expected. This resonance yields an internal quality factor $Q_i \sim 1.0 \times 10^3$.

5.1.2 Cryogenic temperature measurement

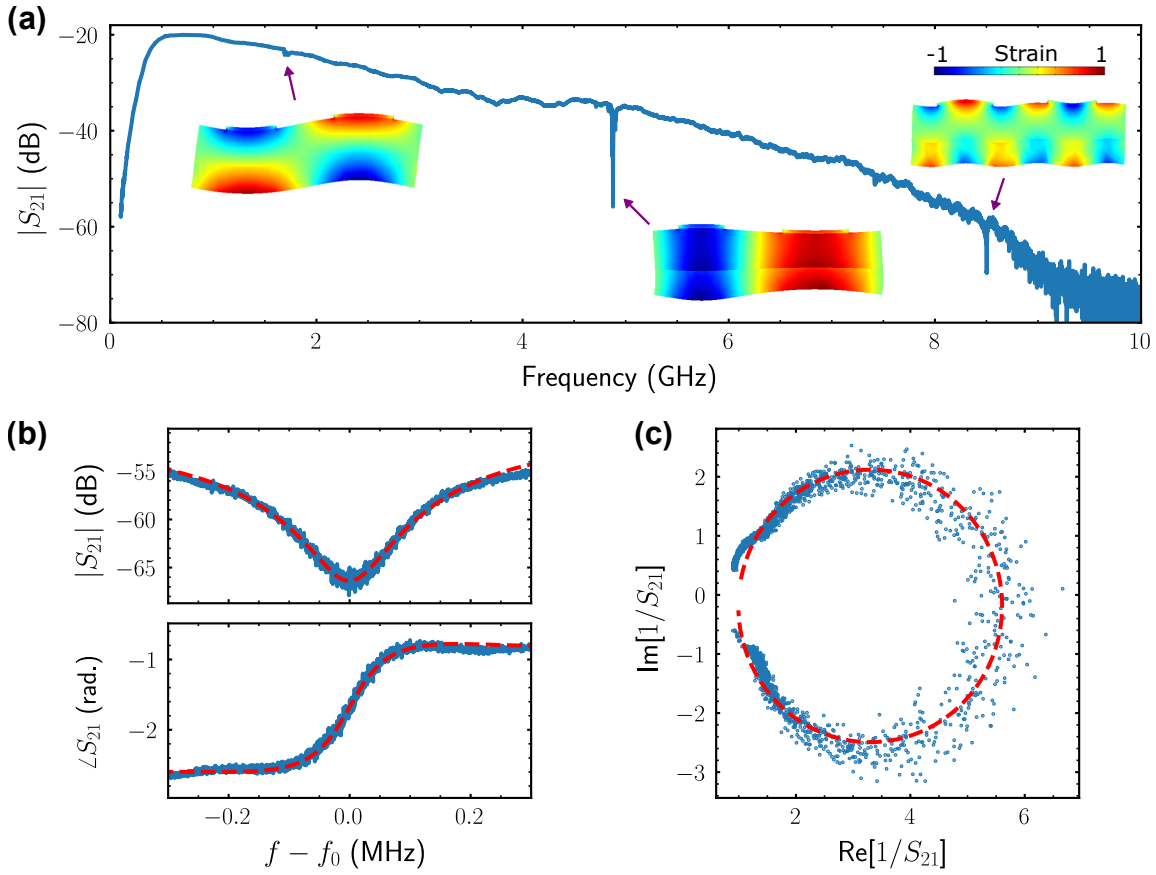

Figure 5.2: Microwave transmission measurements at $T \sim 80\,\text{mk}$. (a) Transmission magnitude $|S_{21}|$ displays three resonances at 1.69, 4.88, and 8.50 GHz, in reasonable agreement with simulations, shown as strain maps (normalized) (inset). (b) Details of the primary resonance at $f_0 = 4.88\,\text{GHz}$, plotted in amplitude (top) and phase (bottom) vs detuning $f - f_0$. (c) Inverse S_{21}^{-1} in the complex plane. The blue dots and lines are experimental data, and the red dash lines are the fits to Eq. 3.16. Based on the discussion in chapter 3, we estimate the excitation corresponding to $\sim 10^6$ phonons.

Next, we characterize the resonator at temperatures below 1 K using an adiabatic demagnetization refrigerator (ADR, base temperature ∼60 mK). The typical wiring diagram for the setup can be found in Appendix. C.1. Excitation signals from a VNA with −40 dBm, which corresponds to about 10^6 phonons in the cavity, pass through a 20 dB attenuator, with the reflection from the device amplified by room-temperature amplifiers with a net gain of 20 dB. The results are displayed in Fig. 5.2. The resonant frequency remains unchanged from room temperature, while Q_i increases by a factor of 40 to $Q_i \sim 4.3 \times 10^4$. As substrate loss is significantly decreased at cryogenic temperatures, additional resonant modes become detectable, consistent with finite-element simulations, shown in Fig. 5.2(a).

5.2 Quantum measurement with a superconducting qubit

After initially characterizing a FBAR device with a VNA, we couple the FBAR device with a qubit. The device is assembled as we have described in chapter 4 (see Fig. 4.11). The integrated device is measured in the dilution refrigerator with the setup shown in Appendix. C.2.

For this hybrid quantum device, a flux-tunable coupler element is placed between the qubit and the resonator. The external flux control line (G-line) is used to control the coupling strength from zero to several megahertz. To better understand our system, the qubit is first detuned away from the mechanical resonance. In this case, the qubit effective inductance L' can be estimated by

$$L' = L_q + \frac{L_g \left[L_c(\Phi) + L_w + L_{fc}\right]}{L_g + L_c(\Phi) + L_w + L_{fc}}. \tag{5.1}$$

Since the coupler inductor L_c can be changed by external flux Φ, the qubit frequency $f_{q,\mathrm{Load}} = \frac{1}{2\pi\sqrt{L'C_q}}$ is expected to exhibit a minimum [97], as shown in Fig. 5.3. With the fit to $f_{q,\mathrm{Load}}$, the minimum $|L_c| = 0.95\,\mathrm{nH}$ is observed and the maximum coupling strength $2g/2\pi$ is expected to be about 10 MHz. With this information, we can select a coupler pulse amplitude to turn on or off the interaction, which is useful for characteriz-

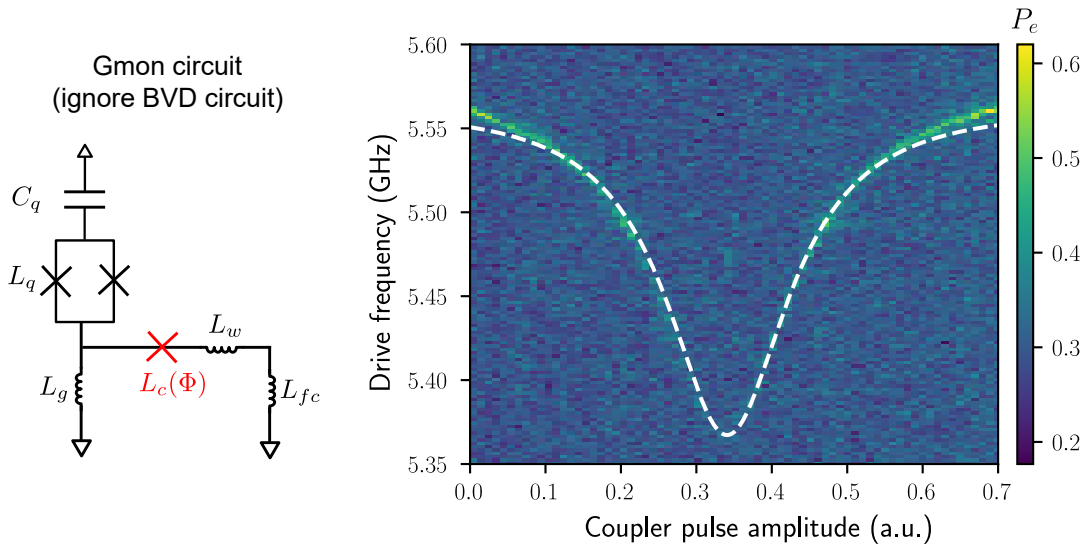

Figure 5.3: Effective qubit frequency for different coupler inductances. The qubit is detuned to 5.55 GHz, which is about 700 MHz above resonator frequency. Left: the Gmon qubit circuit. The coupler inductance depends on the external flux Φ. Right: effective qubit frequency at different coupler pulse amplitude. The color scale represents qubit $|e\rangle$ state probability P_e. The white dash line is the fit to $f_{q,\mathrm{Load}}$.

ing our device. When the coupler is off, we measure the intrinsic qubit $T_1 \sim 20\,\mu\mathrm{s}$ and $T_{2,Ramsey} \sim 3\,\mu\mathrm{s}$, for qubit frequencies ranging from 4.5 to 5.0 GHz, both measured using standard techniques [84](see Fig. 5.4).

As we increase the coupling strength from zero, the qubit response is affected by the resonator and becomes more complex, in particular near the resonator frequency. In Fig. 5.5, we show a qubit spectroscopy measurement with the coupler set to a coupling $2g/2\pi = 9.6\,\mathrm{MHz}$. After setting the qubit frequency, the qubit is gently excited by a $1\mu\mathrm{s}$ excitation microwave tone at the drive frequency, and the qubit excited state probability P_e is measured (color scale). The qubit tunes as expected, exhibiting the expected splitting as it crosses the mechanical resonator frequency at $f_r = 4.86\,\mathrm{GHz}$. There is an additional spurious mode that is weakly coupled to the qubit at 4.87 GHz, with a splitting of about $2g_{\mathrm{spur}}/2\pi = 3.5\,\mathrm{MHz}$. This spurious mode may come from a slight difference between the IDT resonant frequency and that of the FBAR. In Fig. 5.6, we display a qubit-resonator Rabi swap, measured as a function of time (vertical axis) and as a function of qubit detuning from the resonator

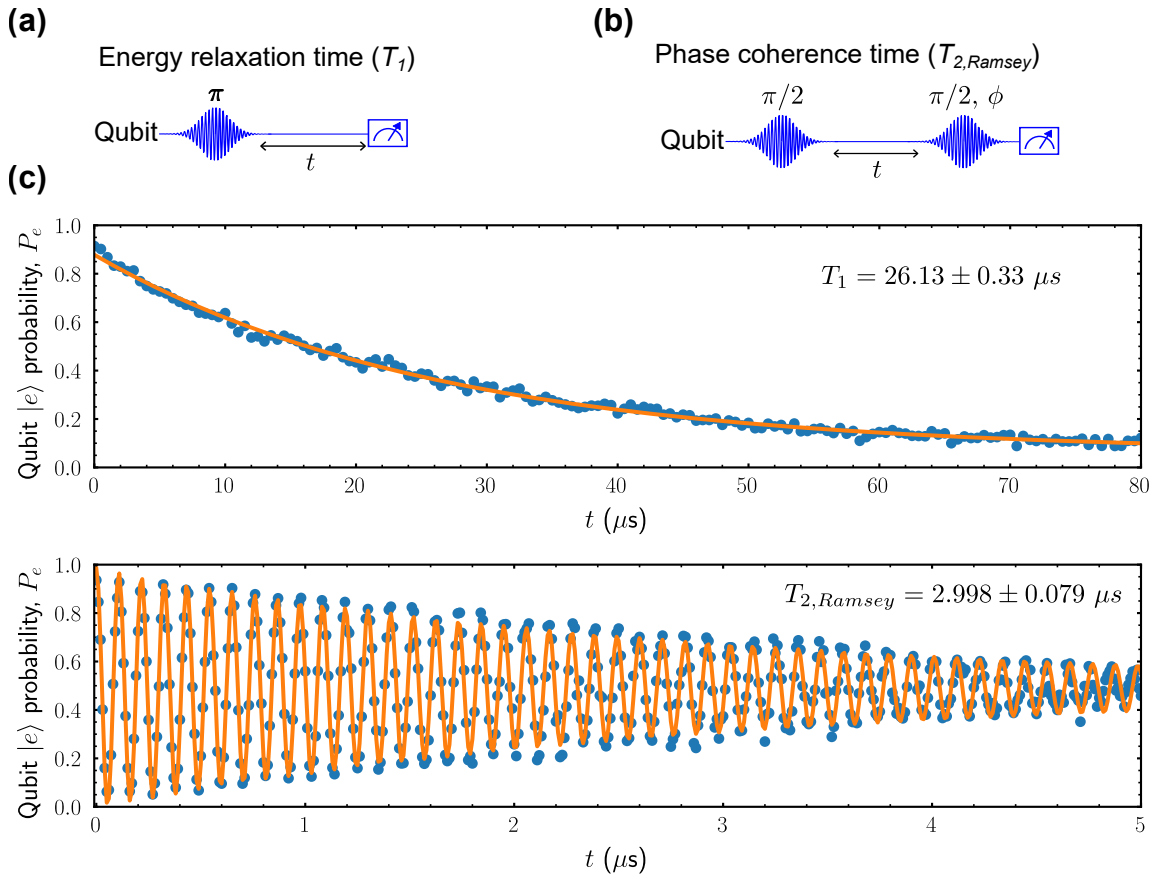

Figure 5.4: Qubit lifetime and coherence time. (a)The pulse sequence for measuring qubit lifetime. The qubit is excited to the $|e\rangle$ state with a π pulse and its energy decay given by excited population P_e is measured after time t. (b) The pulse sequence for measuring qubit coherence time. The qubit is first excited to the superposition of $|g\rangle + |e\rangle$ state with a $\pi/2$ pulse, and we wait some time t for its decay. Then qubit is mapped back along the z-axis (in the Bloch sphere) with another $\pi/2$ pulse. Here, we introduce an additional phase ϕ to the second $\pi/2$ pulse such that the qubit rotates around the z-axis at the rotating frame. This phase is equal to the detuning $\Delta\omega_{\text{fringe}}$ times the delay time t ($\phi = t \times \Delta\omega_{\text{fringe}}$). The qubit $|e\rangle$ state probability is expected to be a cosine oscillation with a decaying exponential envelope. In (b), the $T_{2,Ramsey}$ is measured when qubit is biased to the lower frequency. (c) Qubit lifetime T_1 and coherence time $T_{2,Ramsey}$. The blue dots are the experimental data, and the orange lines are the fits.

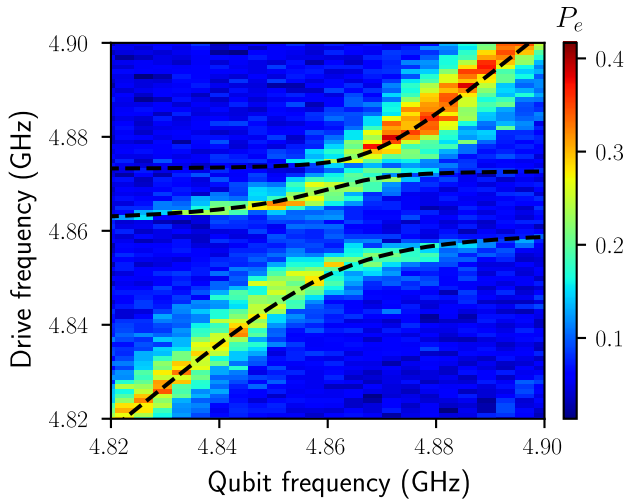

Figure 5.5: Qubit spectroscopy, showing excited state probability P_e vs qubit frequency (horizontal) and microwave pulse frequency (vertical). An avoided-level crossing appears when the qubit and resonator are in resonance. Two energy splittings can be observed, with the larger corresponding to the primary mechanical mode ($2g/2\pi \sim 9.6\,\mathrm{MHz}$) and the other a spurious mechanical mode ($2g_{\mathrm{spur}}/2\pi \sim 3.5\,\mathrm{MHz}$). Dashed lines (black) are the fits to a modified Jaynes-Cummings model including two resonant modes.

frequency (horizontal axis). A microwave pulse places the qubit in its excited state, and the coupling between the qubit and resonator is turned on, initiating the Rabi swap. By measuring the qubit state at different times, we capture the excitation as it is exchanged between the qubit and the resonator. When the qubit-resonator detuning increases, the swap rate increases but the amplitude decreases. The spurious mode interferes with this process, generating a non-ideal response, consistent with the spectroscopy measurement. We used numerical simulations to support our experimental results. The simulations use a modified Jaynes-Cummings model, where the qubit is modeled as a two-level system coupled to two harmonic oscillators, representing the main and spurious mechanical modes, with different coupling strengths at the frequencies 4.86 and 4.87 GHz, respectively. The avoided-level crossing in Fig. 5.5 and the Rabi swap measurement in Fig. 5.6 are both supported by this model, from which we extract a $T_{1,r}^{\mathrm{spur}}$ lifetime for the spurious mode of ~ 70 ns.

Last, we use the qubit to perform a single-phonon lifetime measurement [22, 116], using the pulse sequences shown in Fig. 5.7. From the decay of $P_e(t)$ with delay t, we extract the

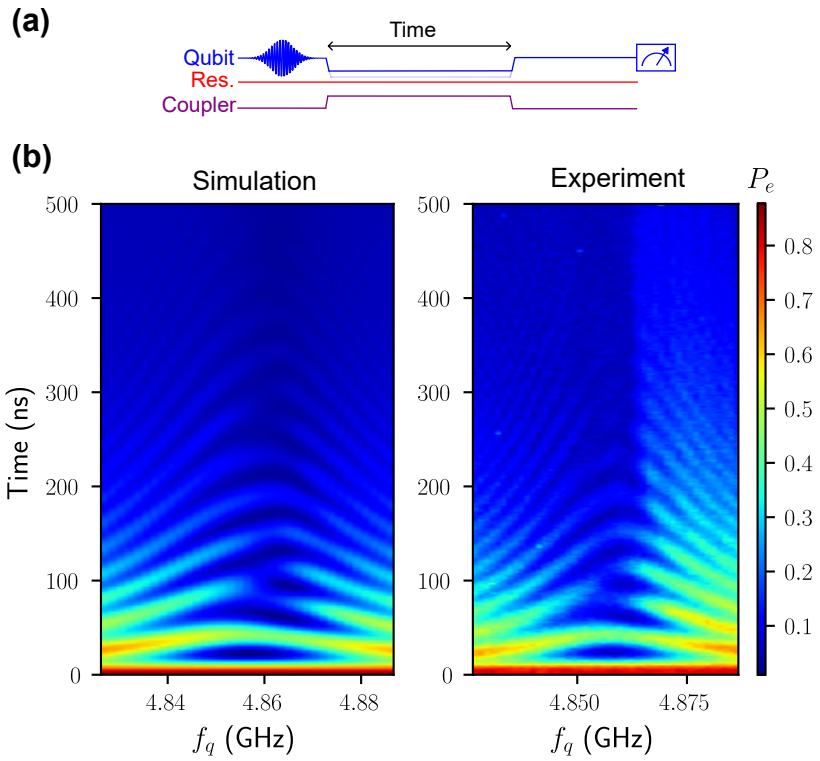

Figure 5.6: (a) Pulse sequence for Rabi measurement. (b) Qubit-resonator Rabi swaps. The probability of the qubit excited state P_e (color scale) is plotted vs qubit frequency f_q (horizontal) and qubit-resonator interaction time (vertical). Coupling strengths are $2g/2\pi \sim 11.2\,\mathrm{MHz}$ and $2g_{\mathrm{spur}}/2\pi \sim 3.5\,\mathrm{MHz}$ for primary and spurious mechanical modes, respectively. Left: simulation results. Right: experimental results.

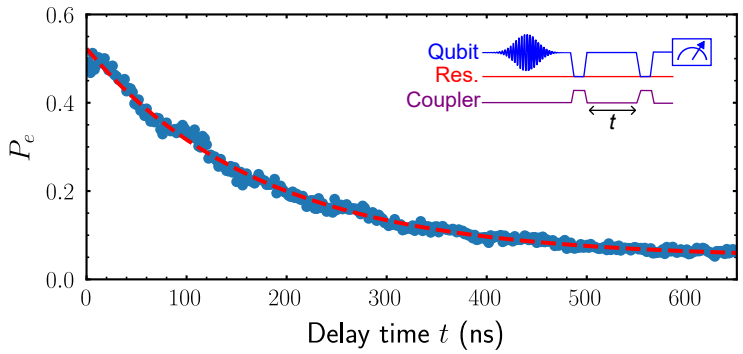

Figure 5.7: Phonon lifetime measurement. The inset shows the pulse sequence. The main panel shows the qubit final excited state probability P_e, where the exponential decay is primarily due to the phonon lifetime of 178 ns, as fit by the dashed line (red).

resonator's energy relaxation time $T_{1,r} = 178 \pm 2$ ns. This corresponds to a single-phonon quality factor $Q_i \sim (5.43 \pm 0.06) \times 10^3$, which is about 10 times smaller than the device measured in Fig. 5.2. This deviation in the quality factor is due to spurious two-level system (TLS) defects that are saturated at the higher powers ($\sim 10^6$ phonons) used in Fig. 5.2 compared to the single-phonon energies used here.

5.3 Hole-burning technique to enhance resonator lifetime

In the previous sections, we have seen the resonator shows a different internal quality factor at different phonon levels. When the resonator is measured with different pump powers, its lifetime increases from about 200 ns to 1 μs, as shown in Fig. 5.8. This trend can be explained by the phenomenological standard tunneling model (STM) of the TLS [119, 120]. The STM describes TLS as a particle in a double-well potential separated by a tunnel barrier. The external strain or electrical field can deform the potential and cause tunneling between two states. The STM model predicts the internal quality factor $Q_{i,r}$ of the resonator follows the given formula

$$\frac{1}{Q_{i,r}(n)} = \frac{1}{\omega_r T_{1,r}(n)} = \frac{1}{Q_{TLS}(n=0)} \frac{\tanh(\frac{\hbar\omega_r}{2k_B T})}{\sqrt{1+\frac{n}{n_c}}} + \frac{1}{Q_{res}} \tag{5.2}$$

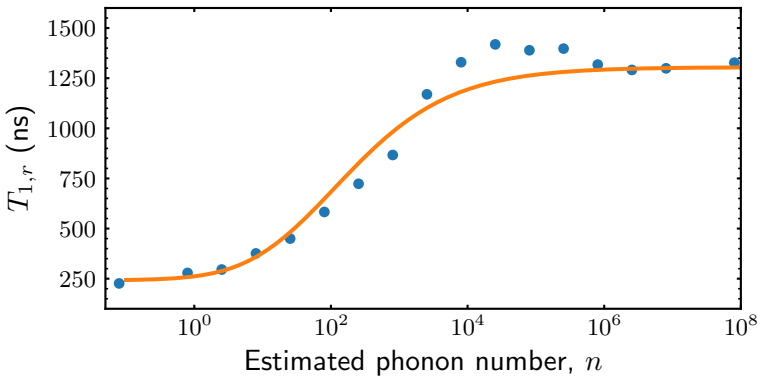

Figure 5.8: Resonator lifetime at different phonon levels. The phonon number in the resonator is estimated by the method described in chapter 3. The blue dots are the experimental data and the orange line is the fit to Eq. 5.2.

where Q_{TLS} is the Q-factor due to the TLS loss, n and n_c represent the averaged and critical phonon number in the resonator respectively. All the other loss not from the TLS is represented by the Q_{res}. Due to the cryogenic temperature environment ($T \sim 60\,\mathrm{mK}$), the $\tanh(\frac{\hbar\omega_r}{2k_BT})$ is very close to 1. From the fit to Eq. 5.2, the $Q_{TLS}(n=0) \sim 8.7 \times 10^3$, $Q_{res} \sim 4 \times 10^4$ and $n_c \sim 4.0$ are extracted.

We now observe that the lifetime of the resonator is limited by the TLS defects, and we want to use a hole-burning technique to improve the quality of our resonator [121]. The idea is to pump the resonator at high power to saturate TLS defects, and then measure the resonator lifetime immediately with a weak probe pulse. Since the TLS defects are temporarily removed, we expect the resonator lifetime is enhanced. We design an experiment by using the setup shown in Appendix. C.3. The pump pulse pumps the resonator with a phonon number $n \sim 10^5$ at 4.883 GHz. We then wait a delay time t and probe the resonator lifetime. The pulse for probing resonator lifetime has phonon number $n \sim 2.5 \times 10^2$, which is not at the single phonon level and will saturate part of the TLS defects. With this pulse sequence, we find that resonator lifetime can be enhanced by a factor of 4 to $\sim 1.5\,\mu$s when the delay time $t < 400\,\mathrm{ns}$. We also perform a control experiment where the pump pulse is removed, and the resonator then has a lifetime of about 500 ns for all the delay time t, which is what we expect for a measurement pulse with such input power. The results of the

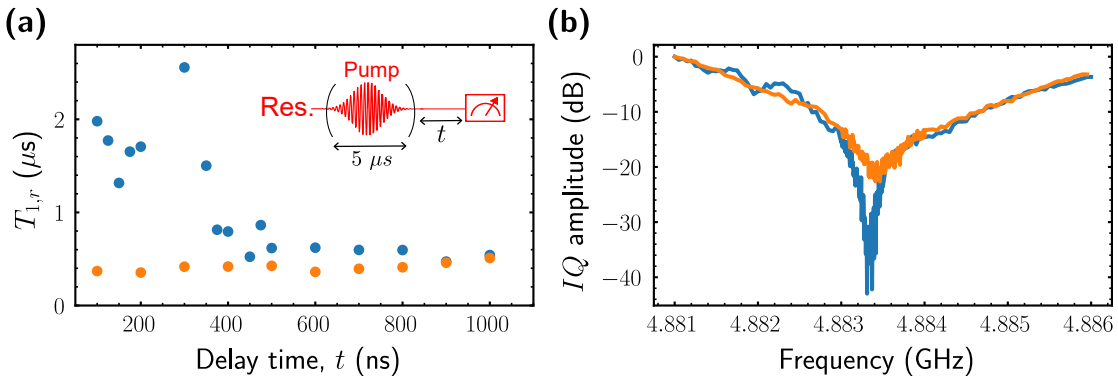

Figure 5.9: (a) Enhancement of the resonator lifetime by hole-burning pulse. The inset shows the pulse sequence for this experiment. The pump pulse length is about 5 μs. (b) The IQ-amplitude of the transmission measurement with two different pulse sequences at the delay time $t = 200$ ns. The background is subtracted and normalized to 0 dB. The blue dots show the resonator lifetime when the hole-burning pulse is applied. The orange dots are the controlled experiment where the hole-burning pulse is removed.

hole-burning experiment are shown in Fig. 5.9.

This hole-burning experiment indicates that we can temporarily remove TLS defects and improve the quality of the resonator in a certain amount of time. This technique in principle can be integrated into our qubit-resonator device by introducing an extra pump line coupled to the resonator. However, due to the high-power pump pulse, this strong microwave pulse can heat the qubit, and the qubit cannot be operated at the single photon level anymore. To apply this technique to a qubit-resonator experiment, more sophisticated circuits need to be designed and tested.

CHAPTER 6

CONCLUSION AND OUTLOOK

In this thesis, we use a new materials combination to design a suspended electromechanical resonator with a resonance frequency of just below 5 GHz. For this resonator, an aluminum-nitride-based interdigital transducer with silicon-based acoustic mirrors is fabricated to eliminate the loss to the substrate. The resonator is characterized by a VNA, and yields an intrinsic quality factor $Q_i \sim 4.3 \times 10^4$ at cryogenic temperature. The resonator is also integrated and inductively coupled to superconducting circuits by a flip-chip technique. Due to the strong piezoelectric response, we can use the superconducting qubit to measure the resonator lifetime at a single phonon level, and we find its $Q_i \sim 5.43 \times 10^3$. These quality factors are roughly 20 times and 200 times higher than those obtained in our previous experiment [22] on thin-film bulk acoustic resonators, although they do not yet approach those on wafer-thickness bulk resonators. Besides, the resonator quality factor shows a strong power-dependent behavior, which implies TLS contamination is a dominant source for limiting the resonator lifetime at a single phonon level. Those TLS defects can be saturated by a hole-burning technique, and the resonator lifetime can be enhanced temporarily, as we also demonstrated in this thesis. This opens the door for having a high-quality resonator without needing to improve material quality and holds promise for making very small form-factor resonant acoustic cavities operating in the quantum limit.

With this platform, several potential experiments can be implemented in the future. For example, we can scale up the systems to two nodes. Each node has a qubit and a resonator as described in the thesis, and the qubit from each node are coupled together. With this configuration, we can address fundamental physics questions on the entanglement of macroscopic objects [62]. With the Gmon architecture and flip-chip technique, the multi-phonons entanglement in separated mechanical resonators can be implemented in our system [122]. Another interesting experiment is related to topological physics in mechanical systems. Recent research [123] demonstrates the topological state in the mechanical system

can be generated with similar materials and suspended geometry. Combining this idea and integrating it with the qubit, we can study topological physics in the mechanical system at a single phonon level.

For electromechanical resonators, piezoelectric materials are commonly used for maintaining a strong coupling rate, but they are usually lossy and would limit the resonator energy relaxation lifetime. Recently, Ref. [124] developed an electromechanical resonator without using any piezoelectric material, and a large coupling rate can be obtained with a strong electrostatic field. With this approach, they have significantly improved the lifetime of the resonator ($T_{1,r} \sim 265\,\mu$s, $T_2 \sim 5\,\mu$s) while keeping the coupling strength at $\sim 1.1\,$MHz. This device opens several possibilities for many advanced quantum experiments. For example, the theory of quantum random access memory (QRAM) can be tested with this resonator [125]. With a QRAM in a quantum computer, quantum information can be read and written more efficiently [126], and this may lower the cost and efforts of building a quantum computer.

Furthermore, people have considered building a quantum computer by linear circuits [127, 128]. The linear quantum computer usually requires a much larger Hilbert space for storing quantum information. Because of the slow speed of sound, the multi-mode phonon cavities with small mode volumes can be engineered, and each resonant mode can be used for storing quantum information. As a result, people may be able to make a linear quantum computer with a small form factor based on quantum acoustics. However, with this approach, a mechanical resonator with lifetime $\sim 1\,$ms may need to be developed.

APPENDIX A

FABRICATION PROCEDURE AND RECIPES

In this chapter, we provided detailed information about the fabrication process and our recipes. Most of the recipes were initially developed from UCSB [79, 129], and then were modified to fit our instruments at the Pritzker Nanofabrication Facility located at the University of Chicago. After several years of evolution, these procedures are stable and repeatable and have been used in many different experiments.

A.1 Silicon oxide stop layer deposition procedure

1. Clean the diced chip by Nanostrip (80 °C, 10 minutes) and then BHF (5 minutes).
2. Bake at 115 °C for 10 minutes.
3. Deposit SiO_x by PECVD tool[1] with parameters in Table A.1.
4. Pattern SiO_x stop layer with optical lithography (see Appendix A.8.2).
5. Wet etch the SiO_x by BHF for 1 minute.
6. NMP strips photoresist following Section A.8.3.
7. Nanostrip at 80 °C for 10 minutes.
8. Inspect under the microscope.
9. Measure SiO_x film stress and thickness with a profilometer.
10. Measure silicon surface roughness by an AFM. The ideal RMS roughness should be about 1 nm.

1. The tool model is Vision 310 PECVD from Plasma-Therm, LLC.

Pressure	800 mTorr
RF power	50 W
5%SiH_4 flow	915 sccm
N_2O flow	685 sccm
Deposition time	45 s

Table A.1: PECVD SiO_x growth recipe.

A.2 AlN sputtering procedure

1. Solvent clean following Section A.8.1.

2. Place the wafer into the wafer carrier with a spring holder, and then seal the wafer carrier with plastic bags.

3. Sputter AlN at Argonne National Laboratory.

   (a) Load the wafer into a cassette and make sure the wafers are placed in the correct orientation and positions. Use the adaptor if it is not a 4-inch wafer.

   (b) Run the script, and a transferred arm moves the wafer from the chamber module (CM) to the processing module (PM).

   (c) Sputter AlN, using the recipes listed in Section A.8.4. The wafer should be automatically transferred back to CM after sputtering.

4. Unload the wafer.

5. Measure the AlN film properties, including crystal orientation, film thickness, and surface roughness[2].

2. Crystal orientation is measured by the Brucker D8 X-ray diffraction tool in CNM at Argonne National Laboratory. Film thickness and surface roughness are both measured at PNF, using the Horiba UVISEL 2 spectroscopic ellipsometer and Bruker Dimension Icon AFM, respectively.

A.3 Gold and Chromium markers deposition procedure

1. Solvent clean following Section A.8.1.
2. Pattern markers with optical lithography (see Appendix A.8.2). The AZ1:1 developer is used here for avoiding damaging the AlN layer.
3. Deposit Cr/Au marker with electron-beam (e-beam) evaporator (no substrate rotation).
   (a) Deposit 20 nm Cr with at 0.1 nm/s.
   (b) Deposit 50 nm Au with at 0.2 nm/s.
4. Liftoff process following Section A.8.5.
5. Inspect under the microscope.
6. Dice the sample into smaller chips if necessary.

A.4 AlN dry etching procedure

1. Solvent clean following Section A.8.1.
2. Spin coat Hexamethyldisilazane (HMDS) at 4500 rpm for 60 seconds.
3. Spin dry HMDS at 4500 rpm for 60 seconds.
4. Pattern an area for silicon phononic device with optical lithography (see Appendix A.8.2). The AZ1:1 developer is used here for avoiding damaging AlN layer.
5. Reflow the photoresist by heat it at 115 °C hotplate for 3 minutes.
6. Dry etch 330 nm AlN using with parameters listed in Table A.2.
7. NMP strips photoresist following Section A.8.3.

8. BHF dip to clean SiO_x stop layer for 1 minute.

9. Inspect under the microscope and check the AlN thickness with a profilometer.

10. Check the length of the ramp by atomic force microscopy[3].

Pressure	3 mTorr
ICP bias power	400 W
ICP power	200 W
Cl_2 flow	15 sccm
O_2 flow	2 sccm
Etching time	57 seconds

Table A.2: AlN etching recipe.

A.5 Fabrication procedure for silicon devices

In this thesis, we use the process described below for fabricating silicon phononic crystals, but the same procedure can also be used for making silicon photonics or silicon other devices [17].

1. Solvent clean following Section A.8.1.

2. Pattern and develop 6% H-SiQ following Section A.8.6.

3. Define the etching area for phononic crystals by using optical lithography (see Appendix A.8.2).

4. Dry etch silicon phononic crystals by using the parameters listed in Table A.3. The sidewall angle of the device is $\sim 95^\circ$ by using this etching recipe and 6% H-SiQ masks

3. If the AlN film thickness or the alignment between each lithography is not accurate, the wider and deeper notch is created. This notch makes the transfer efficiency of the symmetric lamb wave becomes lower due to the mode conversion. However, this only is demonstrated in simulations [81], not observed in our experiment.

(see Fig. A.1). The properties of crystals are affected by the sidewall angle, and this must be considered when designing the device.

5. NMP strips photoresist following Section A.8.3.

6. O_2 downstream clean the sample if necessary.

7. Clean H-SiQ by BHF dip for 1 minute.

Pressure	3 mTorr
ICP bias power	120 W
ICP power	100 W
Cl_2 flow	15 sccm
O_2 flow	2 sccm
Etching time	68 seconds

Table A.3: Silicon etching recipe.

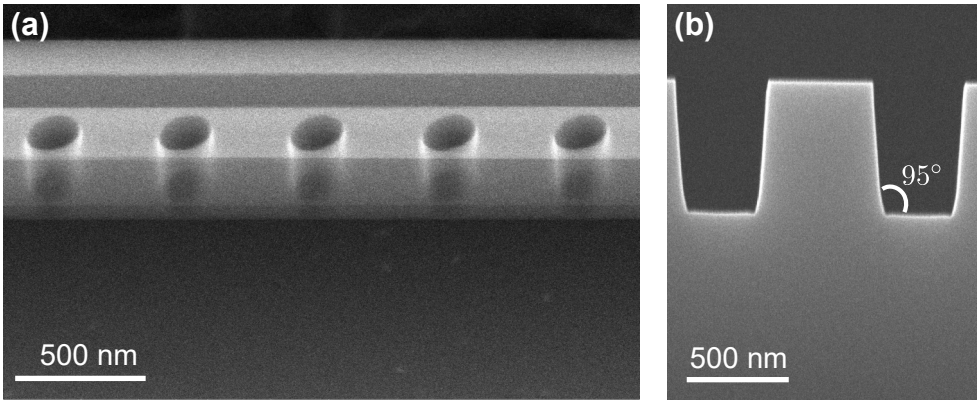

Figure A.1: The angled SEM images show (a) the silicon nanobeam and (b) its sidewall angle after etching.

A.6 Fabrication procedure for interdigital transducers

1. Solvent clean following Section A.8.1.

2. Spin coat and develop PMMA bilayer following Section A.8.7.

3. Deposit 30 nm aluminum following Section A.8.8.

4. Liftoff process for IDT

   (a) Immerse the sample in acetone (suspended face-down, at least 12 hours), and cover the beakers with glass.[4] This step usually is an overnight process.

   (b) After overnight liftoff, squirt the sample gently with acetone on both sides. Most of the metal should fall off easily.

   (c) Eyeball the sample quickly when the surface is still wet. Usually, the patterns with gradient color can be observed due to IDT finger pairs.

   (d) If the diffraction patterns are not observed, then apply gentle sonication at minimum power at 104 kHz for 1 minute.

   (e) Transfer the sample into the IPA bath. Again, gentle sonication can be applied if necessary

   (f) N_2 dry the sample.

5. Inspect the sample under the microscope and check the IDT dimension under a scanning electron microscope.

A.7 Fabrication procedure for release windows

1. Solvent clean following Section A.8.1.

2. Pattern release windows with optical lithography (see Appendix A.8.2).[5]

4. Make sure the acetone is sufficient since acetone evaporates slowly during the liftoff process.

5. Here, we use AZ1518 photoresist instead since we need a thicker photoresist. The dimension of the release window is not critical, so the dose energy and developing time can be increased intentionally to avoid under-development.

3. Dry etch 330 nm AlN and 220 nm silicon using with parameters listed in Table A.2, but change the etching time to 90 seconds.

4. NMP strips photoresist following Section A.8.3.

5. Dice the sample into smaller chips if necessary.

A.8 Commonly used recipes

A.8.1 Solvent clean procedure

1. Acetone 5 minutes with sonication.

2. IPA 5 minutes with sonication.

3. Rinse the sample with deionized (DI) water for 30 seconds.

4. N_2 dry the sample.

5. Bake the sample at 115 °C for 10 minutes for dehydration.

A.8.2 Optical lithography with positive photoresist AZ1512

1. Solvent clean following Section A.8.1.

2. Spin coat $\sim 2\,\mu m$ AZ 1512 photoresist (4500 rpm, 45 s)[6].

3. Soft bake sample at 95 °C for 1 minute.

4. Exposure in MLA150 instrument I[7].

   (a) Laser: 375 nm

   (b) Dose: $225\,mJ/cm^2$

6. AZ1512 photoresist can be replaced to AZ1518 if the thicker photoresist is needed

7. Here we intentionally overexpose the sample to avoid any photoresist residue.

(c) Focus: 0

(d) Critical dimension bias: -200 nm

5. Post bake sample at 115 °C for 1 minute.

6. Development

   (a) AZ MIF 300 for 1 minute with gentle agitation[8].

   (b) DI water for 30 seconds.

   (c) N_2 dry the sample.

7. Inspect under the microscope.

A.8.3 Strip photoresist

1. O_2 downstream clean to remove crosslink in photoresist (RF power: 300 W, O2 flow: 200 sccm, time: 4 minutes, temperature: 70 °C).

2. Put the sample in NMP and cover the dish with aluminum foil (80 °C heated bath for 20 minutes, with gentle sonication).

3. Squirt the sample on both sides with IPA and then place the sample in an IPA bath for 5 minutes

4. N_2 dry the sample.

A.8.4 AlN sputter procedure and recipe

The AlN sputtering job flow consists of three parts: etching, heating, and sputtering. In OEM sputtering system, each part has its own parameters and can be adjusted based on our purpose. The following is a standard job flow used in this thesis.

8. If AZ1:1 developer is used, the development time is 4 minutes.

1. Gentle Ar etch to clean substrate

   (a) Power: 200 W

   (b) Ar flow: 4 sccm

   (c) Time: 30 seconds

2. Heat the substrate

   (a) Power: 100% (maximum power of external heater)

   (b) Heat the substrate for 40 seconds.

3. Sputter AlN on the wafer

   (a) Pressure: 6 mTorr

   (b) Ar flow: 5 sccm

   (c) N_2 flow: 17 sccm

   (d) Cathode Power: 6000 W

   (e) Targeted AlN thickness: 330 nm

   (f) SAU: 15 Ω (position 3)

4. Wait 5 minutes for cooling down.

A.8.5 NMP liftoff process

1. Place the sample face-down in NMP and cover the dish with aluminum foil (80 °C heated bath for 3 to 4 hours, no sonication).

2. Squirt the sample on both sides with IPA, and then place the sample in an IPA bath for 5 minutes.

3. N_2 dry the sample.

A.8.6 H-SiQ development process

In the past, the Dow XR1541 series of hydrogen silsesquioxane (HSQ or H-SiQ) is used in our cleanroom. However, its quality is very sensitive to the temperature and it has only 6 months lifetime (also 4 months lead time). As a result, the recipe is not stable due to the uncertainty of the Dow HSQ. This is a well-known issue and the other company, Dischem, provides an alternative solution. Dischem develops and sells a very similar H-SiQ e-beam resist product, and it turns out their resist has better quality. Dischem H-SiQ has more than one year lifetime when it is stored in the fridge ($-5\,^{\circ}$C), and the lead time is relatively short. In this thesis, 6% H-SiQ from Dischem is used for all the experiments, and the typically developed mask is shown in Fig. A.2. The process described below can be applied to different concentrations of H-SiQ, and the thicker or thinner H-SiQ can be achieved[9].

1. Inspect the sample under the microscope and make sure the surface is clean.
2. Spin coat 110 nm H-SiQ
   (a) Spin the sample at 3000 rpm for 60 seconds.
   (b) Soft bake at 90 °C for 4 minutes.
3. Align and mount the sample in the e-beam writer as soon as possible, since the H-SiQ can interact with water vapor in the air and thus its quality can be degraded.
4. Exposure
   (a) Dose: 1700 µC/cm^2 (with proximity effect correction)
   (b) Current: 1 nA
   (c) Beam voltage: 100 kV
5. H-SiQ Development

9. For example, $\sim$ 530 nm H-SiQ (14%) can be realized by using the similar process.

(a) Immerse the sample in the 25% TMAH for 60 seconds.

(b) Rinse the sample with gently flowing DI water from the tap for 90 seconds. Since TMAH is a very sticky developer, using the flowing DI water to clean the sample surface is necessary.

(c) Immerse the sample in a DI water bath for 30 seconds.

(d) N_2 dry the sample.

6. Post-exposure bake the sample at 300 °C for 15 minutes.

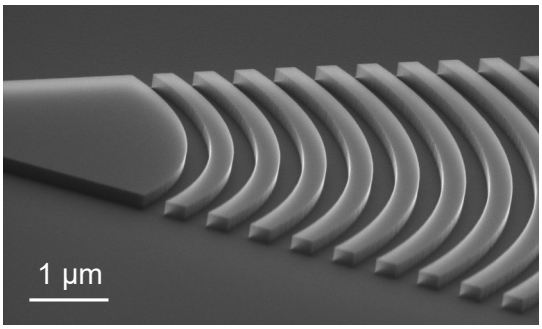

Figure A.2: An angled SEM image of a 6% H-SiQ e-beam resist mask.

A.8.7 PMMA bilayer process

1. Inspect the sample under the microscope and make sure the surface is clean.

2. Spin coat 495A4 PMMA at 5000 rpm for 45 seconds.

3. Bake the sample at 180 °C for 5 minutes.

4. Spin coat 950A2 PMMA at 1500 rpm for 45 seconds.

5. Bake the sample at 180 °C for 5 minutes.

6. Thermal gold evaporation

(a) Place the sample in an e-beam evaporator (Angstrom Nexdep Thermal E-beam Evaporator II), and pump down the chamber pressure below 10^{-5} mTorr.

(b) Deposit 10 nm of Au at 0.05 nm/s with 10 rpm substrate rotation.

7. Exposure

   (a) Dose for IDT: 410 μC/cm^2 (with proximity effect correction)

   (b) Current for IDT: 30 nA

   (c) Dose for large ground plane: 500 μC/cm^2 (with proximity effect correction)

   (d) Current for the large ground plane: 100 nA

   (e) Beam voltage: 100 kV

8. Remove thermal gold by TFA Au etcher (10 seconds).

9. PMMA development

   (a) Develop sample in MIBK/IPA (1:1) mixture for 60 seconds (without agitation).

   (b) Immerse the sample in IPA for 60 seconds (without agitation).

   (c) N_2 dry the sample.

10. O_2 downstream clean to remove PMMA residue (RF power: 50W, O2 flow: 200 sccm, time: 25 seconds, temperature: 25 °C).

11. Inspect the sample under the microscope.

A.8.8 Aluminum deposition for liftoff process

1. Inspect the sample under the microscope

2. Load the sample into Angstrom Evo-Vac E-beam Evaporator.

3. Pre-condition the chamber by depositing 100 nm of Ti at 0.05 nm/s and 50 nm of Al at 0.1 nm/s. In this step, the substrate shutter is closed. The chamber pressure should decrease to 10^{-7} mTorr (or below) after pre-condition.

4. Open the substrate shutter and deposit 30 nm aluminum without substrate rotation.

A.8.9 SU8 3005 spacer process

This process is designed for aluminum on a sapphire substrate. Modification is needed if the substrate is different.

1. Spin coat 5 µm SU8 at 2500 rpm for 45 seconds.
2. Soft-bake the sample at 95 °C for 4 minutes.
3. Expose sample in MLA instrument II[10].
   (a) Laser: 375 nm
   (b) Dose: 800 mJ/cm^2
   (c) Focus: 0
   (d) Critical dimension bias: -200 nm
4. Post-bake the sample at 95 °C for 4 minutes.
5. SU8 development
   (a) Place the sample face-down in the SU8 developer for 90 seconds (without agitation).
   (b) Transfer the sample to the second SU8 developer bath. Place the sample face-down for 30 seconds (without agitation).
   (c) Transfer the sample into the IPA bath. Place the sample face-down for 60 seconds (without agitation).
   (d) N_2 dry the sample. If any residue is observed by eyeballing, immediately put the sample back to the SU8 developer for additional 30 seconds, and then transfer the sample to an IPA bath for 10 seconds.

10. PNF has two MLA instruments. The parameters listed here are tested in the 2nd MLA instrument, but the procedure should work in both instruments since they have similar properties.

6. Measure the SU8 spacer thickness with a profilometer.

7. Hard bake SU8 spacer at 95 °C for 10 minutes.

APPENDIX B

CIRCUIT TRANSFORMATION AND FORMULA

In this chapter, we provide several useful circuit transformation formulas. Those formulas can be found or derived by following the instruction in Ref. [110].

B.1 Replace a mutual inductor with a T-circuit

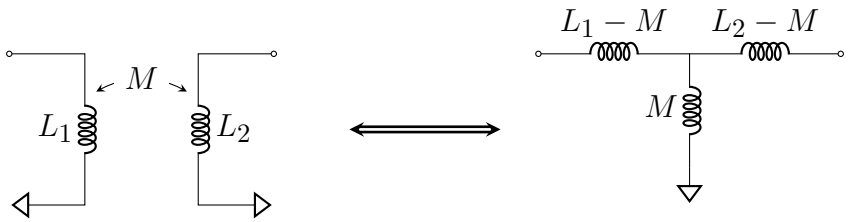

Figure B.1: T-equivalent circuit of mutually coupled inductors.

B.2 Conversion between Π-circuit and T-circuit

In Fig. B.2, the following relations can be derived:

$$Z_1 = \frac{Z_A Z_B}{Z_A + Z_B + Z_C}, Z_2 = \frac{Z_B Z_C}{Z_A + Z_B + Z_C}, Z_3 = \frac{Z_A Z_C}{Z_A + Z_B + Z_C}. \tag{B.1}$$

$$Z_A = \frac{Z_1 Z_2 + Z_1 Z_3 + Z_2 Z_3}{Z_2}, Z_B = \frac{Z_1 Z_2 + Z_1 Z_3 + Z_2 Z_3}{Z_3}, Z_C = \frac{Z_1 Z_2 + Z_1 Z_3 + Z_2 Z_3}{Z_1}. \tag{B.2}$$

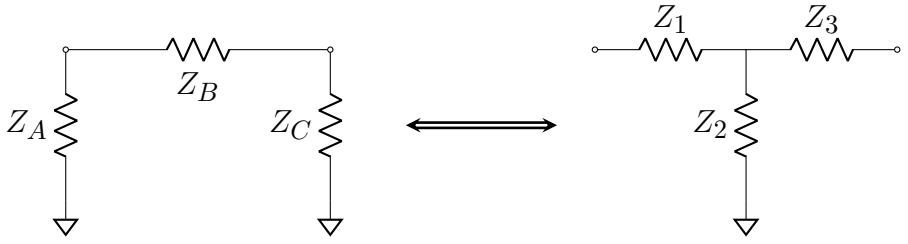

Figure B.2: Π circuit to tee circuit transformation.

B.3 A control line inductively couples to external circuits

In Fig. B.3, a control line is inductively coupled to a two-port circuit with a mutual inductance M. The control line has an impedance Z_l and it is in series with Z_0. Two small coupling inductors in both branches are ignored. By using Kirchhoff's circuit laws, we have

$$-(Z_l + Z_0)I_2 - j\omega M I_1 = 0 \tag{B.3}$$

$$-j\omega M I_2 = V \tag{B.4}$$

where V and I_1 are the voltage and the current around the coupling point on the upper circuit branch, and I_2 is the current in the control line. From the two equations above, we can get the equivalent Z as

$$Z = \frac{V}{I_1} = \frac{\omega^2 M^2}{(Z_l + Z_0)^2} \tag{B.5}$$

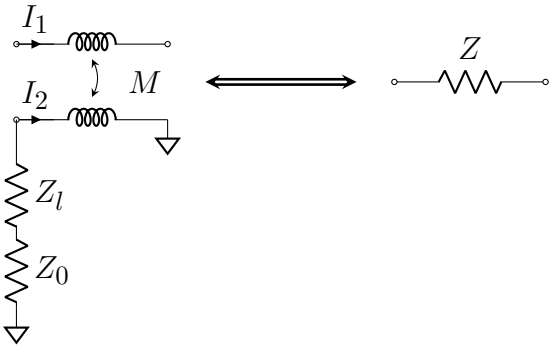

Figure B.3: Inductively couple a control line to an external circuit.

APPENDIX C

EXPERIMENTAL SETUP

In this chapter, we provide the details of the wiring diagrams for each experiment. Fig. C.1, C.2 and C.3 are the typical setups for ADR microwave measurement, qubit-resonator and hole-burning experiments, respectively.

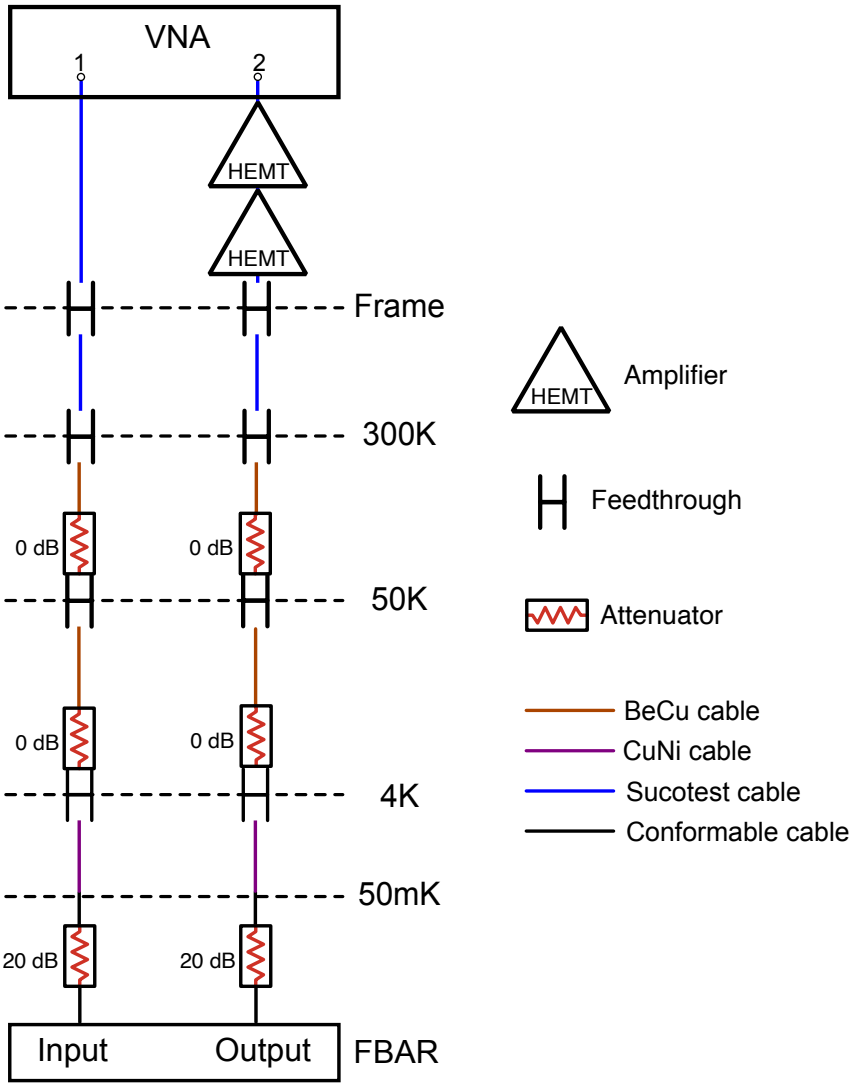

Figure C.1: The typical wiring diagram for microwave measurement in ADR. Different cables are used at different stages in order to avoid thermal noise and electrical loss. VNA: vector network analyzer.

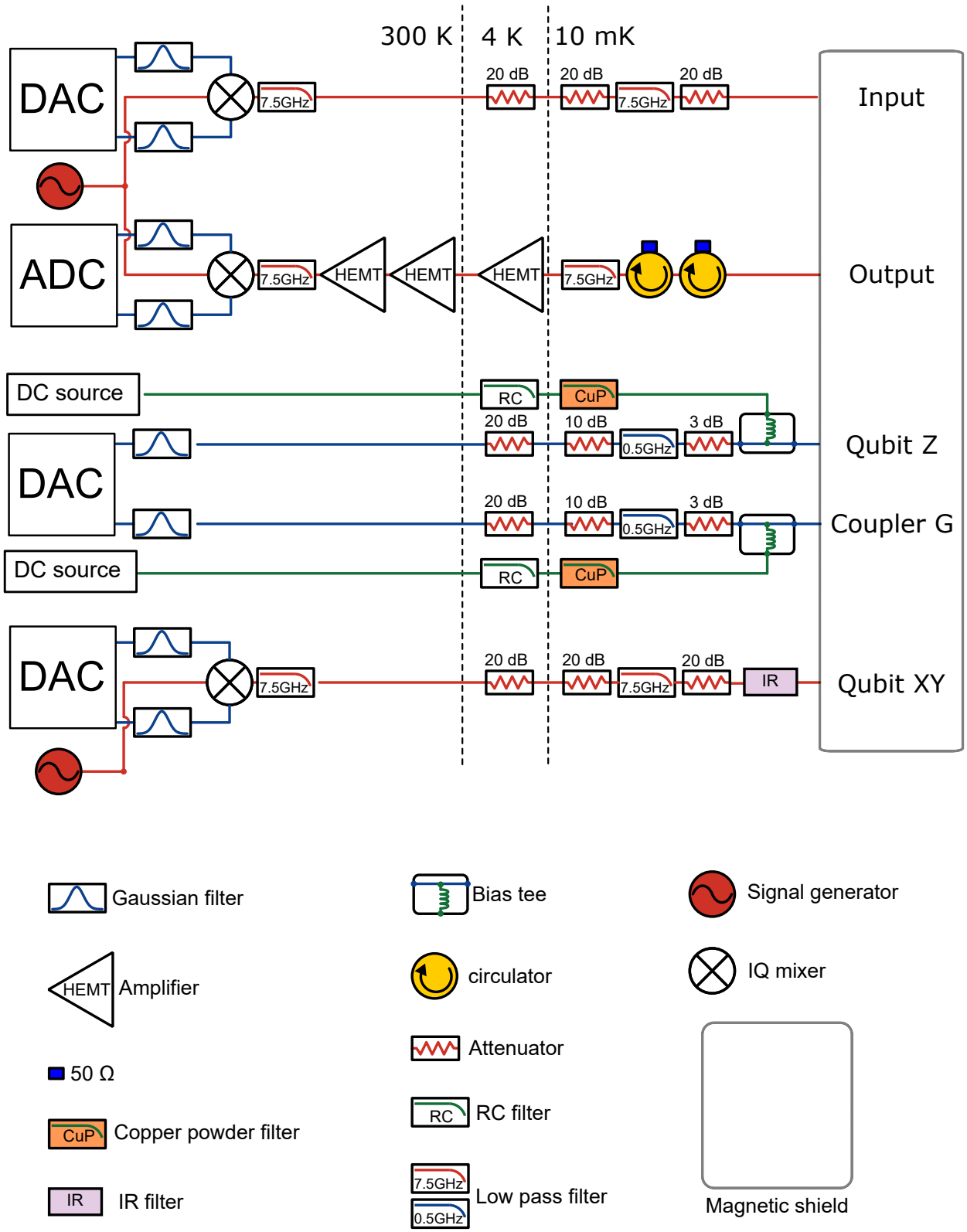

Figure C.2: The wiring diagram for the qubit-resonator experiment. ADC: analog-to-digital converter. DAC: digital-to-analog converter.

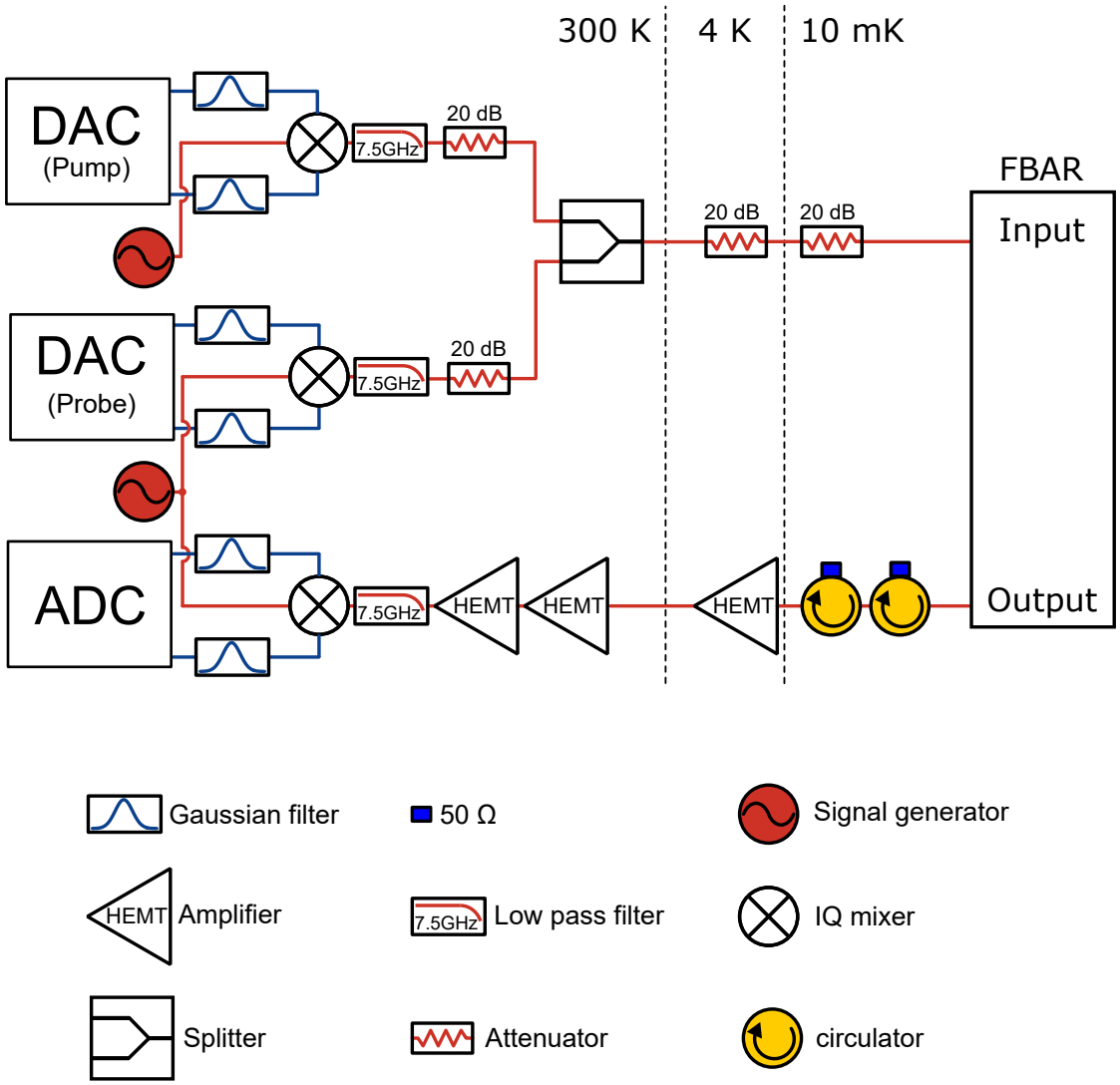

Figure C.3: The wiring diagram for the hole-burning experiment. Two DAC boards are used for generating the hole-burning pulse (pump) and measurement pulse (probe).

APPENDIX D

RESONATORS AND QUALITY FACTORS

For any resonator, its internal quality factor is given by [110]

$$Q_i = \omega_0 \frac{\text{averaged stored energy}}{\text{energy loss per second}} \tag{D.1}$$

where ω_0 is the resonant frequency. If we consider a series RLC resonator[1] shown in Fig. D.1 (a), its internal quality factor Q_i is

$$Q_i = \frac{1}{\omega RC} \tag{D.2}$$

The resistor R represents the internal loss of the resonator. If it is a lossless resonator, $R = 0$ and Q_i is infinity. For this series RLC circuit, its impedance is

$$Z = R + j\omega L - j\frac{1}{\omega C}, \tag{D.3}$$

and its imaginary part vanishes if it is at resonance ($\omega_0 = \frac{1}{\sqrt{LC}}$).

When we want to measure a resonator, we need to couple it to an external circuit, which usually has an impedance $Z_0 = 50\,\Omega$. This makes a resonator become lossy because the energy stored in the resonator decays into the external circuit. As a result, the resonator "overall" quality factor Q is lowered. In general, we can engineer this decay rate κ, which is equal to the inverse of the external quality factor Q_c. The relation of Q_i, Q_c and Q is given by

$$\frac{1}{Q} = \frac{1}{Q_i} + \frac{1}{Q_c}. \tag{D.4}$$

1. The quarter-wave coplanar readout resonator we discuss in this thesis can be modeled as a series RLC resonator[110].

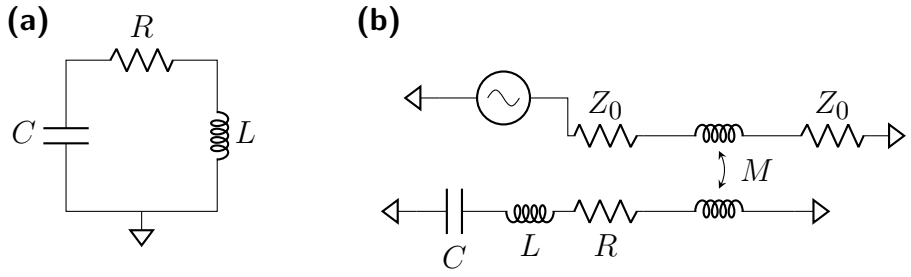

Figure D.1: (a) Schematic of a series RLC resonator. (b) Schematic of a series RLC resonator coupled to an external circuit. The mutual inductance M can be engineered to control the external quality factor Q_c. The external circuit includes a source that can be used to measure the resonator.

In Fig. D.1 (b), a series RLC resonator is inductively coupled to an external source with a mutual inductance M. The transmission signal S_{21} of this circuit is given by [109]

$$\frac{1}{S_{21}} = 1 + \frac{Q_i}{Q_c}\frac{1}{1 + 2jQ_i\delta} \tag{D.5}$$

where $\delta = (\omega - \omega_0)/\omega_0$, and its S_{21} is shown in Fig. D.2.

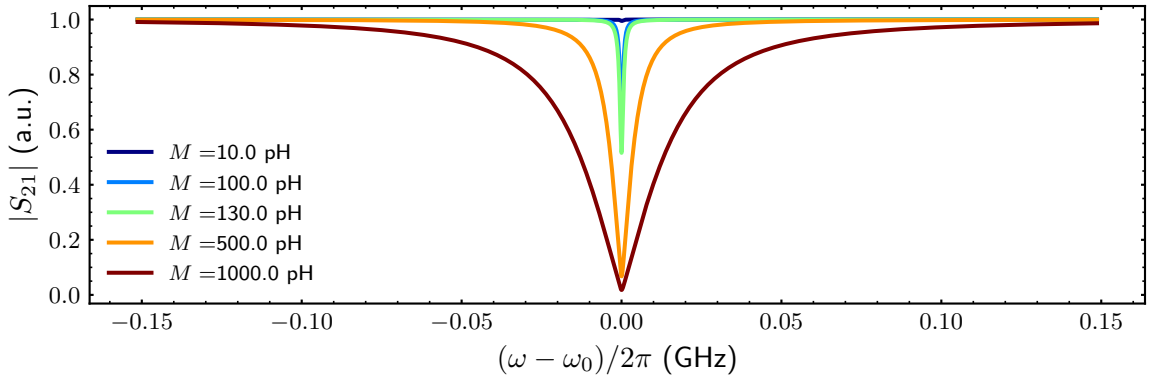

Figure D.2: Transmission signals of a series RLC resonator. For this calculation, $R = 0.1\,\Omega$, $C = 90\,\mathrm{fF}$ and $L = 20\,\mathrm{nH}$ are used. When $Q_i = Q_c$ and the resonator is at resonance, the minimum of the $|S_{21}| = 0.5$.

BIBLIOGRAPHY

[1] Ze-Liang Xiang, Sahel Ashhab, J. Q. You, and Franco Nori. Hybrid quantum circuits: Superconducting circuits interacting with other quantum systems. *Reviews of Modern Physics*, 85(2):623–653, April 2013.

[2] Markus Aspelmeyer, Tobias J. Kippenberg, and Florian Marquardt. Cavity optomechanics. *Reviews of Modern Physics*, 86(4):1391–1452, December 2014.

[3] Gershon Kurizki, Patrice Bertet, Yuimaru Kubo, Klaus Mølmer, David Petrosyan, Peter Rabl, and Jörg Schmiedmayer. Quantum technologies with hybrid systems. *Proceedings of the National Academy of Sciences*, 112(13):3866–3873, March 2015.

[4] C. L. Degen, F. Reinhard, and P. Cappellaro. Quantum sensing. *Reviews of Modern Physics*, 89(3), July 2017.

[5] John J.L. Morton and Patrice Bertet. Storing quantum information in spins and high-sensitivity ESR. *Journal of Magnetic Resonance*, 287:128–139, February 2018.

[6] A. A. Clerk, K. W. Lehnert, P. Bertet, J. R. Petta, and Y. Nakamura. Hybrid quantum systems with circuit quantum electrodynamics. *Nature Physics*, 16(3):257–267, March 2020.

[7] Per Delsing, Andrew N Cleland, Martin J A Schuetz, Johannes Knörzer, Géza Giedke, J Ignacio Cirac, Kartik Srinivasan, Marcelo Wu, Krishna Coimbatore Balram, Christopher Bäuerle, Tristan Meunier, Christopher J B Ford, Paulo V Santos, Edgar Cerda-Méndez, Hailin Wang, Hubert J Krenner, Emeline D S Nysten, Matthias Weiß, Geoff R Nash, Laura Thevenard, Catherine Gourdon, Pauline Rovillain, Max Marangolo, Jean-Yves Duquesne, Gerhard Fischerauer, Werner Ruile, Alexander Reiner, Ben Paschke, Dmytro Denysenko, Dirk Volkmer, Achim Wixforth, Henrik Bruus, Martin Wiklund, Julien Reboud, Jonathan M Cooper, YongQing Fu, Manuel S Brugger, Florian Re-

hfeldt, and Christoph Westerhausen. The 2019 surface acoustic waves roadmap. *Journal of Physics D: Applied Physics*, 52(35):353001, July 2019.

[8] Mohammad Mirhosseini, Alp Sipahigil, Mahmoud Kalaee, and Oskar Painter. Superconducting qubit to optical photon transduction. *Nature*, 588(7839):599–603, December 2020.

[9] Jasper Chan, T. P. Mayer Alegre, Amir H. Safavi-Naeini, Jeff T. Hill, Alex Krause, Simon Gröblacher, Markus Aspelmeyer, and Oskar Painter. Laser cooling of a nanomechanical oscillator into its quantum ground state. *Nature*, 478(7367):89–92, October 2011.

[10] Joerg Bochmann, Amit Vainsencher, David D. Awschalom, and Andrew N. Cleland. Nanomechanical coupling between microwave and optical photons. *Nature Physics*, 9(11):712–716, September 2013.

[11] R. W. Andrews, R. W. Peterson, T. P. Purdy, K. Cicak, R. W. Simmonds, C. A. Regal, and K. W. Lehnert. Bidirectional and efficient conversion between microwave and optical light. *Nature Physics*, 10(4):321–326, March 2014.

[12] Krishna C. Balram, Marcelo I. Davanço, Jin Dong Song, and Kartik Srinivasan. Coherent coupling between radiofrequency, optical and acoustic waves in piezo-optomechanical circuits. *Nature Photonics*, 10(5):346–352, March 2016.

[13] Amit Vainsencher, K. J. Satzinger, G. A. Peairs, and A. N. Cleland. Bi-directional conversion between microwave and optical frequencies in a piezoelectric optomechanical device. *Applied Physics Letters*, 109(3):033107, July 2016.

[14] A. P. Higginbotham, P. S. Burns, M. D. Urmey, R. W. Peterson, N. S. Kampel, B. M. Brubaker, G. Smith, K. W. Lehnert, and C. A. Regal. Harnessing electro-optic correlations in an efficient mechanical converter. *Nature Physics*, 14(10):1038–1042, July 2018.

[15] Linran Fan, Chang-Ling Zou, Risheng Cheng, Xiang Guo, Xu Han, Zheng Gong, Sihao Wang, and Hong X. Tang. Superconducting cavity electro-optics: A platform for coherent photon conversion between superconducting and photonic circuits. *Science Advances*, 4(8), August 2018.

[16] Moritz Forsch, Robert Stockill, Andreas Wallucks, Igor Marinković, Claus Gärtner, Richard A. Norte, Frank van Otten, Andrea Fiore, Kartik Srinivasan, and Simon Gröblacher. Microwave-to-optics conversion using a mechanical oscillator in its quantum ground state. *Nature Physics*, 16(1):69–74, October 2019.

[17] G.A. Peairs, M.-H. Chou, A. Bienfait, H.-S. Chang, C.R. Conner, É. Dumur, J. Grebel, R.G. Povey, E. Şahin, K.J. Satzinger, Y.P. Zhong, and A.N. Cleland. Continuous and time-domain coherent signal conversion between optical and microwave frequencies. *Physical Review Applied*, 14(6), December 2020.

[18] Nicholas J. Lambert, Alfredo Rueda, Florian Sedlmeir, and Harald G. L. Schwefel. Coherent conversion between microwave and optical photons—an overview of physical implementations. *Advanced Quantum Technologies*, 3(1):1900077, January 2020.

[19] Wentao Jiang, Christopher J. Sarabalis, Yanni D. Dahmani, Rishi N. Patel, Felix M. Mayor, Timothy P. McKenna, Raphaël Van Laer, and Amir H. Safavi-Naeini. Efficient bidirectional piezo-optomechanical transduction between microwave and optical frequency. *Nature Communications*, 11(1), March 2020.

[20] Xu Han, Wei Fu, Changchun Zhong, Chang-Ling Zou, Yuntao Xu, Ayed Al Sayem, Mingrui Xu, Sihao Wang, Risheng Cheng, Liang Jiang, and Hong X. Tang. Cavity piezo-mechanics for superconducting-nanophotonic quantum interface. *Nature Communications*, 11(1), June 2020.

[21] R. D. Delaney, M. D. Urmey, S. Mittal, B. M. Brubaker, J. M. Kindem, P. S. Burns,

C. A. Regal, and K. W. Lehnert. Superconducting-qubit readout via low-backaction electro-optic transduction. *Nature*, 606(7914):489–493, June 2022.

[22] A. D. O'Connell, M. Hofheinz, M. Ansmann, Radoslaw C. Bialczak, M. Lenander, Erik Lucero, M. Neeley, D. Sank, H. Wang, M. Weides, J. Wenner, John M. Martinis, and A. N. Cleland. Quantum ground state and single-phonon control of a mechanical resonator. *Nature*, 464(7289):697–703, March 2010.

[23] Yiwen Chu, Prashanta Kharel, William H. Renninger, Luke D. Burkhart, Luigi Frunzio, Peter T. Rakich, and Robert J. Schoelkopf. Quantum acoustics with superconducting qubits. *Science*, 358(6360):199–202, October 2017.

[24] K. J. Satzinger, Y. P. Zhong, H.-S. Chang, G. A. Peairs, A. Bienfait, Ming-Han Chou, A. Y. Cleland, C. R. Conner, É. Dumur, J. Grebel, I. Gutierrez, B. H. November, R. G. Povey, S. J. Whiteley, D. D. Awschalom, D. I. Schuster, and A. N. Cleland. Quantum control of surface acoustic-wave phonons. *Nature*, 563(7733):661–665, November 2018.

[25] Yiwen Chu, Prashanta Kharel, Taekwan Yoon, Luigi Frunzio, Peter T. Rakich, and Robert J. Schoelkopf. Creation and control of multi-phonon fock states in a bulk acoustic-wave resonator. *Nature*, 563(7733):666–670, November 2018.

[26] A. Bienfait, K. J. Satzinger, Y. P. Zhong, H.-S. Chang, M.-H. Chou, C. R. Conner, É. Dumur, J. Grebel, G. A. Peairs, R. G. Povey, and A. N. Cleland. Phonon-mediated quantum state transfer and remote qubit entanglement. *Science*, 364(6438):368–371, April 2019.

[27] Patricio Arrangoiz-Arriola, E. Alex Wollack, Zhaoyou Wang, Marek Pechal, Wentao Jiang, Timothy P. McKenna, Jeremy D. Witmer, Raphaël Van Laer, and Amir H. Safavi-Naeini. Resolving the energy levels of a nanomechanical oscillator. *Nature*, 571(7766):537–540, July 2019.

[28] L. R. Sletten, B. A. Moores, J. J. Viennot, and K. W. Lehnert. Resolving phonon fock states in a multimode cavity with a double-slit qubit. *Physical Review X*, 9(2), June 2019.

[29] Mikael Kervinen, Alpo Välimaa, Jhon E. Ramírez-Muñoz, and Mika A. Sillanpää. Sideband control of a multimode quantum bulk acoustic system. *Physical Review Applied*, 14(5), November 2020.

[30] M.-H. Chou, É. Dumur, Y. P. Zhong, G. A. Peairs, A. Bienfait, H.-S. Chang, C. R. Conner, J. Grebel, R. G. Povey, K. J. Satzinger, and A. N. Cleland. Measurements of a quantum bulk acoustic resonator using a superconducting qubit. *Applied Physics Letters*, 117(25):254001, December 2020.

[31] Samuel J. Whiteley, Gary Wolfowicz, Christopher P. Anderson, Alexandre Bourassa, He Ma, Meng Ye, Gerwin Koolstra, Kevin J. Satzinger, Martin V. Holt, F. Joseph Heremans, Andrew N. Cleland, David I. Schuster, Giulia Galli, and David D. Awschalom. Spin–phonon interactions in silicon carbide addressed by Gaussian acoustics. *Nature Physics*, 15(5):490–495, February 2019.

[32] Huiyao Chen, Noah F. Opondo, Boyang Jiang, Evan R. MacQuarrie, Raphaël S. Daveau, Sunil A. Bhave, and Gregory D. Fuchs. Engineering electron–phonon coupling of quantum defects to a semiconfocal acoustic resonator. *Nano Letters*, 19(10):7021–7027, September 2019.

[33] J. R. Gell, M. B. Ward, R. J. Young, R. M. Stevenson, P. Atkinson, D. Anderson, G. A. C. Jones, D. A. Ritchie, and A. J. Shields. Modulation of single quantum dot energy levels by a surface-acoustic-wave. *Applied Physics Letters*, 93(8):081115, August 2008.

[34] M. Metcalfe, S. M. Carr, A. Muller, G. S. Solomon, and J. Lawall. Resolved sideband

emission of InAs/GaAs quantum dots strained by surface acoustic waves. *Physical Review Letters*, 105(3), July 2010.

[35] Martin V. Gustafsson, Thomas Aref, Anton Frisk Kockum, Maria K. Ekström, Göran Johansson, and Per Delsing. Propagating phonons coupled to an artificial atom. *Science*, 346(6206):207–211, October 2014.

[36] A Hernández-Mínguez, Y-T Liou, and P V Santos. Interaction of surface acoustic waves with electronic excitations in graphene. *Journal of Physics D: Applied Physics*, 51(38):383001, August 2018.

[37] J. D. Teufel, T. Donner, M. A. Castellanos-Beltran, J. W. Harlow, and K. W. Lehnert. Nanomechanical motion measured with an imprecision below that at the standard quantum limit. *Nature Nanotechnology*, 4(12):820–823, November 2009.

[38] Asimina Arvanitaki, Savas Dimopoulos, and Ken Van Tilburg. Sound of dark matter: Searching for light scalars with resonant-mass detectors. *Physical Review Letters*, 116(3), January 2016.

[39] Jack Manley, Dalziel J. Wilson, Russell Stump, Daniel Grin, and Swati Singh. Searching for scalar dark matter with compact mechanical resonators. *Physical Review Letters*, 124(15), April 2020.

[40] Daniel Carney, Anson Hook, Zhen Liu, Jacob M Taylor, and Yue Zhao. Ultralight dark matter detection with mechanical quantum sensors. *New Journal of Physics*, 23(2):023041, February 2021.

[41] Maxim Goryachev and Michael E. Tobar. Gravitational wave detection with high frequency phonon trapping acoustic cavities. *Physical Review D*, 90(10), November 2014.

[42] Maxim Goryachev, William M. Campbell, Ik Siong Heng, Serge Galliou, Eugene N. Ivanov, and Michael E. Tobar. Rare events detected with a bulk acoustic wave high frequency gravitational wave antenna. *Physical Review Letters*, 127(7), August 2021.

[43] Nancy Aggarwal, Odylio D. Aguiar, Andreas Bauswein, Giancarlo Cella, Sebastian Clesse, Adrian Michael Cruise, Valerie Domcke, Daniel G. Figueroa, Andrew Geraci, Maxim Goryachev, Hartmut Grote, Mark Hindmarsh, Francesco Muia, Nikhil Mukund, David Ottaway, Marco Peloso, Fernando Quevedo, Angelo Ricciardone, Jessica Steinlechner, Sebastian Steinlechner, Sichun Sun, Michael E. Tobar, Francisco Torrenti, Caner Ünal, and Graham White. Challenges and opportunities of gravitational-wave searches at MHz to GHz frequencies. *Living Reviews in Relativity*, 24(1), December 2021.

[44] Matt McEwen, Lara Faoro, Kunal Arya, Andrew Dunsworth, Trent Huang, Seon Kim, Brian Burkett, Austin Fowler, Frank Arute, Joseph C. Bardin, Andreas Bengtsson, Alexander Bilmes, Bob B. Buckley, Nicholas Bushnell, Zijun Chen, Roberto Collins, Sean Demura, Alan R. Derk, Catherine Erickson, Marissa Giustina, Sean D. Harrington, Sabrina Hong, Evan Jeffrey, Julian Kelly, Paul V. Klimov, Fedor Kostritsa, Pavel Laptev, Aditya Locharla, Xiao Mi, Kevin C. Miao, Shirin Montazeri, Josh Mutus, Ofer Naaman, Matthew Neeley, Charles Neill, Alex Opremcak, Chris Quintana, Nicholas Redd, Pedram Roushan, Daniel Sank, Kevin J. Satzinger, Vladimir Shvarts, Theodore White, Z. Jamie Yao, Ping Yeh, Juhwan Yoo, Yu Chen, Vadim Smelyanskiy, John M. Martinis, Hartmut Neven, Anthony Megrant, Lev Ioffe, and Rami Barends. Resolving catastrophic error bursts from cosmic rays in large arrays of superconducting qubits. *Nature Physics*, 18(1):107–111, December 2021.

[45] John M. Martinis. Saving superconducting quantum processors from decay and correlated errors generated by gamma and cosmic rays. *npj Quantum Information*, 7(1), June 2021.

[46] C. D. Wilen, S. Abdullah, N. A. Kurinsky, C. Stanford, L. Cardani, G. D'Imperio, C. Tomei, L. Faoro, L. B. Ioffe, C. H. Liu, A. Opremcak, B. G. Christensen, J. L. DuBois, and R. McDermott. Correlated charge noise and relaxation errors in superconducting qubits. *Nature*, 594(7863):369–373, June 2021.

[47] Daniel Gottesman, Alexei Kitaev, and John Preskill. Encoding a qubit in an oscillator. *Physical Review A*, 64(1), June 2001.

[48] Zaki Leghtas, Gerhard Kirchmair, Brian Vlastakis, Robert J. Schoelkopf, Michel H. Devoret, and Mazyar Mirrahimi. Hardware-efficient autonomous quantum memory protection. *Physical Review Letters*, 111(12), September 2013.

[49] Marios H. Michael, Matti Silveri, R. T. Brierley, Victor V. Albert, Juha Salmilehto, Liang Jiang, and S. M. Girvin. New class of quantum error-correcting codes for a bosonic mode. *Physical Review X*, 6(3), July 2016.

[50] Weizhou Cai, Yuwei Ma, Weiting Wang, Chang-Ling Zou, and Luyan Sun. Bosonic quantum error correction codes in superconducting quantum circuits. *Fundamental Research*, 1(1):50–67, January 2021.

[51] Kevin S. Chou, Jacob Z. Blumoff, Christopher S. Wang, Philip C. Reinhold, Christopher J. Axline, Yvonne Y. Gao, L. Frunzio, M. H. Devoret, Liang Jiang, and R. J. Schoelkopf. Deterministic teleportation of a quantum gate between two logical qubits. *Nature*, 561(7723):368–373, September 2018.

[52] Yvonne Y. Gao, Brian J. Lester, Kevin S. Chou, Luigi Frunzio, Michel H. Devoret, Liang Jiang, S. M. Girvin, and Robert J. Schoelkopf. Entanglement of bosonic modes through an engineered exchange interaction. *Nature*, 566(7745):509–512, February 2019.

[53] A. Grimm, N. E. Frattini, S. Puri, S. O. Mundhada, S. Touzard, M. Mirrahimi, S. M.

Girvin, S. Shankar, and M. H. Devoret. Stabilization and operation of a Kerr-cat qubit. *Nature*, 584(7820):205–209, August 2020.

[54] P. Campagne-Ibarcq, A. Eickbusch, S. Touzard, E. Zalys-Geller, N. E. Frattini, V. V. Sivak, P. Reinhold, S. Puri, S. Shankar, R. J. Schoelkopf, L. Frunzio, M. Mirrahimi, and M. H. Devoret. Quantum error correction of a qubit encoded in grid states of an oscillator. *Nature*, 584(7821):368–372, August 2020.

[55] Philip Reinhold, Serge Rosenblum, Wen-Long Ma, Luigi Frunzio, Liang Jiang, and Robert J. Schoelkopf. Error-corrected gates on an encoded qubit. *Nature Physics*, 16(8):822–826, June 2020.

[56] Christopher Chamberland, Kyungjoo Noh, Patricio Arrangoiz-Arriola, Earl T. Campbell, Connor T. Hann, Joseph Iverson, Harald Putterman, Thomas C. Bohdanowicz, Steven T. Flammia, Andrew Keller, Gil Refael, John Preskill, Liang Jiang, Amir H. Safavi-Naeini, Oskar Painter, and Fernando G.S.L. Brandão. Building a fault-tolerant quantum computer using concatenated cat codes. *PRX Quantum*, 3(1), February 2022.

[57] Y. Tsaturyan, A. Barg, E. S. Polzik, and A. Schliesser. Ultracoherent nanomechanical resonators via soft clamping and dissipation dilution. *Nature Nanotechnology*, 12(8):776–783, June 2017.

[58] Gregory S. MacCabe, Hengjiang Ren, Jie Luo, Justin D. Cohen, Hengyun Zhou, Alp Sipahigil, Mohammad Mirhosseini, and Oskar Painter. Nano-acoustic resonator with ultralong phonon lifetime. *Science*, 370(6518):840–843, November 2020.

[59] Riccardo Manenti, Anton F. Kockum, Andrew Patterson, Tanja Behrle, Joseph Rahamim, Giovanna Tancredi, Franco Nori, and Peter J. Leek. Circuit quantum acoustodynamics with surface acoustic waves. *Nature Communications*, 8(1), October 2017.

[60] É. Dumur, K. J. Satzinger, G. A. Peairs, M.-H. Chou, A. Bienfait, H.-S. Chang, C. R. Conner, J. Grebel, R. G. Povey, Y. P. Zhong, and A. N. Cleland. Quantum communic-

ation with itinerant surface acoustic wave phonons. *npj Quantum Information*, 7(1), December 2021.

[61] Gustav Andersson, Shan W. Jolin, Marco Scigliuzzo, Riccardo Borgani, Mats O. Tholén, J.C. Rivera Hernández, Vitaly Shumeiko, David B. Haviland, and Per Delsing. Squeezing and multimode entanglement of surface acoustic wave phonons. *PRX Quantum*, 3(1), January 2022.

[62] E. Alex Wollack, Agnetta Y. Cleland, Rachel G. Gruenke, Zhaoyou Wang, Patricio Arrangoiz-Arriola, and Amir H. Safavi-Naeini. Quantum state preparation and tomography of entangled mechanical resonators. *Nature*, 604(7906):463–467, April 2022.

[63] Marius Bild, Matteo Fadel, Yu Yang, Uwe von Lüpke, Phillip Martin, Alessandro Bruno, and Yiwen Chu. Schrödinger cat states of a 16-microgram mechanical oscillator.

[64] Matthew Reagor, Hanhee Paik, Gianluigi Catelani, Luyan Sun, Christopher Axline, Eric Holland, Ioan M. Pop, Nicholas A. Masluk, Teresa Brecht, Luigi Frunzio, Michel H. Devoret, Leonid Glazman, and Robert J. Schoelkopf. Reaching 10 ms single photon lifetimes for superconducting aluminum cavities. *Applied Physics Letters*, 102(19):192604, May 2013.

[65] Srivatsan Chakram, Andrew E. Oriani, Ravi K. Naik, Akash V. Dixit, Kevin He, Ankur Agrawal, Hyeokshin Kwon, and David I. Schuster. Seamless high-Q microwave cavities for multimode circuit quantum electrodynamics. *Physical Review Letters*, 127(10), August 2021.

[66] A. Romanenko, R. Pilipenko, S. Zorzetti, D. Frolov, M. Awida, S. Belomestnykh, S. Posen, and A. Grassellino. Three-dimensional superconducting resonators at $T < 20$ mK with photon lifetimes up to τ=2 s. *Physical Review Applied*, 13(3), March 2020.

[67] Jens Koch, Terri M. Yu, Jay Gambetta, A. A. Houck, D. I. Schuster, J. Majer, Alexan-

dre Blais, M. H. Devoret, S. M. Girvin, and R. J. Schoelkopf. Charge-insensitive qubit design derived from the Cooper pair box. *Physical Review A*, 76(4), October 2007.

[68] David Isaac Schuster. *Circuit quantum electrodynamics*. PhD thesis, Yale University, 2007.

[69] Daniel Thomas Sank. *Fast, accurate state measurement in superconducting qubits*. PhD thesis, University of California, Santa Barbara, 2014.

[70] Charles James Neill. *A Path Towards Quantum Supremacy with Superconducting Qubits*. PhD thesis, University of California, Santa Barbara, 2017.

[71] Zijun Chen. *Metrology of Quantum Control and Measurement in Superconducting Qubits*. PhD thesis, University of California, Santa Barbara, 2018.

[72] P. Krantz, M. Kjaergaard, F. Yan, T. P. Orlando, S. Gustavsson, and W. D. Oliver. A quantum engineer's guide to superconducting qubits. *Applied Physics Reviews*, 6(2):021318, June 2019.

[73] Youpeng Zhong. *Violating Bell's Inequality with Remotely-Connected Superconducting Qubits*. PhD thesis, 2019.

[74] Hung-Shen Chang. *Remote Entanglement via Adiabatic Passage Using a Tunably Dissipative Quantum Communication System*. PhD thesis, 2021.

[75] Supriyo Datta. *Surface acoustic wave devices*. Prentice-Hall, 1986.

[76] David Morgan. *Surface Acoustic Wave Filters*. Elsevier Science & Techn., 2010.

[77] Amir H. Safavi-Naeini and Oskar Painter. Optomechanical crystal devices. In *Cavity Optomechanics*, pages 195–231. Springer Berlin Heidelberg, 2014.

[78] Thomas Aref, Per Delsing, Maria K. Ekström, Anton Frisk Kockum, Martin V. Gustafsson, Göran Johansson, Peter J. Leek, Einar Magnusson, and Riccardo Manenti.

Quantum acoustics with surface acoustic waves. In *Quantum Science and Technology*, pages 217–244. Springer International Publishing, 2016.

[79] Amit S. Vainsencher. *Building an Optomechanical Interface for Superconducting Qubits*. PhD thesis, University of California, Santa Barbara, 2016.

[80] Kevin Joseph Satzinger. *Quantum control of surface acoustic wave phonons*. PhD thesis, University of California, Santa Barbara, 2018.

[81] Gregory Peairs. *Fast and efficient transducers for microwave-optical quantum communication*. PhD thesis, University of California, Santa Barbara, 2019.

[82] B.D. Josephson. Possible new effects in superconductive tunnelling. *Physics Letters*, 1(7):251–253, July 1962.

[83] Charles Kittel. *Introduction to Solid State Physics*. WILEY, 2004.

[84] R. Barends, J. Kelly, A. Megrant, D. Sank, E. Jeffrey, Y. Chen, Y. Yin, B. Chiaro, J. Mutus, C. Neill, P. O'Malley, P. Roushan, J. Wenner, T. C. White, A. N. Cleland, and John M. Martinis. Coherent josephson qubit suitable for scalable quantum integrated circuits. *Physical Review Letters*, 111(8), August 2013.

[85] D. I. Schuster, A. A. Houck, J. A. Schreier, A. Wallraff, J. M. Gambetta, A. Blais, L. Frunzio, J. Majer, B. Johnson, M. H. Devoret, S. M. Girvin, and R. J. Schoelkopf. Resolving photon number states in a superconducting circuit. *Nature*, 445(7127):515–518, February 2007.

[86] U. Vool, S. Shankar, S. O. Mundhada, N. Ofek, A. Narla, K. Sliwa, E. Zalys-Geller, Y. Liu, L. Frunzio, R. J. Schoelkopf, S. M. Girvin, and M. H. Devoret. Continuous quantum nondemolition measurement of the transverse component of a qubit. *Physical Review Letters*, 117(13), September 2016.

[87] Jean-Claude Besse, Simone Gasparinetti, Michele C. Collodo, Theo Walter, Philipp Kurpiers, Marek Pechal, Christopher Eichler, and Andreas Wallraff. Single-shot quantum nondemolition detection of individual itinerant microwave photons. *Physical Review X*, 8(2), April 2018.

[88] E.T. Jaynes and F.W. Cummings. Comparison of quantum and semiclassical radiation theories with application to the beam maser. *Proceedings of the IEEE*, 51(1):89–109, 1963.

[89] Alexandre Blais, Ren-Shou Huang, Andreas Wallraff, S. M. Girvin, and R. J. Schoelkopf. Cavity quantum electrodynamics for superconducting electrical circuits: An architecture for quantum computation. *Physical Review A*, 69(6), June 2004.

[90] A. A. Houck, J. A. Schreier, B. R. Johnson, J. M. Chow, Jens Koch, J. M. Gambetta, D. I. Schuster, L. Frunzio, M. H. Devoret, S. M. Girvin, and R. J. Schoelkopf. Controlling the spontaneous emission of a superconducting transmon qubit. *Physical Review Letters*, 101(8), August 2008.

[91] M. D. Reed, B. R. Johnson, A. A. Houck, L. DiCarlo, J. M. Chow, D. I. Schuster, L. Frunzio, and R. J. Schoelkopf. Fast reset and suppressing spontaneous emission of a superconducting qubit. *Applied Physics Letters*, 96(20):203110, May 2010.

[92] Evan Jeffrey, Daniel Sank, J. Y. Mutus, T. C. White, J. Kelly, R. Barends, Y. Chen, Z. Chen, B. Chiaro, A. Dunsworth, A. Megrant, P. J. J. O'Malley, C. Neill, P. Roushan, A. Vainsencher, J. Wenner, A. N. Cleland, and John M. Martinis. Fast accurate state measurement with superconducting qubits. *Physical Review Letters*, 112(19), May 2014.

[93] Eyob A. Sete, John M. Martinis, and Alexander N. Korotkov. Quantum theory of a bandpass purcell filter for qubit readout. *Physical Review A*, 92(1), July 2015.

[94] C. Neill, P. Roushan, K. Kechedzhi, S. Boixo, S. V. Isakov, V. Smelyanskiy, A. Megrant, B. Chiaro, A. Dunsworth, K. Arya, R. Barends, B. Burkett, Y. Chen, Z. Chen, A. Fowler, B. Foxen, M. Giustina, R. Graff, E. Jeffrey, T. Huang, J. Kelly, P. Klimov, E. Lucero, J. Mutus, M. Neeley, C. Quintana, D. Sank, A. Vainsencher, J. Wenner, T. C. White, H. Neven, and J. M. Martinis. A blueprint for demonstrating quantum supremacy with superconducting qubits. *Science*, 360(6385):195–199, April 2018.

[95] Frank Arute, Kunal Arya, Ryan Babbush, Dave Bacon, Joseph C. Bardin, Rami Barends, Rupak Biswas, Sergio Boixo, Fernando G. S. L. Brandao, David A. Buell, Brian Burkett, Yu Chen, Zijun Chen, Ben Chiaro, Roberto Collins, William Courtney, Andrew Dunsworth, Edward Farhi, Brooks Foxen, Austin Fowler, Craig Gidney, Marissa Giustina, Rob Graff, Keith Guerin, Steve Habegger, Matthew P. Harrigan, Michael J. Hartmann, Alan Ho, Markus Hoffmann, Trent Huang, Travis S. Humble, Sergei V. Isakov, Evan Jeffrey, Zhang Jiang, Dvir Kafri, Kostyantyn Kechedzhi, Julian Kelly, Paul V. Klimov, Sergey Knysh, Alexander Korotkov, Fedor Kostritsa, David Landhuis, Mike Lindmark, Erik Lucero, Dmitry Lyakh, Salvatore Mandrà, Jarrod R. McClean, Matthew McEwen, Anthony Megrant, Xiao Mi, Kristel Michielsen, Masoud Mohseni, Josh Mutus, Ofer Naaman, Matthew Neeley, Charles Neill, Murphy Yuezhen Niu, Eric Ostby, Andre Petukhov, John C. Platt, Chris Quintana, Eleanor G. Rieffel, Pedram Roushan, Nicholas C. Rubin, Daniel Sank, Kevin J. Satzinger, Vadim Smelyanskiy, Kevin J. Sung, Matthew D. Trevithick, Amit Vainsencher, Benjamin Villalonga, Theodore White, Z. Jamie Yao, Ping Yeh, Adam Zalcman, Hartmut Neven, and John M. Martinis. Quantum supremacy using a programmable superconducting processor. *Nature*, 574(7779):505–510, October 2019.

[96] Fabian Marxer, Antti Vepsäläinen, Shan W. Jolin, Jani Tuorila, Alessandro Landra, Caspar Ockeloen-Korppi, Wei Liu, Olli Ahonen, Adrian Auer, Lucien Belzane, Ville Bergholm, Chun Fai Chan, Kok Wai Chan, Tuukka Hiltunen, Juho Hotari, Eric

Hyyppä, Joni Ikonen, David Janzso, Miikka Koistinen, Janne Kotilahti, Tianyi Li, Jyrgen Luus, Miha Papic, Matti Partanen, Jukka Räbinä, Jari Rosti, Mykhailo Savytskyi, Marko Seppälä, Vasilii Sevriuk, Eelis Takala, Brian Tarasinski, Manish J. Thapa, Francesca Tosto, Natalia Vorobeva, Liuqi Yu, Kuan Yen Tan, Juha Hassel, Mikko Möttönen, and Johannes Heinsoo. Long-distance transmon coupler with CZ gate fidelity above 99.8%. *arXiv:2208.09460*.

[97] Yu Chen, C. Neill, P. Roushan, N. Leung, M. Fang, R. Barends, J. Kelly, B. Campbell, Z. Chen, B. Chiaro, A. Dunsworth, E. Jeffrey, A. Megrant, J. Y. Mutus, P. J. J. O'Malley, C. M. Quintana, D. Sank, A. Vainsencher, J. Wenner, T. C. White, Michael R. Geller, A. N. Cleland, and John M. Martinis. Qubit architecture with high coherence and fast tunable coupling. *Physical Review Letters*, 113(22), November 2014.

[98] X. Li, T. Cai, H. Yan, Z. Wang, X. Pan, Y. Ma, W. Cai, J. Han, Z. Hua, X. Han, Y. Wu, H. Zhang, H. Wang, Yipu Song, Luming Duan, and Luyan Sun. Tunable coupler for realizing a controlled-phase gate with dynamically decoupled regime in a superconducting circuit. *Physical Review Applied*, 14(2), August 2020.

[99] Youngkyu Sung, Leon Ding, Jochen Braumüller, Antti Vepsäläinen, Bharath Kannan, Morten Kjaergaard, Ami Greene, Gabriel O. Samach, Chris McNally, David Kim, Alexander Melville, Bethany M. Niedzielski, Mollie E. Schwartz, Jonilyn L. Yoder, Terry P. Orlando, Simon Gustavsson, and William D. Oliver. Realization of high-fidelity CZ and ZZ-free iSWAP gates with a tunable coupler. *Physical Review X*, 11(2), June 2021.

[100] Yuan Xu, Ji Chu, Jiahao Yuan, Jiawei Qiu, Yuxuan Zhou, Libo Zhang, Xinsheng Tan, Yang Yu, Song Liu, Jian Li, Fei Yan, and Dapeng Yu. High-fidelity, high-scalability two-qubit gate scheme for superconducting qubits. *Physical Review Letters*, 125(24), December 2020.

[101] Mark E Orwat. Experimental investigation of lamb waves in transversely isotropic composite plates. Master's thesis, Massachusetts Institute of Technology, 2001.

[102] Michael R. Geller, Emmanuel Donate, Yu Chen, Michael T. Fang, Nelson Leung, Charles Neill, Pedram Roushan, and John M. Martinis. Tunable coupler for superconducting Xmon qubits: Perturbative nonlinear model. *Physical Review A*, 92(1), July 2015.

[103] J.D. Larson, P.D. Bradley, S. Wartenberg, and R.C. Ruby. Modified butterworth-van dyke circuit for FBAR resonators and automated measurement system. In *2000 IEEE Ultrasonics Symposium. Proceedings. An International Symposium (Cat. No.00CH37121)*. IEEE, 2000.

[104] Ru-Yuan Yang, Yan-Kuin Su, Min-Hang Weng, Cheng-Yuan Hung, and Hung-Wei Wu. Characteristics of coplanar waveguide on lithium niobate crystals as a microwave substrate. *Journal of Applied Physics*, 101(1):014101, January 2007.

[105] Aaron D. O'Connell, M. Ansmann, R. C. Bialczak, M. Hofheinz, N. Katz, Erik Lucero, C. McKenney, M. Neeley, H. Wang, E. M. Weig, A. N. Cleland, and J. M. Martinis. Microwave dielectric loss at single photon energies and millikelvin temperatures. *Applied Physics Letters*, 92(11):112903, March 2008.

[106] Maxim Goryachev, Nikita Kostylev, and Michael E. Tobar. Single-photon level study of microwave properties of lithium niobate at millikelvin temperatures. *Physical Review B*, 92(6), August 2015.

[107] E. Alex Wollack, Agnetta Y. Cleland, Patricio Arrangoiz-Arriola, Timothy P. McKenna, Rachel G. Gruenke, Rishi N. Patel, Wentao Jiang, Christopher J. Sarabalis, and Amir H. Safavi-Naeini. Loss channels affecting lithium niobate phononic crystal resonators at cryogenic temperature. *Applied Physics Letters*, 118(12):123501, March 2021.

[108] Marco Scigliuzzo, Laure E Bruhat, Andreas Bengtsson, Jonathan J Burnett, Anita Fadavi Roudsari, and Per Delsing. Phononic loss in superconducting resonators on piezoelectric substrates. *New Journal of Physics*, 22(5):053027, May 2020.

[109] A. Megrant, C. Neill, R. Barends, B. Chiaro, Yu Chen, L. Feigl, J. Kelly, Erik Lucero, Matteo Mariantoni, P. J. J. O'Malley, D. Sank, A. Vainsencher, J. Wenner, T. C. White, Y. Yin, J. Zhao, C. J. Palmstrøm, John M. Martinis, and A. N. Cleland. Planar superconducting resonators with internal quality factors above one million. *Applied Physics Letters*, 100(11):113510, March 2012.

[110] David M. Pozar. *Microwave Engineering*. WILEY, 2011.

[111] V. V. Felmetsger, P. N. Laptev, and S. M. Tanner. Innovative technique for tailoring intrinsic stress in reactively sputtered piezoelectric aluminum nitride films. *Journal of Vacuum Science & Technology A: Vacuum, Surfaces, and Films*, 27(3):417–422, May 2009.

[112] Matthew Borselli, Thomas J. Johnson, and Oskar Painter. Measuring the role of surface chemistry in silicon microphotonics. *Applied Physics Letters*, 88(13):131114, March 2006.

[113] Julian Kelly. *Fault-tolerant superconducting qubits*. PhD thesis, University of California, Santa Barbara, 2015.

[114] G. J. Dolan. Offset masks for lift-off photoprocessing. *Applied Physics Letters*, 31(5):337–339, September 1977.

[115] A. Dunsworth, A. Megrant, C. Quintana, Zijun Chen, R. Barends, B. Burkett, B. Foxen, Yu Chen, B. Chiaro, A. Fowler, R. Graff, E. Jeffrey, J. Kelly, E. Lucero, J. Y. Mutus, M. Neeley, C. Neill, P. Roushan, D. Sank, A. Vainsencher, J. Wenner, T. C. White, and John M. Martinis. Characterization and reduction of capacitive

loss induced by sub-micron josephson junction fabrication in superconducting qubits. *Applied Physics Letters*, 111(2):022601, July 2017.

[116] K. J. Satzinger, C. R. Conner, A. Bienfait, H.-S. Chang, Ming-Han Chou, A. Y. Cleland, É. Dumur, J. Grebel, G. A. Peairs, R. G. Povey, S. J. Whiteley, Y. P. Zhong, D. D. Awschalom, D. I. Schuster, and A. N. Cleland. Simple non-galvanic flip-chip integration method for hybrid quantum systems. *Applied Physics Letters*, 114(17):173501, April 2019.

[117] D. Rosenberg, D. Kim, R. Das, D. Yost, S. Gustavsson, D. Hover, P. Krantz, A. Melville, L. Racz, G. O. Samach, S. J. Weber, F. Yan, J. L. Yoder, A. J. Kerman, and W. D. Oliver. 3D integrated superconducting qubits. *npj Quantum Information*, 3(1), October 2017.

[118] L. Glasser. Equations of state and phase diagrams. *Journal of Chemical Education*, 79(7):874, July 2002.

[119] David P. Pappas, Michael R. Vissers, David S. Wisbey, Jeffrey S. Kline, and Jiansong Gao. Two level system loss in superconducting microwave resonators. *IEEE Transactions on Applied Superconductivity*, 21(3):871–874, June 2011.

[120] Clemens Müller, Jared H Cole, and Jürgen Lisenfeld. Towards understanding two-level-systems in amorphous solids: insights from quantum circuits. *Reports on Progress in Physics*, 82(12):124501, October 2019.

[121] G. Andersson, A. L. O. Bilobran, M. Scigliuzzo, M. M. de Lima, J. H. Cole, and P. Delsing. Acoustic spectral hole-burning in a two-level system ensemble. *npj Quantum Information*, 7(1), January 2021.

[122] H. Wang, Matteo Mariantoni, Radoslaw C. Bialczak, M. Lenander, Erik Lucero, M. Neeley, A. D. O'Connell, D. Sank, M. Weides, J. Wenner, T. Yamamoto, Y. Yin,

J. Zhao, John M. Martinis, and A. N. Cleland. Deterministic entanglement of photons in two superconducting microwave resonators. *Physical Review Letters*, 106(6), February 2011.

[123] Qicheng Zhang, Daehun Lee, Lu Zheng, Xuejian Ma, Shawn I. Meyer, Li He, Han Ye, Ze Gong, Bo Zhen, Keji Lai, and A. T. Charlie Johnson. Gigahertz topological valley Hall effect in nanoelectromechanical phononic crystals. *Nature Electronics*, 5(3):157–163, March 2022.

[124] Alkim Bozkurt, Han Zhao, Chaitali Joshi, Henry G. LeDuc, Peter K. Day, and Mohammad Mirhosseini. A quantum electromechanical interface for long-lived phonons. *arXiv:2207.10972*.

[125] Vittorio Giovannetti, Seth Lloyd, and Lorenzo Maccone. Quantum random access memory. *Physical Review Letters*, 100(16), April 2008.

[126] Connor T. Hann, Chang-Ling Zou, Yaxing Zhang, Yiwen Chu, Robert J. Schoelkopf, S. M. Girvin, and Liang Jiang. Hardware-efficient quantum random access memory with hybrid quantum acoustic systems. *Physical Review Letters*, 123(25), December 2019.

[127] E. Knill, R. Laflamme, and G. J. Milburn. A scheme for efficient quantum computation with linear optics. *Nature*, 409(6816):46–52, January 2001.

[128] Pieter Kok, W. J. Munro, Kae Nemoto, T. C. Ralph, Jonathan P. Dowling, and G. J. Milburn. Linear optical quantum computing with photonic qubits. *Reviews of Modern Physics*, 79(1):135–174, January 2007.

[129] Aaron D O'Connell. *A Macroscopic Mechanical Resonator Operated in the Quantum Limit*. PhD thesis, University of California, Santa Barbara, 2010.